Title
Dissecting the role of cell physical properties in the invasion of pancreatic ductal adenocarcinoma

Permalink
https://escholarship.org/uc/item/2sz0s13b

Author
Nguyen, Angelyn Thuy An Vu

Publication Date
2017

Peer reviewed|Thesis/dissertation

UNIVERSITY OF CALIFORNIA

Los Angeles

Dissecting the role of cell physical properties in the invasion of pancreatic ductal adenocarcinoma

A dissertation submitted in partial satisfaction of the
requirements for the degree Doctor of Philosophy
in Molecular, Cellular, and Integrative Physiology

by

Angelyn Thuy An Vu Nguyen

2017

ABSTRACT OF THE DISSERTATION

Dissecting the role of cell physical properties in the invasion of pancreatic ductal adenocarcinoma

by

Angelyn Thuy An Vu Nguyen
Doctor of Philosophy in Molecular, Cellular, and Integrative Physiology
University of California, Los Angeles, 2017
Professor Amy Catherine Rowat, Chair

Metastasis is a physical process in which cells are required to deform through narrow gaps and generate forces as they invade surrounding tissues. Understanding the relationship between invasion and cell physical properties, such as deformability and contractility, can impart knowledge that guides the development of new therapeutics, yet the physical properties of pancreatic cancer cells are still poorly understood. In many cancers, more invasive cells are more deformable than less invasive cells. However, using atomic force microscopy, I discovered that more invasive pancreatic ductal adenocarcinoma (PDAC) cells tend to have a higher Young's modulus, indicating that they are stiffer. This finding challenges the oversimplified notion that decreased cell stiffness is a hallmark of cancer invasion. To gain a more complete understanding of why stiffer PDAC cells are more invasive, I examine the ability of PDAC cells to actively generate forces through actomyosin contractility and actin polymerization, as both processes have been associated with cancer cell invasion and stiffness. Using pharmacologic inhibitors, I determined that actomyosin contractility (inhibited with blebbistatin), as well as the polymerization of actin by Arp2/3 (inhibited with CK-666) and formin (inhibited with SMIFH2), contribute to the stiffness of PDAC cells. Interestingly, I observe that these inhibitors are cell line specific, indicating that different PDAC cell lines may rely on different modes of motility to invade the extracellular matrix. In addition, using measurements of cell physical phenotypes obtained by microfluidic quantitative deformability cytometry, my collaborators and I define a minimal set of physical phenotypes that can predict PDAC cell invasion. Taken together, my dissertation work provides valuable insight into the physical mechanisms of cancer cell invasion, and establishes a physical model that can predict cell invasion based on single-cell physical phenotypes including cell stiffness. My results provide the foundation for future studies into the relationship between cell physical properties and the tumor microenvironment, which undergoes substantial physical changes throughout PDAC progression.

The dissertation of Angelyn Thuy An Vu Nguyen is approved.

Timothy R. Donahue

Tomas Ganz

Stephen G. Young

Amy Catherine Rowat, Committee Chair

University of California, Los Angeles

2017

TABLE OF CONTENTS

Chapter I: Introduction

Chapter II: Stiffness of pancreatic cancer cells is associated with increased invasive potential

Chapter III: Myosin II, Arp2/3, and formin activity contribute to cancer cell stiffness and invasion

Chapter IV: Label-free prediction of cancer cell invasion by single-cell physical phenotyping

Chapter V: Conclusions and Future Directions

LIST OF FIGURES AND TABLES

Chapter II: Stiffness of pancreatic cancer cells is associated with increased invasive potential

Chapter III: Myosin II, Arp2/3, and formin activity contribute to cancer cell stiffness and invasion

Chapter IV: Label-free prediction of cancer cell invasion by single-cell physical phenotyping

Acknowledgements

I would like to express grateful acknowledgement to my mentor, Dr. Amy Rowat, for the opportunity to complete my Ph.D. in her laboratory and for all of her guidance throughout my studies. I would also like to thank my committee members, Dr. Timothy Donahue, Dr. Tomas Ganz, and Dr. Stephen Young, for their input and support.

I would like to acknowledge all of the members of the Rowat laboratory, past and present, for fond memories, insightful discussions, and productive collaborations, especially Kendra Nyberg and Dr. Tae-Hyung Kim. Additionally, I thank all of my co-authors that contributed to the manuscripts contained in this thesis. I am grateful for all of my funding sources, including the Farber Family Foundation, the Integrative Biology and Physiology Eureka Scholarship, and David Geffen Scholarship Foundation.

Finally, I would like to thank all of my family and friends for their enduring support throughout this journey.

Chapter 1 is a reproduction of: Nguyen AV, Nyberg KD, Scott MB, Welsh AM, Nguyen AH, Wu N, Hohlbauch SV, Geisse NA, Gibb EA, Robertson AG, Donahue TR, Rowat AC. Stiffness of pancreatic cancer cells is associated with increased invasive potential. Integr Biol. 2016;8(12):1232-1245. DOI: 10.1039/c6ib00135a. AVN and ACR designed experiments. KDN performed and analyzed the microfluidic deformability cytometry experiments. KDN also assisted with statistical analysis. MBS wrote a custom Matlab script to analyze adherent cell size data. AMW and AVN performed and analyzed immunoblotting experiments. AHN, NW, and

TRD assisted with cell culture and provided advice for the transwell migration experiments, as well as insight into the progression of PDAC. SVH and NAG planned and assisted with AFM experiments. EAG and GR performed RNAseq analysis. AVN performed all other experiments (scratch-wound invasion, transwell migration, scratch-wound migration, proliferation, AFM, imaging flow cytometry). All authors reviewed and contributed to the text.

Chapter 2 is a version of: Nguyen AV, Trompetto B, Tan M, Hsueh-heng K, Butte M, Chiou E, Rowat AC. Myosin II, Arp2/3, and formin activity contribute to cancer cell stiffness and invasion. In preparation for publication. AVN and ACR designed experiments. BT assisted with IncuCyte invasion experiments and pillar contractility experiments. KH and MB assisted with AFM set-up. MT and EC fabricated and assisted with analysis of pillar contractility experiments. AVN performed all experiments (scratch-wound invasion and proliferation assays, AFM, cell rounding assay, micropillar contractility assay, MMP activity assay). All authors reviewed and contributed to the text.

Chapter 3 is a version of: Nyberg KD, Bruce SL, Nguyen AV, Chan C, Gill NK, Kim T-H, Sloan EK, Rowat AC. Label-free prediction of cancer cell invasion by single-cell physical phenotyping. Nature Microsystems & Nanoengineering. Submitted. KDN and ACR designed experiments and prepared the manuscript. KDN, AVN, CKC, NKG, and THK performed experiments. KDN and SLB designed, implemented and evaluated machine learning algorithms. EKS provided guidance throughout the manuscript and study.

Vita

2008-2012, Physiological Sciences, B.S.

University of California, Los Angeles

Publications:

1. **Nguyen AV**, Trompetto B, Nyberg KD, et al. Myosin II, Arp2/3, and formin activity contribute to cancer cell stiffness and invasion. Manuscript in preparation.
2. Nyberg KD, Bruce S, **Nguyen AV**, et al. Label-free prediction of cancer cell invasion by single-cell physical phenotyping. Nature Microsystems & Nanoengineering. Submitted.
3. Kim TH, Gill NK, Nyberg KD, **Nguyen AV**, et al. Cancer cells become less deformable and more invasive with activation of β-adrenergic signaling. J Cell Sci. 2016;129(24):4563-4575.
4. **Nguyen AV**, Nyberg KD, Scott MB, et al. Stiffness of pancreatic cancer cells is associated with increased invasive potential. Integr Biol. 2016;8(12):1232-1245.
5. Jacobitz AW, Wereszczynski J, Yi SW, Amer BR, Huang GL, **Nguyen AV**, et al. Structural and computational studies of the Staphylococcus aureus sortase B-substrate complex reveal a substrate-stabilized oxyanion hole. J Biol Chem. 2014;289(13):8891-902.
6. Kang TM, Yuan J, **Nguyen A**, Becket E, Yang H, Miller JH. The aminoglycoside antibiotic kanamycin damages DNA bases in Escherichia coli: caffeine potentiates the DNA-damaging effects of kanamycin while suppressing cell killing by ciprofloxacin in Escherichia coli and Bacillus anthracis. Antimicrob Agents Chemother. 2012;56(6):3216-23.

Chapter I: Introduction

Pancreatic ductal adenocarcinoma (PDAC) is the cancer of the exocrine ductal cells of the pancreas, and represents 90% of all pancreatic cancers. This devastating disease has a five-year survival rate of 8% (1) and is the fourth leading cause of cancer-related deaths in the United States (2). The National Cancer Institute estimates that 53,670 new cases of pancreatic cancer will be diagnosed in 2017 (1). With the strong research efforts of the last few decades, significant advances have been made in understanding the mechanisms involved in the progression of PDAC, and the development of new therapeutics (3). Yet, despite these advances, even with the most recent and sophisticated surgical treatments and chemotherapy regimens, patients diagnosed with advanced disease have a median survival rate of only 1 year (4). The current statistics on pancreatic cancer, along with the lack of effective treatments, clearly communicate the strong need for additional research on this disease.

PDAC is a stroma-rich cancer. It is not uncommon for stromal components to outnumber tumor cells. This dense tumor microenvironment consists of extracellular matrix (ECM) components, as well as noncancerous cells including fibroblasts and immune cells. The development of extensive ECM and fibrosis, termed desmoplasia, is a result of the deposition of collagen, fibronectin, proteoglycans and hyaluronic acid, as well as proteinases (5). Increased fibrosis contributes to tumor rigidity, or stiffness (6). A recent study shows that patients with impaired epithelial transforming growth factor-β (TGF-β) signaling have high epithelial STAT3 activity and increased fibrosis, which is associated with shorter patient survival (7). Further, this study shows that PDAC tumor cells can sense the stiff ECM, and through mechanosignaling, or signaling induced by external mechanical stimuli, activate a positive feedback loop that increases fibrosis and tissue tension. Thus, there is evidence that the stiffness of the microenvironment contributes to disease progression. Yet, while tumor cells sense and changes their physical properties in response to their physical surroundings, it is unclear how the physical phenotypes of PDAC cells play a role in PDAC progression.

Ninety percent of cancer deaths are related to metastasis, a process in which cells of the primary tumor invade the extracellular matrix, transverse through blood vessels, and establish secondary tumor sites. Invasion and metastasis are inherently physical processes since cells must deform through pores of the extracellular matrix and capillaries, which are typically smaller than the diameter of a cell. The ability of cancer cells to invade and metastasize also requires them to generate physical forces to push and pull on the surrounding microenvironment. The majority of biophysical studies in breast, ovarian, and prostate cancers find that more deformable cells tend to be more invasive (8-14). This is thought to be beneficial to cancer cells since a cell must deform through small spaces to invade and metastasize. However, some studies using lung cancer cells and breast cancer cells treated with a beta-adrenergic receptor agonist find that stiffer cells are more invasive (15,16). The apparent discrepancies in the relationship between cell stiffness and invasion may stem from differences in intrinsic tissue properties: different tissues have inherently different physical properties, which could result in differential alterations in stiffness during cancer progression. For example, bone and cartilage is an order of magnitude stiffer than brain tissue (17). Therefore, bone cells may need to become more deformable to be more invasive, while brain tissue may need to become stiffer. Given the varied observations in the deformability of invading cancer cells in different cancer types and the importance of cell physical properties in hallmark cancer phenotypes, such as invasion, it is imperative to understand the physical properties of individual cancer types, including PDAC.

Cell deformability is influenced by a number of intrinsic and extrinsic factors. Extrinsic factors include soluble factors and the physical properties of the surrounding microenvironment (9, 15, 18). Two major intrinsic factors that contribute to the stiffness of a cell are structural proteins and its ability to actively generate forces.

Structural proteins. The mechanical phenotype, or mechanotype, of a cell dictates its ability to deform through narrow pores. Major determinants of mechanotype are the structural proteins within the cell, including vimentin, actin, and lamin A/C (19). Vimentin is a type III intermediate filament that plays a role in supporting and anchoring organelles in the cell cytoplasm, as well as resisting physical stresses. Vimentin is overexpressed in many cancers and considered a biomarker of epithelial-to-mesenchymal transition (20). Actin is a major component of the cell cytoskeleton. The monomeric form of this protein polymerizes to form actin filaments that are important in cell structure and the generation of contractile forces. Actin has also been implicated in cancer, since actomyosin contractions and the formation of protrusive forces are required for cell motility (21, described in more detail below). Lamin A, and its isoform lamin C, are type V intermediate filaments located in the nuclear lamina, which is found near the inner nuclear membrane (22). Alterations in lamin A expression have been implicated in cancer (23).

Active force generation. While structural proteins of the cytoskeleton and nucleus are major contributors to cell stiffness, mechanotype is also regulated by active force generation. The generation of contractile and protrusive forces are two main contributors to the forces that cells produce. Contractile forces, which contribute to actomyosin contractility, are a result of the interaction between myosin II with actin filaments, or F-actin, and the conversion of ATP into a mechanical energy. This process takes place in almost every cell in the human body, and is implicated in the motility of cells, including cancer cells (24). The generation of protrusions, such as invadopodia and lamellipodia, are driven by actin polymerization and contribute to some forms of cell migration. The two main pathways involved in the generation of protrusive forces are the WASP-Arp2/3 and formin pathways (25). Arp2/3 is responsible for actin nucleation and branching, which are essential for lamellipodia and invadopodia formation (26). The overexpression of Arp2/3, which leads to more actin polymerization and protrusion formation, is associated with breast, colorectal and lung cancers, as well as head and neck squamous cell carcinoma (27). Formins are involved in a secondary pathway for actin nucleation and protrusion formation. The inhibition of formins leads to a reduction in polarized cell growth, stress fiber formation, and invadopodia formation (28, 29). Further, formins have been implicated in epithelial-to-mesenchymal transition (29), and the overexpression of formins has been established in breast cancer and oral squamous cell carcinoma (30, 31). Since proteins that regulate cell mechanical properties and active force generation also mediate cell motility and invasion, determining the molecular alterations that influence the changes in cancer cell deformability can provide targets for novel therapeutics or co-treatments that improve the efficacy of existing drugs.

Collectively, gaining a deeper understanding of the physical phenotypes of PDAC cells will establish the foundation for future studies that link our understanding of cell physical properties and those of the surrounding microenvironment. This more complete knowledge of PDAC biophysics may lead to improvements in the sensitivity and efficacy of current drugs, as well as the development of novel therapeutics, in order to improve disease burden and decrease mortality rates.

References

1. Surveillance, Epidemiology, and End Results (SEER) 18 registries, National Cancer Institute, 2016.
2. Jemal A, Ward EM, Johnson CJ, et al. Annual Report to the Nation on the Status of Cancer, 1975-2014, Featuring Survival. J Natl Cancer Inst. 2017;109(9)
3. Valsecchi ME, Díaz-cantón E, De la vega M, Littman SJ. Recent treatment advances and novel therapies in pancreas cancer: a review. J Gastrointest Cancer. 2014;45(2):190-201.
4. Conroy T, Desseigne F, Ychou M, Bouche O, Guimbaud R, Becouarn Y, et al. FOLFIRINOX versus gemcitabine for metastatic pancreatic cancer. N Engl J Med. 2011;364(19):1817-25.
5. Feig C, Gopinathan A, Neesse A, Chan DS, Cook N, Tuveson DA. The pancreas cancer microenvironment. Clin Cancer Res. 2012;18(16):4266-76.
6. Paszek MJ, Zahir N, Johnson KR, et al. Tensional homeostasis and the malignant phenotype. Cancer Cell. 2005;8(3):241-54.
7. Laklai, H. et al. Genotype tunes pancreatic ductal adenocarcinoma tissue tension to induce matricellular fibrosis and tumor progression. Nat. Med. 22, 497–505 (2016).
8. Rother J, Nöding H, Mey I, Janshoff A. Atomic force microscopy-based microrheology reveals significant differences in the viscoelastic response between malign and benign cell lines. Open Biol. 2014;4(5):140046.
9. Laklai, H. et al. Genotype tunes pancreatic ductal adenocarcinoma tissue tension to induce matricellular fibrosis and tumor progression. Nat. Med. 22, 497–505 (2016).
10. Cross SE, Jin YS, Rao J, Gimzewski JK. Nanomechanical analysis of cells from cancer patients. Nat Nanotechnol. 2007;2(12):780-3.

11. Faria EC, Ma N, Gazi E, et al. Measurement of elastic properties of prostate cancer cells using AFM. Analyst. 2008;133(11):1498-500.
12. Plodinec M, Loparic M, Monnier CA, et al. The nanomechanical signature of breast cancer. Nat Nanotechnol. 2012;7(11):757-65.
13. Lopez JI, Kang I, You WK, Mcdonald DM, Weaver VM. In situ force mapping of mammary gland transformation. Integr Biol. 2011;3(9):910-21.
14. Xu W, Mezencev R, Kim B, Wang L, Mcdonald J, Sulchek T. Cell stiffness is a biomarker of the metastatic potential of ovarian cancer cells. PLoS ONE. 2012;7(10):e46609.
15. Kim TH, Gill NK, Nyberg KD, et al. Cancer cells become less deformable and more invasive with activation of β-adrenergic signaling. J Cell Sci. 2016;129(24):4563-4575.
16. Rosenbluth MJ, Lam WA, Fletcher DA. Force microscopy of nonadherent cells: a comparison of leukemia cell deformability. Biophys J. 2006;90(8):2994-3003.
17. Swift J, Ivanovska IL, Buxboim A, et al. Nuclear lamin-A scales with tissue stiffness and enhances matrix-directed differentiation. Science. 2013;341(6149):1240104.
18. Chen C, Xie J, Deng L, Yang L. Substrate stiffness together with soluble factors affects chondrocyte mechanoresponses. ACS Appl Mater Interfaces. 2014;6(18):16106-16.
19. Chan CK, Pan Y, Nyberg K, et al. Tumour-suppressor microRNAs regulate ovarian cancer cell physical properties and invasive behaviour. Open Biol. 2016;6(11)
20. Satelli A, Li S. Vimentin in cancer and its potential as a molecular target for cancer therapy. Cell Mol Life Sci. 2011;68(18):3033-46.
21. Olson MF, Sahai E. The actin cytoskeleton in cancer cell motility. Clin Exp Metastasis. 2009;26(4):273-87.

22. Gruenbaum Y, Wilson KL, Harel A, Goldberg M, Cohen M. Review: nuclear lamins--structural proteins with fundamental functions. J Struct Biol. 2000;129(2-3):313-23.
23. Sakthivel KM, Sehgal P. A Novel Role of Lamins from Genetic Disease to Cancer Biomarkers. Oncol Rev. 2016;10(2):309.
24. Murrell M, Oakes PW, Lenz M, Gardel ML. Forcing cells into shape: the mechanics of actomyosin contractility. Nat Rev Mol Cell Biol. 2015;16(8):486-98.
25. Yamaguchi H, Condeelis J. Regulation of the actin cytoskeleton in cancer cell migration and invasion. Biochim Biophys Acta. 2007;1773(5):642-52.
26. Goley ED, Welch MD. The ARP2/3 complex: an actin nucleator comes of age. Nat Rev Mol Cell Biol. 2006;7(10):713-26.
27. Ilatovskaya DV, Chubinskiy-nadezhdin V, Pavlov TS, et al. Arp2/3 complex inhibitors adversely affect actin cytoskeleton remodeling in the cultured murine kidney collecting duct M-1 cells. Cell Tissue Res. 2013;354(3):783-92.
28. Tojkander S, Gateva G, Schevzov G, et al. A molecular pathway for myosin II recruitment to stress fibers. Curr Biol. 2011;21(7):539-50.
29. Gardberg M, Kaipio K, Lehtinen L, et al. FHOD1, a formin upregulated in epithelial-mesenchymal transition, participates in cancer cell migration and invasion. PLoS ONE. 2013;8(9):e74923.
30. Lizárraga F, Poincloux R, Romao M, et al. Diaphanous-related formins are required for invadopodia formation and invasion of breast tumor cells. Cancer Res. 2009;69(7):2792-800.
31. Gardberg M, Kaipio K, Lehtinen L, et al. FHOD1, a formin upregulated in epithelial-mesenchymal transition, participates in cancer cell migration and invasion. PLoS ONE. 2013;8(9):e74923.

Chapter II: Stiffness of pancreatic cancer cells is associated with increased invasive potential

Integrative Biology

PAPER

View Article Online
View Journal

Cite this: DOI: 10.1039/c6ib00135a

Stiffness of pancreatic cancer cells is associated with increased invasive potential†

Angelyn V. Nguyen,[a] Kendra D. Nyberg,[ab] Michael B. Scott,[a] Alia M. Welsh,[c] Andrew H. Nguyen,[d] Nanping Wu,[d] Sophia V. Hohlbauch,[e] Nicholas A. Geisse,[e] Ewan A. Gibb,[f] A. Gordon Robertson,[f] Timothy R. Donahue[dg] and Amy C. Rowat*[abg]

Received 16th July 2016,
Accepted 7th October 2016

DOI: 10.1039/c6ib00135a

www.rsc.org/ibiology

Metastasis is a fundamentally physical process in which cells are required to deform through narrow gaps as they invade surrounding tissues and transit to distant sites. In many cancers, more invasive cells are more deformable than less invasive cells, but the extent to which mechanical phenotype, or mechanotype, can predict disease aggressiveness in pancreatic ductal adenocarcinoma (PDAC) remains unclear. Here we investigate the invasive potential and mechanical properties of immortalized PDAC cell lines derived from primary tumors and a secondary metastatic site, as well as noncancerous pancreatic ductal cells. To investigate how invasive behavior is associated with cell mechanotype, we flow cells through micron-scale pores using parallel microfiltration and microfluidic deformability cytometry; these results show that the ability of PDAC cells to passively transit through pores is only weakly correlated with their invasive potential. We also measure the Young's modulus of pancreatic ductal cells using atomic force microscopy, which reveals that there is a strong association between cell stiffness and invasive potential in PDAC cells. To determine the molecular origins of the variability in mechanotype across our PDAC cell lines, we analyze RNAseq data for genes that are known to regulate cell mechanotype. Our results show that vimentin, actin, and lamin A are among the most differentially expressed mechanoregulating genes across our panel of PDAC cell lines, as well as a cohort of 38 additional PDAC cell lines. We confirm levels of these proteins across our cell panel using immunoblotting, and find that levels of lamin A increase with both invasive potential and Young's modulus. Taken together, we find that stiffer PDAC cells are more invasive than more compliant cells, which challenges the paradigm that decreased cell stiffness is a hallmark of metastatic potential.

Insight, innovation, integration

Pancreatic ductal adenocarcinoma (PDAC) cells sense and respond to the increased stiffness of their microenvironment and deform through narrow gaps during metastasis. While physical processes are implicated in the progression of PDAC, the mechanical phenotype, or mechanotype, of tumor cells is poorly understood. Here we show that stiffer PDAC cells have a greater invasive potential than more deformable cells. We also investigate mechanoregulating proteins that contribute to the variability in mechanotype that we observe across different PDAC cell lines. Taken together, our findings provide insight into the mechanome of PDAC cells and suggest that the current paradigm of cell deformability as a hallmark of metastatic potential depends on cancer type.

Introduction

Pancreatic ductal adenocarcinoma (PDAC) remains one of the most aggressive and lethal cancers.[1,2] A major factor in the progression of this disease is the interaction between tumor cells and their microenvironment.[3,4] For example, mechanical cues activate signalling pathways, such as the JAK-STAT3 and integrin-FAK-ROCK axes, which promote cancer by triggering a positive feedback loop that results in increased ECM deposition,[4] fibrosis, and stiffness of the extracellular matrix (ECM).[5] In turn, cells respond to the stiffness of their substrate

---

[a] *Department of Integrative Biology and Physiology, University of California, Los Angeles, USA. E-mail: rowat@ucla.edu*
[b] *Department of Bioengineering, University of California, Los Angeles, USA*
[c] *Department of Microbiology, Immunology, and Molecular Genetics, University of California, Los Angeles, USA*
[d] *Department of General Surgery, University of California, Los Angeles, USA*
[e] *Asylum Research, an Oxford Instruments Company, Santa Barbara, California, USA*
[f] *Canada's Michael Smith Genome Sciences Centre, British Columbia Cancer Agency, Vancouver, BC, Canada*
[g] *Jonsson Comprehensive Cancer Center, University of California, Los Angeles, USA*

† Electronic supplementary information (ESI) available. See DOI: 10.1039/c6ib00135a

by altering their mechanical phenotype,[6,7] or mechanotype. A deeper knowledge of PDAC cell mechanotype and its underlying molecular components would provide a more complete understanding of how cells sense and transduce mechanical cues, and may ultimately identify molecules in mechanosignaling pathways that could be targeted to impede disease progression.

Cell mechanotype is linked to invasive potential in several types of cancers, including breast and ovarian.[8–10] The current paradigm is that more invasive or metastatic cancer cells are more deformable than their benign or less invasive counterparts.[8–17] A more deformable cell may have a selective advantage for metastasis, which requires individual tumor cells to transit through narrow vessels of the vasculature and extravasate to secondary tumor sites. However, there is also evidence that stiffer cancer cells are more invasive. For example, stiffer lung cancer cells and transformed fibroblasts are more motile in *in vitro* invasion assays.[18,19] While metastasis is the leading cause of death in PDAC and invasion is linked to cell mechanical properties in other cancers, the mechanotype of PDAC cells is not well understood.

Since metastasis requires cells to invade through the extracellular matrix and deform during transit through the vasculature, studies aiming to understand the possible roles of cell deformability in PDAC can benefit from complementary methods that measure cells in attached and suspended states. The use of multiple methods can also provide insight into the molecular mechanisms that determine cell mechanotype: different methods enable deformations over varying length scales, which determine the subcellular structures that contribute to the deformation response. For example, fluidic methods, such as micropipette aspiration and microfluidic deformability cytometry, measure cells in a suspended state, where cortical actin[20] and the nucleus[21,22] contribute to the deformation of cells through micron-scale pores. By contrast, in methods that induce local, 10 nm to 1 μm deformations on cells adhered to their substrate, such as atomic force microscopy (AFM)[23] and magnetic twisting cytometry,[24] actin can organize into stress fibers,[25] which have a marked effect on cell stiffness. Adhered cells also generate traction stresses, which result in increased cell stiffness[26] and enhanced invasive behavior of cancer cells.[27] For all of these reasons, comparisons of the same types of PDAC cells using multiple, complementary methods should provide more detailed insights into cancer cell mechanotype.

Here we investigate the invasive behavior and mechanotype of four immortalized pancreatic ductal cell lines, including cell lines derived from primary PDAC malignancies (MIA PaCa-2 and PANC-1) and a metastatic pleural effusion (Hs766T), as well as a nontransformed control cell line (HPDE). While the PDAC cell lines in our panel are derived from different sites, they all have similar founder mutations,[28] including alterations in *KRAS*, *TP53*, and *P16*. To determine the invasive potential of these cells, we perform a modified scratch wound invasion assay with Matrigel overlay to simulate the ECM. We also use a transwell migration assay without Matrigel to probe how effectively cells can migrate through narrow gaps independently of proteolytic matrix degradation. To assess how the deformability of PDAC cells is associated with their invasive potential, we use complementary mechanotyping methods to measure cells in both suspended and adhered states. We use parallel microfiltration (PMF)[15] and single-cell microfluidic deformability cytometry[29] to measure the deformability of suspended cells, and atomic force microscopy (AFM) to determine the Young's modulus of adhered cells. By analyzing gene expression data across our 3 PDAC cell lines, as well as data from 38 additional PDAC cell lines, we identify lamin A as a possible mechanoregulating protein that may contribute to the variability we observe in pancreatic ductal cell mechanotype. Taken together, our results show that stiffer PDAC cells are more invasive than more compliant PDAC cells, demonstrating that the relationship between cell invasive potential and mechanotype may vary for different types of cancers.

Results

Invasive behavior varies across pancreatic ductal adenocarcinoma cell lines

As cell mechanotype is associated with the invasive potential of cancer cells,[8–10] we first determine the invasion efficiency of PDAC cells derived from both primary and secondary sites, as well as that of noncancerous pancreatic ductal cells. To quantify cell invasion, we measure wound confluence using a modified scratch wound invasion assay where cells are overlaid with a ~1.5 mm-thick layer of Matrigel, a protein mixture that recapitulates the ECM (Fig. 1B); this setup requires cells to invade through a 3D matrix.[30,31] Our results show that there is variability in how quickly pancreatic ductal cells move into the wound gap. At 72 hours, the wound confluence across PDAC cells lines varies from 33 to 60% (Fig. 1A and B), indicating that cells with similar founder mutations[28] (Table S1, ESI†) have different invasion efficiencies. The MIA PaCa-2 and PANC-1 cells, which are derived from primary tumors, show increased invasion compared to the noncancerous HPDE cells (MIA PaCa-2: 33 ± 1%, PANC-1: 40 ± 2%, HPDE: 22 ± 4%; $p_{\text{MIA–HPDE}} = 8.5 \times 10^{-2}$, $p_{\text{PANC–HPDE}} = 3.5 \times 10^{-3}$). PANC-1 cells also show a significantly greater wound confluence than MIA PaCa-2 cells ($p_{\text{MIA–PANC}} = 4.0 \times 10^{-2}$). The Hs766T cells, which are derived from metastatic pleural effusion, exhibit the greatest invasive potential with a wound confluence of 60 ± 5%, which is ~2-fold higher than both the PANC-1 ($p_{\text{Hs766T–PANC}} = 5.8 \times 10^{-3}$) and MIA PaCa-2 cells ($p_{\text{Hs766T–MIA}} = 9.9 \times 10^{-4}$).

Since the speed at which cells migrate on a 2D surface could influence the observed differences in invasive potential, we repeat the scratch wound migration assays without a 3D Matrigel matrix (Fig. S1, ESI†). These results show that the cancerous cell lines have a significantly lower wound confluence than the HPDE cells after 24 hours (HPDE: 86 ± 6%, PDAC cell lines: 29 ± 4% to 34 ± 6%; $p_{\text{HPDE–PDAC}} < 3.6 \times 10^{-3}$), but there are no significant differences in migration efficiency between PDAC cell lines ($p > 0.05$ for all pairwise comparisons). Overall, we observe no significant correlation between migration and invasion potential ($R = -0.15$), indicating that our modified scratch wound invasion assay does not simply reflect differences in cell motility.

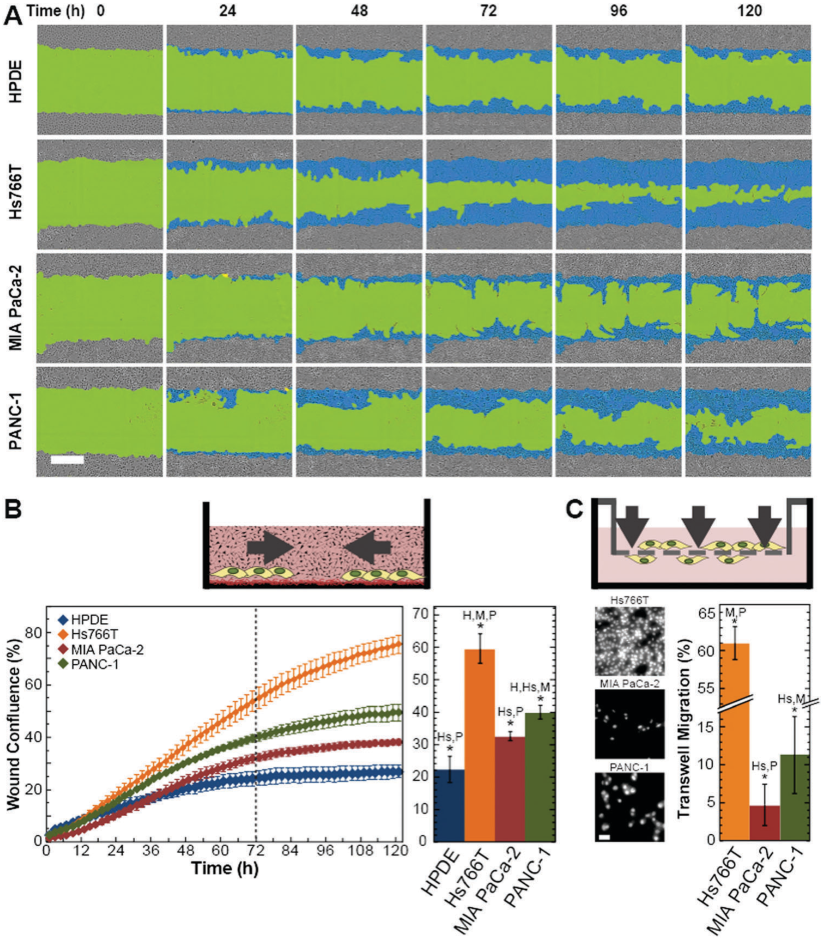

Fig. 1 Invasive behavior of pancreatic ductal adenocarcinoma cell lines. (A) Time series of images showing scratch wound invasion of pancreatic ductal cells through Matrigel. Wound confluence is the percentage of wound area covered by cells. Color legend: green is the wound area, blue shows wound confluence in the wound area, and grey represents the confluent cells outside of the wound area. Scale, 300 μm. (B) Schematic illustration showing the modified scratch wound assay. Cells are plated on a layer of thin Matrigel and invade into the thick 3D matrix of overlaid Matrigel that fills the scratch wound. The line plot shows quantification of wound confluence over time. The dotted line indicates the 72 h time point, which we use to compare wound confluence values for statistical significance. The bar plot represents wound confluence at the 72 h time point. Pairwise p-values are determined by a Student's t-test. $*p < 0.05$. (C) Schematic illustration showing the transwell migration assay. Cells migrate through the 8 μm pores of a polycarbonate membrane in response to a chemoattractant on the opposite side of the membrane. Images of transwell migration assays showing DRAQ5-labeled nuclei of cells that migrate through the 8 μm pores of a polycarbonate membrane after 12 hours. Scale, 50 μm. Pairwise p-values are determined by a Student's t-test. $*p < 0.05$. All error bars represent standard errors. The significance of pairwise comparisons between cell lines is shown in panels B and C by the initial(s) of the cell lines that are significantly different where H: HPDE, Hs: Hs766T, M: MIA PaCa-2, and P: PANC-1. For example, in panel B, HPDE is significantly different ($*p < 0.05$) from Hs766T (Hs) and PANC-1 (P).

Cell proliferation can also impact wound confluence. To exclude cell proliferation as a factor in our invasion results, we track the density of pancreatic ductal cell lines over 120 hours by time-lapse imaging (Fig. S2A–C, ESI†). We find that the Hs766T cells, which are the most invasive, have the lowest confluence of the four pancreatic ductal cell lines at 72 hours (47 ± 2%), indicating that these cells have the slowest proliferation rate. Conversely, the MIA PaCa-2 cells, which are the slowest PDAC cells to invade, show the highest confluence, which indicates that they proliferate most quickly. Across our 3 pancreatic cell lines, proliferation does not correlate with cell invasive potential ($R = -0.097$). We also track the proliferation of cells overlaid with Matrigel, as in our invasion assay (Fig. S2D and E, ESI†). We find that there is only a ~4–6% difference in proliferation across PDAC cell lines after 72 h. By contrast, we observe up to a 27% difference in invasion at the same time point (Fig. 1A and B). Furthermore, while apoptosis could influence differences in measurements of cell invasion, we observe no significant differences in apoptosis across PDAC cell lines with Matrigel overlay (Fig. S3, ESI†). Taken together, these results indicate that differences in cell doubling rates across our cell lines cannot explain the differences in invasion efficiencies that we observe.

PDAC cell migration through membrane pores is consistent with invasion through Matrigel

Invasion depends on the ability of cells to deform through narrow gaps, as well as their ability to degrade the surrounding protein matrix with secreted matrix metalloproteases (MMPs).[32–34] Degradation of the ECM results in an increased pore size, which can enhance invasion.[35] Thus, the variable expression and activity of secreted MMPs across PDAC cell lines[36–38] could influence our measurements of cell invasion through a protein matrix. To assess the contribution of cell deformability to invasion independently of MMP activity, we use a transwell migration assay, in which cells must actively deform through pores of a polycarbonate membrane. After 12 hours, MIA PaCa-2 cells have a lower percent migration than PANC-1 cells (MIA PaCa-2: 5 ± 3%, PANC-1: 11 ± 5%; $p = 1.1 \times 10^{-16}$), while the Hs766T cells show a statistically higher transwell migration efficiency compared to the two other PDAC cells (Hs766T: 62 ± 5%; $p_{\text{Hs766T–MIA}} = 2.0 \times 10^{-6}$, $p_{\text{Hs766T–PANC-1}} = 2.4 \times 10^{-6}$) (Fig. 1C). These transwell migration data are consistent with the data from our modified scratch wound invasion assay with Matrigel ($R = 0.99$; Fig. 5 and Table S2, ESI†), indicating that the variations in PDAC invasive potential are consistent with the ability of cells to migrate through narrow gaps.

PDAC cells vary in their ability to passively deform through micron-scale pores

During metastasis, cells must deform through micron-scale gaps in the ECM and basement membrane. Since more invasive cancer cells are generally more deformable than less invasive cells,[8–10] we next ask whether the differences in invasive potential between cell lines can be attributed to differences in the ability of cells to passively deform through pores. Here we refer to 'deformability' as the ability of cells to flow through pores when driven by an applied pressure.

To measure the deformability of pancreatic ductal cells, we use parallel microfiltration (PMF).[15] In PMF, we flow a suspension of cells across a porous membrane by applying air pressure for a defined time and then quantify the retention, or the volume of fluid that is retained above the membrane. Higher retention indicates that a larger fraction of cells has occluded the pores. In contrast, lower retention indicates that cells can passage more easily through the pores and thereby enable more fluid to flow across the membrane. Prior to PMF, cell suspensions are filtered through a 35 μm mesh filter to reduce aggregates; we confirm that our samples contain over 98% single cells using image analysis (Fig. S4, ESI†). MIA PaCa-2 cells exhibit a lower retention of 40 ± 10% compared to the HPDE noncancerous control cells (HPDE: 57 ± 7%, $p_{\text{MIA–HPDE}} = 8.0 \times 10^{-4}$) (Fig. 2A). In contrast, the PANC-1 cells exhibit a significantly increased retention (88 ± 8%) compared to both the noncancerous control ($p_{\text{PANC–HPDE}} = 2.0 \times 10^{-5}$) and the MIA PaCa-2 cells ($p_{\text{PANC–MIA}} = 1.2 \times 10^{-7}$). The Hs766T cells show a marginally higher retention than the HPDE control cells (Hs766T: 60 ± 11%, $p_{\text{Hs766T–HPDE}} = 5.5 \times 10^{-2}$).

Since the ability of cells to occlude pores can depend on both cell deformability and cell size, we next measure the size of cells in suspension using imaging flow cytometry (Fig. S5A and B, ESI†) and plot percent retention as a function of cell diameter (Fig. 2B). Overall, we observe that there is a positive correlation between retention and cell size ($R = 0.72$), indicating that cell size could influence retention. While the observed relationship between cell size and retention may explain the higher retention of the larger PANC-1 cells, the other pancreatic ductal cell lines have similar size distributions yet show significant differences in retention. For example, the MIA PaCa-2 have a slightly larger size compared to the Hs766T cells, yet exhibit a significantly lower retention, which indicates that these cells occlude fewer pores and are therefore more deformable. In addition to cell size, nuclear size can also impact occlusion of pores and channels.[21,22] The median diameter of nuclei in our pancreatic ductal cells is 11–16 μm (Fig. S5A and C, ESI†), suggesting that some nuclear deformation is also required for cells to deform through micron-scale pores. We observe moderate correlations between nuclear size and transit time ($R = 0.86$), as well as nuclear size and retention ($R = 0.62$). However, there is a very strong correlation between cell and nuclear size ($R = 0.99$ for cells in suspension). Therefore, our cell deformability measurements by PMF and microfluidic deformability cytometry could be influenced by both the cytoskeleton and nucleus.

As an independent measure of how cells transit through narrow gaps, we use microfluidic deformability cytometry. This method enables us to measure the timescale, or transit time, for single cells to deform through micron-scale channels while simultaneously characterizing their size. Cells that have larger elastic moduli tend to have longer transit times.[29,39] When considering the entire population, the PANC-1 cells have a similar median transit time as the HPDE control (bootstrapped median transit time ± confidence interval, PANC-1: 18 ± 5.3 ms, HPDE: 18 ± 2.0 ms; $p_{\text{PANC–HPDE}} = 2.8 \times 10^{-2}$). Consistent with our retention data, the MIA PaCa-2 cells have a lower transit time compared to the HPDE cells (MIA PaCa-2: 4.0 ± 0.0 ms, $p_{\text{MIA–HPDE}} \approx 0.0$), substantiating that these cells are more deformable than the noncancerous controls. In addition, we observe that the Hs766T cells have significantly lower median transit times than the HPDE cells (Hs766T: 4.8 ± 0.5 ms, $p_{\text{HPDE–Hs766T}} \approx 0.0$).

To determine the role of cell size in transit time, we gate for cells of a similar size and compare their transit time distributions (Fig. S6, ESI†). Here we focus our analysis on the size bins of the largest (PANC-1) and smallest (Hs766T) cells of our panel. For example, we first compare transit time distributions for cells that are within 5 μm of the PANC-1 median cell size of 24 μm (Fig. S6D, ESI†). While the non-gated data show that PANC-1 and HPDE cells have similar median transit times across the entire population (Fig. 2C and D), our size-gated data reveal that the PANC-1 cells have a shorter median transit time than HPDE cells (PANC-1: 19 ± 8.5 ms, HPDE: 26 ± 5.0 ms; $p_{\text{PANC–HPDE}} = 4.8 \times 10^{-6}$), suggesting that PANC-1 cells are more deformable than the HPDE control cells when accounting for differences in cell size.

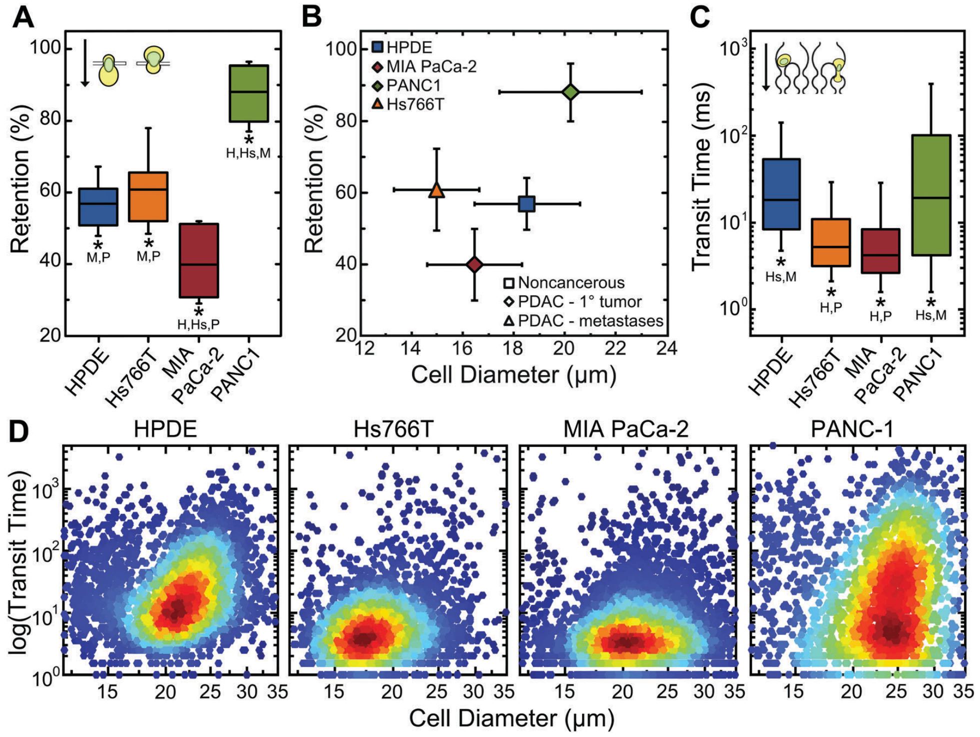

Fig. 2 Deformability of pancreatic ductal cells. (A) Retention as measured by parallel microfiltration (PMF). A suspension of cells that more effectively occludes the 10 μm pores of the membrane in response to external air pressure will exhibit a higher retention. Inset shows schematic of cells passing through a porous membrane. Boxes represent the 25th and 75th percentiles, whiskers represent the 10th and 90th percentiles, and horizontal lines represents the means. (B) Retention as a function of cell diameter. Data points represent the means and the error bars represent the standard deviations for both axes. (C) Transit time is measured using microfluidic deformability cytometry and reveals the timescale required for single cells to deform through a channel with a 9 μm × 10 μm diameter, as illustrated in the inset. Cells that are less deformable have longer transit times than cells that are more deformable. For each cell line, $n > 2200$ cells. Boxes represent the 25th and 75th percentiles, whiskers represent the 10th and 90th percentiles, and horizontal lines represent the bootstrapped medians. Size-gated transit time data is shown in Fig. S6 (ESI†). (D) Density scatterplots show the transit time of single cells as a function of cell size. Statistical significance of the deformability cytometry results is calculated using a Mann–Whitney *U* test. All other statistical significances is calculated with a Student's *t*-test. $^*p$-value < 0.05. The significance of pairwise comparisons between cell lines is shown in panels A and C by the initial(s) of the cell lines that are significantly different where H: HPDE, Hs: Hs766T, M: MIA PaCa-2, and P: PANC-1. For example, in panel A, HPDE is significantly different ($^*p < 0.05$) from MIA PaCa-2 (M) and PANC-1 (P).

Since the Hs766T cells are significantly smaller than the HPDE cells (Fig. 2D and Fig. S5A, B, ESI†), we also compare transit time distributions across cell lines within the median size range of the Hs766T cells (18.3 ± 2.5 μm) (Fig. S6B, ESI†). Our results show that even for cells of similar sizes, the Hs766T cells have a significantly reduced transit time (Hs766T: 4.8 ± 0.5, HPDE: 9.8 ± 1.5 ms; $p_{\text{HPDE–Hs766T}} = 1.2 \times 10^{-67}$), indicating that these cells are more deformable than the noncancerous HPDE cells. Thus, while both cell size and deformability can impact how cells deform through narrow gaps, our size-gated data show that even for cells of similar size, there are differences in transit time, reflecting the variability in cell mechanotype across our PDAC cell lines, both within and between populations. Collectively, our fluidic assays show that the MIA PaCa-2 cells passively deform through narrow gaps most readily, as indicated by their low retention and transit time. Interestingly, while the MIA PaCa-2 cells are the most deformable, they show a slightly lower invasive potential compared to the PANC-1 cells (Fig. 1), which have higher retention and transit times. By contrast, the Hs766T cells are the most invasive but have similar transit times and increased retention compared to the MIA PaCa-2 cells. Overall, for the three PDAC cell lines tested, we observe weak correlations between PDAC cell invasive potential and the deformability of suspended cells as measured using our fluidic assays [$R_{\text{Invasion–Retention}} = 0.21$, $R_{\text{Transwell–Retention}} = 0.05$, $R_{\text{Invasion–Transit Time}} = -0.24$; $R_{\text{Transwell–Transit Time}} = -0.39$] (Fig. 5 and Table S2, ESI†). Our results contrast previous studies showing that lung, breast and ovarian cancer cells with higher invasive potential have shorter transit times[14,16] and transformed ovarian cells have a lower retention.[15]

Stiffer pancreatic cancer cells tend to be more invasive

Before cancer cells reach circulation, they adhere to fibers and other cells as they disseminate and invade into surrounding tissues.

Therefore, we next use atomic force microscopy (AFM) to measure the Young's modulus of the central cytoplasmic region of pancreatic ductal cells in an adhered state. Our data show that the MIA PaCa-2 and PANC-1 cells have significantly lower median Young's moduli than the noncancerous HPDE cells (bootstrapped mean ± confidence intervals: MIA PaCa-2: 1.7 ± 1.0 kPa, PANC-1: 2.4 ± 1.1 kPa, HPDE: 3.7 ± 1.2 kPa; $p_{\text{MIA–HPDE}} = 1.6 \times 10^{-5}$, $p_{\text{PANC–HPDE}} = 1.3 \times 10^{-3}$) (Fig. 3A–C). The PANC-1 cells show a statistically significant 1.4× increase in the average Young's modulus compared to MIA PaCa-2 cells ($p = 2.7 \times 10^{-2}$). In contrast, the Hs766T cells have an average Young's modulus that is higher than both the MIA PaCa-2 and PANC-1 cells (Hs766T: 3.0 ± 2.0 kPa; $p_{\text{Hs766T–MIA}} = 1.2 \times 10^{-4}$, $p_{\text{Hs766T–PANC}} = 5.0 \times 10^{-3}$), but similar to that of the HPDE cells ($p_{\text{Hs766T–HPDE}} = 9.7 \times 10^{-1}$) (Fig. 3C). Compared to the other pancreatic ductal cancer cell lines, the stiffer Hs766T cells have a significantly greater invasive potential (Fig. 1). These data demonstrate that pancreatic cancer cells with a higher Young's modulus are more invasive than cancer cells that are more compliant ($R_{\text{Invasion–Young's Modulus}} = 0.97$; $R_{\text{Transwell–Young's Modulus}} = 0.92$), which contrasts previous studies that show more invasive breast and ovarian cancer cells have a lower Young's modulus than their benign and less invasive counterparts.[9,10]

Lamin A is associated with variability in PDAC cell mechanotype

To investigate the molecular origins underlying the observed differences in cell mechanotype of PDAC cells, we compile a list of genes that regulate cell mechanical properties,[40–45] which we collectively refer to as the 'mechanome'. Using publicly available RNAseq data,[46] we identify mechanome genes that have the greatest differential expression across our PDAC cell lines (Fig. 4A). The four genes that exhibit the largest standard deviation are *VIM*, *ACTB*, *ACTG1*, and *LMNA*. These genes also show the highest standard deviations across a cohort of 41 PDAC cell lines (Fig. S8, ESI†). Vimentin (*VIM*) is a cytoplasmic intermediate filament protein that contributes to the mechanical properties of various cell types.[47–49] Reduced levels of vimentin are associated with decreased stiffness of mouse embryo fibroblasts[50,51] and breast cancer cells.[52] Vimentin is also a biomarker for epithelial-to-mesenchymal transition (EMT): cells with increased levels of vimentin tend to be more motile and invasive.[53] Our previous work shows that EMT-transformed ovarian cancer cells are more deformable than epithelial-type cells.[15] *ACTB* and *ACTG1* form protein products that polymerize to form filamentous (F)-actin, which is a well-established regulator of cell mechanotype and motility.[54,55] We prioritize ß-actin for further analysis, as this protein is implicated in cancer progression.[54–56] We also investigate *LMNA*, which encodes lamin A; this nuclear-specific intermediate filament protein underlies the inner nuclear membrane, and is important in essential processes including chromatin organization, gene transcription, and DNA repair.[57] Lamin A is a key determinant of the shape stability of the cell nucleus,[58] and contributes to the mechanical properties of different cell and tissue types.[21,22,45,58,59] Therefore, we focus on validating the role of vimentin, ß-actin, F-actin, and lamin A in the mechanotypic variability of our pancreatic ductal cells.

We first quantify levels of vimentin by immunoblotting, revealing that there is significant variability across cell lines (Fig. 4B and C). MIA–PaCa-2 cells have the highest levels of vimentin, which are approximately 2-fold greater than levels in PANC-1 ($p = 0.08$). By contrast, HS766T and HPDE have no detectable vimentin. While the variability in vimentin levels across the cell lines is significant, it does not appear to explain the variability that we observe in cell mechanotype and invasive behavior, as the MIA PaCa-2 cells are the most deformable of our PDAC cell lines, and cells that are deficient in vimentin are typically more deformable.[50–52]

Our data show that ß-actin levels do not significantly vary across our panel of pancreatic ductal cells (0.9 to 1.2 fold-change; $p > 0.05$ for all pairwise comparisons) (Fig. 4D and E).

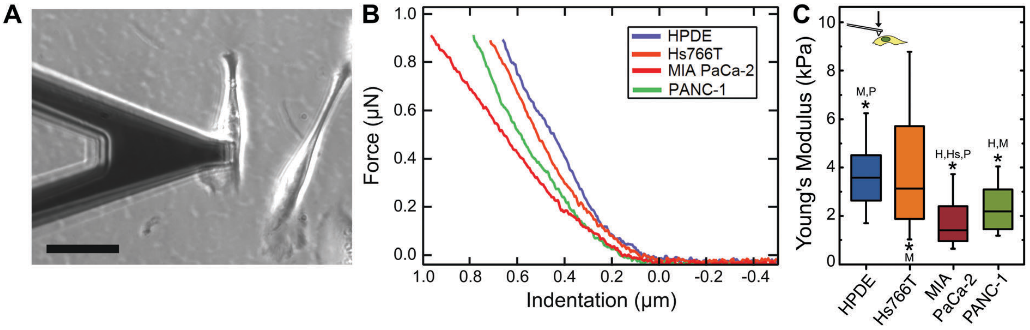

Fig. 3 Stiffness of pancreatic ductal cells. (A) Representative image of atomic force microscopy (AFM) tip over the cytoplasmic region of an HPDE cell. Scale, 40 µm. (B) Representative force curves from each cell line. Hertz–Sneddon fits are shown in Fig. S7 (ESI†). (C) Young's modulus of each cell type is measured by AFM. Stiffer cells have a larger Young's modulus than more compliant cells. $n > 28$ for all cell lines. Boxes represent the 25th and 75th percentiles, whiskers represent the 10th and 90th percentiles, and the horizontal line represents the bootstrapped median. Significance calculated by a Mann–Whitney U test between medians. $^*p < 0.05$. The significance of pairwise comparisons between cell lines is shown in panel C by the initial(s) of the cell lines that are significantly different where H: HPDE, Hs: Hs766T, M: MIA PaCa-2, and P: PANC-1. For example, HPDE is significantly different ($^*p < 0.05$) from MIA PaCa-2 (M) and PANC-1 (P).

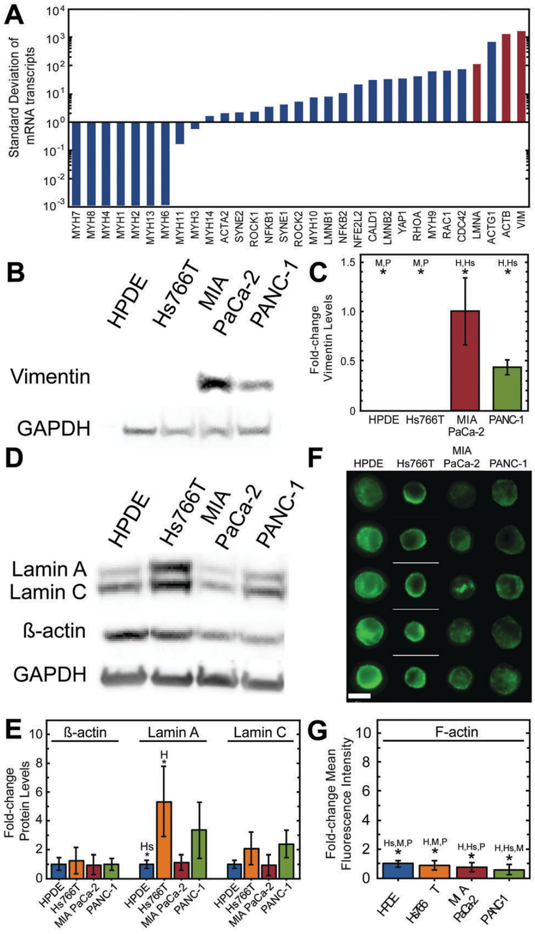

Fig. 4 Structural proteins in pancreatic ductal cell lines. (A) Bar plot showing standard deviation in expression levels of mechanoregulating genes across our three PDAC cell lines as determined by RNAseq analysis. (B) Immunoblot of vimentin and GAPDH. (C) Fold-change in protein levels compared to the MIA–PaCa2 cells, as HPDE cells show no detectable vimentin. Values are first normalized to the loading control, GAPDH. (D) Immunoblot of lamin A, lamin C, ß-actin, and GAPDH. (E) Fold-change in protein levels compared to HPDE cells. Values are first normalized to the loading control, GAPDH. (F) Imaging flow cytometry images of cells stained with phalloidin to label F-actin. Scale, 15 μm. (G) Quantification of images shows bootstrapped median fluorescence intensity of F-actin. Statistical significance for immunoblotting results is determined by a Student *t*-test. Statistical significance for imaging flow cytometry results is determined by a Mann Whitney *U* test. $*p < 0.05$. Significance is shown for cell line with the star to the cell line denoted by the initial(s). The significance of pairwise comparisons between cell lines is shown in panels C, E, and G by the initial(s) of the cell lines that are significantly different where H: HPDE, Hs: Hs766T, M: MIA PaCa-2, and P: PANC-1.

To quantify F-actin levels, we use imaging flow cytometry, which enables us to characterize large populations of single cells. While there is a slight decrease in F-actin levels for PDAC cell lines compared to the HPDE control, there is less than a 2-fold difference across our 4 pancreatic cell lines (Fig. 4F and G).

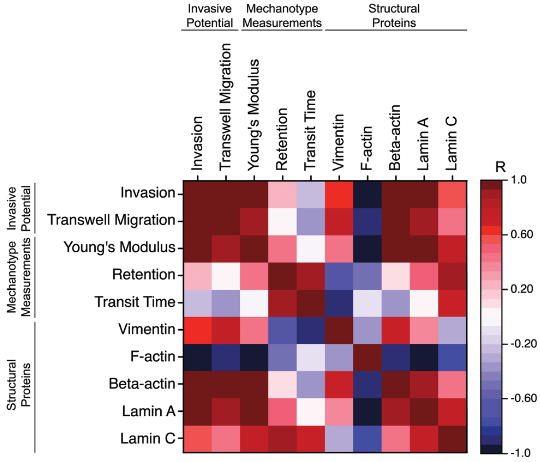

Fig. 5 Pearson's correlations (*R*) between cancer cell behaviors, mechanotype measurements, and levels of structural proteins for PDAC cells. Invasion is determined from modified scratch wound invasion assays as percent confluence at 72 hours. Transwell migration assays measure the ability of cells to migrate through 8 μm pores after 12 hours. Young's modulus is obtained using AFM. Retention is determined by PMF. Transit time is measured using microfluidic deformability cytometry. F-actin levels are measured for fixed, phalloidin-labeled cells in suspension by imaging flow cytometry. Vimentin, ß-actin, and lamin A/C levels are measured by quantitative immunoblotting. Colors are based on *R*-values that are obtained by calculating Pearson's correlation coefficients across the three cancerous PDAC cell lines (Hs766T, PANC-1, and MIA PaCa-2) in our panel.

By contrast, we observe up to a 5-fold difference in lamin A levels across our panel of cells, as measured by immunoblotting (Fig. 4D and E). Hs766T cells have the highest content of lamin A, which is approximately 5× greater than in HPDE cells (Hs766T: 5.3 ± 2.5, HPDE: 1.0 ± 0.3; $p_{\text{Hs766T–HPDE}} = 9.2 \times 10^{-2}$). The MIA PaCa-2 cells have similar lamin A levels as the HPDE control cells (MIA PaCa-2: 1.1 ± 0.5; $p_{\text{MIA–HPDE}} = 7.8 \times 10^{-1}$), while the PANC-1 cells have intermediate levels of lamin A (PANC-1: 3.3 ± 1.9; $p_{\text{PANC–HPDE}} = 1.7 \times 10^{-1}$) (Fig. 4D and E). Lamin C, which is a splice variant of lamin A, shows a much smaller ∼2-fold variation across cell lines. Overall, for the three PDAC cell lines tested, our data reveal a positive trend between protein levels of lamin A and cell mechanotype ($R_{\text{LaminA–Retention}} = 0.48$, $R_{\text{LaminA–Youngs Modulus}} = 1.0$) (Fig. 5 and Table S2, ESI†). Intriguingly, we also find a positive association between lamin A and cancer cell invasion ($R_{\text{LaminA–Invasion}} = 0.96$, $R_{\text{LaminA–Transwell Migration}} = 0.90$). Taken together, our data suggest that Young's modulus and invasive behavior are more strongly associated with lamin A than with ß-actin, F-actin, or lamin C.

Discussion

More invasive PDAC cells are stiffer than less invasive PDAC cells

Across many cancer types, in both cell lines and patient samples, cancer cells that are more deformable are more invasive or have higher metastatic potential than stiffer cells.[8–17,60] By contrast, we show here that more invasive PDAC cells have a higher Young's modulus. The Hs766T cells, which are derived from a malignant pleural effusion, are the stiffest and also the most invasive of the cell lines in our panel (Fig. 1 and 3). Of the two cell lines derived from primary tumors, PANC-1 cells are slightly more invasive and have a higher Young's modulus than MIA PaCA-2 cells. Our observations that more invasive pancreatic ductal cells tend to be stiffer suggest that the relationship between cancer cell mechanotype and invasive potential may depend on cancer type. While many studies identify more compliant breast and ovarian cancer cells as more invasive,[9,10] stiffer lung cancer and transformed skin cells have greater invasive potential.[18,19] Indeed, more invasive or metastatic cancer cell lines that generate greater traction stresses[27,61] and more contractile cells have a higher apparent stiffness.[62]

Cell mechanotype shows promise as an emerging biomarker that could be used to aid pathologists in achieving more accurate prognoses.[13,63] Our data highlight that the association between mechanotype and disease aggressiveness may vary for different tissue types. For example, while the increased deformability of breast and ovarian cancer cells may predict increased invasive behavior, our results suggest that more invasive PDAC cells could be detected or classified based on their increased stiffness. Developing a framework across different types of cancers that classifies disease aggressiveness based on cell mechanotype could provide clinically valuable information for prognosis or identifying appropriate therapeutic treatments.

An integrated understanding of cell mechanotype

Across three different mechanotype measurements, we find different trends between cell lines. Our AFM data show that the stiffest to most compliant cell lines are Hs766T = HPDE > PANC-1 > MIA PaCa-2. With PMF, we find that retention from highest to lowest is PANC-1 > Hs766T = HPDE > MIA PaCa-2. Our microfluidic deformability cytometry data show that transit times from longest to shortest are HPDE = PANC-1 > Hs766T > MIA PaCa-2. Overall we find that there is a strong, positive correlation between our microfluidic and PMF data (Fig. 5 and Table S2, ESI†). However, there is only a moderate to weak association between AFM and our fluidic assays. One possible explanation for the difference we see across methods may be a result of measuring bulk populations *versus* single cells. For example, the PANC-1 cells have a similar median transit time as the HPDE cells, but exhibit a greater range of transit times; the PANC-1 cells that have longer transit times are more likely to occlude pores in our PMF assay, and may thereby contribute to the marked increase in retention that we observe for PANC-1 compared to HPDE cells.

The different trends in cell mechanotype that we observe may also stem from the different length scales of deformation between the techniques: in our fluidic assays, cells are subject to global deformations on the order of 10 μm whereas with AFM we probe the cell with local, ~0.5 to 1 μm indentations. The deformation length scale determines which subcellular structures are primary contributors to the measured cell deformability. For example, the nucleus may dominate our fluidic deformability measurements as the nuclei of our pancreatic ductal cells have a diameter of 11 to 16 μm and the pores used in our PMF and transit time assays have a diameter of 9 to 10 μm. Therefore, the nucleus must deform in order for the whole cell to passage through a pore. As the nucleus rate-limits the transit of cells through pores much smaller than the diameter of the nucleus,[21] contributions of nuclear mechanical properties to our fluidic measurements may be more significant than the cytoskeleton. However, we observe only weak correlations between retention and transit time with levels of the nuclear envelope protein lamin A (Fig. 5 and Table S2, ESI†), suggesting that both nuclear and cytoskeletal structures may contribute to transit time and retention measurements. With AFM, we induce local deformations of the cytoplasmic region of adhered cells, thus we expect that these measurements reflect cytoskeletal architecture. We note that adhered cells also exhibit stress fibers, which can be anchored at focal adhesions where cells attach to their substrate;[25] the associated stress fibers may also contribute to the deformability of adhered cells. We note that the nucleus could additionally contribute to our AFM measurements of the cytoplasmic region. The cytoskeleton is physically connected to the nucleus through LINC protein complexes that span the nuclear envelope and interact with actin and intermediate filaments; thus, mechanical stresses applied during deformation of the cytoplasm may be transduced to the nucleus.[64]

Adhered cells can also generate intracellular tension or 'prestress' when they are attached to a Matrigel-coated substrate. As higher levels of prestress are reflected in AFM measurements of Young's modulus,[65] the increased stiffness of Hs766T cells may additionally reflect increased intracellular tension of these cells. Moreover, adhered cells are prestressed materials with actin stress fibers[66] and the nucleus under tension.[67–69] We speculate that higher levels of lamin A could also enable cells to achieve higher levels of prestress, and thereby contribute to the stiffer cytoplasmic region that we observe by AFM. Therefore, a higher density of lamin A in the nucleus could result in a smaller deformation of the cytoplasmic region for a given applied force; consistent with this, Hs766T cells have the highest levels of lamin A (Fig. 4D and E) largest Young's modulus as measured by AFM (Fig. 3C).

Given these differences between cells that are adhered *versus* suspended, as well as differences between the deformation length scales of mechanotyping techniques, such complementary methods could provide information that may be relevant in the context of distinct physical processes in metastasis and invasion, from circulation through vasculature to extravasation into distant sites. While our retention and transit time results do not strongly correlate with cell invasive potential (Fig. 5 and Table S2, ESI†), the ability of PDAC cells to passively deform may influence their ability to transit through narrow capillaries of the vasculature during metastasis. Our retention measurements may also have physiological disease relevance: it is intriguing to speculate that the occlusion of cells in micron-scale capillaries of the pulmonary bed could increase the probability that a secondary cancer site will be established.

The molecular origins of variability in cell mechanotype

Here we show that there is a 5-fold difference in lamin A protein levels across 4 pancreatic ductal cell lines. Our results also show a strong correlation between lamin A levels and Young's modulus as measured by AFM (Fig. 5 and Table S2, ESI†), indicating that this key structural protein of the cell nucleus may contribute to the observed variability in mechanotype that we observe across the PDAC cell lines. Our results are consistent with previous findings showing that lower levels of lamin A result in more deformable cells.[21,58,70]

We also observe that cells with higher levels of lamin A tend to be more invasive (Fig. 5). For example, the Hs766T cells have the highest expression of lamin A (1.6 to 5.3-fold increase compared to the other pancreatic ductal cells lines) (Fig. 4D and E) and are the most invasive (20 to 38% higher wound confluence at 72 hours than the other pancreatic ductal cell lines, Fig. 1). These findings contrast previous studies that show increased levels of lamin A can impede the active migration and passive transit of cells through narrow pores that are ~50% smaller than the diameter of their nuclei.[21,22] However, cells with reduced levels of lamin A exhibit increased frequency of nuclear envelope rupture,[71,72] apoptosis, and cell death[22] when migrating through micron-scale pores and 3D collagen gels. Thus, while a more compliant nucleus, with lower lamin A levels, can enable changes in shape that are required for deformation through narrow gaps, a threshold level of lamin A and/or mechanical stability appears to be necessary to prevent cell death and excessive nuclear rupture events, which ultimately cause DNA damage. Further, a stiffer nucleus could provide other advantages during invasion. Because polymerizing actin bundles generate forces and push against the nucleus during invadopodia formation,[73] we speculate that a stiffer nucleus with higher levels of lamin A could provide more resistance to the forces exerted by growing invadopodia and thereby enhance the ability of cells to penetrate and invade into the surrounding matrix. Indeed, lamin A-deficient mouse embryo fibroblasts cells show reduced protrusions while migrating through a collagen matrix, as well as lower 3D migration speeds.[74] Thus, both lower and higher levels of lamin A may offer distinct advantages for cancer cells.

While lamin A appears to be implicated in the progression of some types of cancer, there is currently no consensus on the role of lamin A in cancer progression or prognosis.[75] Lamin A overexpression is correlated to increased growth and invasion in prostate cancer,[76] while reduced lamin A levels are linked to poor prognosis in gastric and squamous cell carcinoma, as well as some skin cancers.[77] The variability in mechanotype that we observe could stem from other differences between cell lines. Although the cell lines in our panel are all pancreatic ductal cells, they are derived from different sites, including primary tumors and pleural effusion. Despite their different origins, all three PDAC cell lines have mutations in *KRAS*, *TP53*, and *p16*. The Hs766T cells have an additional *SMAD4* mutation (Table S1, ESI†), which could contribute to its increased invasive potential.[78,79] In addition to these founder mutations, other genetic alterations could affect mechanotype. Future studies measuring the deformability of primary cells with well-characterized genetic mutations may address the link between genotype, mechanotype, and invasive behavior.

We also find that there is significant variability in vimentin levels across PDAC cell lines (Fig. 4B and C), and that cells with higher vimentin levels are more compliant and less invasive. This apparent discrepancy with previous mechanical studies of cells with decreased vimentin levels[50–52] may be due to the fact that we investigate endogeneous vimentin levels across different cell lines, rather than specifically manipulating vimentin levels by knock-down or overexpression. However, during epithelial-to-mesenchymal transition (EMT), cells tend to express increased levels of vimentin and become more motile and invasive;[53] our previous work shows that EMT-transformed ovarian cancer cells are more deformable than epithelial-type cells.[15] Our current study also reveals that pancreatic cancer cells with higher vimentin levels are more deformable, although they are less invasive. It will be interesting to more thoroughly investigate the role of vimentin in the mechanical properties and invasion of pancreatic cancer cells in future work.

Our bioinformatics analysis highlights additional mechanome genes that could regulate PDAC cell mechanotype. For example, we observe that components of the Rho/ROCK pathway also exhibit significant variability across PDAC cell lines. These proteins, such as RhoA, are implicated in cell contractility,[80–82] and may thus impact cancer cell invasion, response to stiffer extracellular matrices, and metastasis. Further investigations should provide deeper insight into the molecular basis of how cells regulate their mechanotype to adapt to a microenvironment of a particular stiffness, and how such changes in cell mechanotype may affect cancer behaviors, from invasion to proliferation. It is thought that more compliant cells could more easily transit narrow channels of the vasculature and metastasize to distant sites; however, stiffer cells may be better able to sustain the physical forces in the microenvironment and generate greater contractile forces that enable invasion into surrounding tissues. Such studies would also provide deeper insight into the open question of whether tumor cell mechanotype contributes to cancer progression, or is a byproduct that accompanies disease progression.

Towards clinical benefit

We anticipate that expanding our knowledge of the PDAC cell mechanome could identify novel drug targets. One of the greatest challenges in PDAC treatment is the development of effective therapies that impede metastasis, as metastatic tumor burden is thought to be responsible for over 70 percent of PDAC-related deaths.[83] Knowledge of the PDAC mechanome could provide insight into how cells alter mechanosignaling pathways in response to the stiffness of their microenvironment. Targeting the molecular components that are triggered by mechanical cues may impede cancer progression by interrupting the positive feedback loop that drives cells to generate more ECM, which results in a stiffer tumor and increases PDAC progression.[4] Insights into cell physical properties and their contributions to the complex cancer phenotype are thus urgently needed for improving the prognosis of patients with pancreatic cancer.

Experimental methods

Cell culture

The nontransformed human pancreatic ductal epithelial (HPDE) cell line is from Ming-Sound Tsao from the Department of

Laboratory Medicine and Pathobiology at the Ontario Cancer Institute (University Health Network-Princess Margaret Hospital, Toronto) and the Department of Medical Biophysics (University of Toronto, Ontario, Canada). The pancreatic ductal adenocarcinoma (PDAC) cell lines (Hs766T, MIA PaCa-2, and PANC-1) are from the American Type Culture Collection (ATCC). HPDE cells are cultured in Keratinocyte-SFM (Life Technologies) supplemented with prequalified human recombinant Epidermal Growth Factor 1-53 (Life Technologies), Bovine Pituitary Extract (Life Technologies), and 1% v/v penicillin–streptomycin (Gemini BioProducts). Hs766T, MIA PaCa-2, and PANC-1 cells are grown in high glucose, L-glutamine Dulbecco's Modified Eagle Medium (DMEM) (Life Technologies) with 10% fetal bovine serum and 1% v/v penicillin–streptomycin (Gemini BioProducts). Cells are cultured at 5% CO_2 and 37 °C.

Scratch wound invasion, migration, and proliferation assays

We perform invasion, migration, and proliferation assays using the IncuCyte time-lapse imaging system (EssenBioscience). To measure cell invasion through a 3D matrix, we perform modified scratch wound invasion assays with an overlay of Matrigel to simulate the ECM.[30,31,84] We plate cells in the wells of a 96-well plate with a thin Matrigel (100 $\mu g\ ml^{-1}$) layer for cell attachment at 95% confluency, create a scratch wound, overlay the scratch with a ~1.5 mm-thick layer of 8 mg ml^{-1} Matrigel (Corning), and perform time-lapse imaging using the IncuCyte Zoom (Essen Bioscience) at 5% CO_2 and 37 °C. Phase contrast images of cells are acquired every 2 hours for 120 hours. We determine the confluence of cells in the wound area at each time point using quantitative image analysis (Essen Bioscience). To assay the ability of cells to migrate on a 2D substrate, we perform this same assay without Matrigel and image every 2 hours for 72 hours. Since both scratch wound invasion and migration assays may be influenced by cell proliferation, we also measure percent confluence by sparsely plating cells (2000 cells per well of a 96-well plate) and acquiring phase contrast images every 2 hours for 120 hours. We also determine proliferation and apoptosis rates of cells with a Matrigel overlay. Cells are prepared as described above for a proliferation assay. Prior to overlay with Matrigel (8 mg ml^{-1}), cells were stained with 3 μM DRAQ7, a cell impermeable nuclear dye that only intercalates into the DNA of apoptosed cells.

Transwell migration

To assay the ability of cells to migrate through 8 μm pores, we use 24-well uncoated transwell inserts with porous polycarbonate membranes (Costar, Corning). For 1 hour prior to the experiments, we hydrate each well in serum-free DMEM media. We then load 150 μl of a suspension of 6.7×10^5 cells per ml into each well and incubate at 5% CO_2, 37 °C for 12 hours. After the incubation period, cells remaining on the top side of each membrane are removed with a cotton swab; all of the cells that have migrated to the bottom of the membrane are fixed in 100% methanol, stained with Hoechst 33342 (Life Technologies), and washed with 1× PBS (Corning). Imaging of stained cells is performed using a fluorescent microscope (Zeiss EC Plan-Neofluar 20× objective; NA 0.5/Ph2 M27). The number of cells that migrate to the bottom of the membrane is determined by counting the number of nuclei from images of the bottom membrane. Transwell migration efficiency is determined by the number of migrated cells divided by the total number of cells loaded.

Parallel microfiltration (PMF)

The PMF method is described previously in detail.[15] In brief, we assemble the device with a polycarbonate membrane that has pores of 10 μm diameter (Isopore, Millipore). To minimize cell-surface interactions, we incubate each well with 1% w/v bovine serum albumin (BSA) (Fisher Scientific) for 1 hour at 37 °C. The BSA solution is then removed and wells are air dried for at least 1 hour before each experiment. Cell suspensions are prepared at a concentration of 6.0×10^5 cells per ml and filtered through a 35 μm mesh filter to reduce the number of cell aggregates. To measure cell number and size, we use an automated cell counter (TC20, BioRad); this also confirms that over 98% of cells are single cells (Fig. S4, ESI†). Using compressed air as a pressure source, we apply 14 kPa for 50 s. We determine the percentage (%) retention by collecting the cell suspension that remains in the top well and measuring its mass using a precision balance (Northeast Scale Inc.); retention is defined as $mass_{final}/mass_{initial}$. We load samples into at least three wells per cell line per experiment, and at least ten wells over three independent experiments are measured for each cell line.

Microfluidic deformability cytometry

To evaluate the ability of single cells to passively deform through micron-scale pores, we use microfluidic devices with channels that have a smallest dimension of 9 μm × 10 μm (width × height), which we fabricate using standard soft photolithography techniques.[85] To pattern the device design onto a silicon master, SU-8 3010 negative photoresist (MicroChem) is spincoated onto a 4″ silicon wafer and exposed to UV light through a photomask. Polydimethylsiloxane (Sylgard 184 silicone elastomer, Dow Corning) is mixed with a 10 : 1 ratio of base to crosslinker, poured over the silicon master, and cured at 80 °C for 1 hour. A biopsy punch is used to create inlets and outlets. The PDMS is bonded to #1.5-thickness glass coverslips using plasma corona discharge and baked at 80 °C for 20 minutes to ensure bonding. To minimize cell-wall interactions, we add Pluronic F-127 surfactant (0.1 w/v%) (Sigma-Aldrich) to the cell suspension.[29] Cell suspensions are flowed through the microfluidic device using pressure-driven flow (10 psi).[86] We image cells that deform through the narrow channels by acquiring images at 2000 frames per second using a CMOS camera (Miro eX1, Vision Research) mounted on an inverted microscope. For each cell line, we obtain videos over three independent experiments. To determine the timescale for single cells to transit through the 9 μm constriction, or transit time, we perform post-acquisition analysis using a custom MATLAB script (Mathworks).

Atomic force microscopy (AFM)

AFM is performed using the MFP-3D-BIO system (Asylum Research, Oxford Instruments). Cells are probed with the "C" tip of an MLCT probe (Bruker) at room temperature. The sensitivity and spring constant of each probe (11.5 to 14.5 mN m^{-1}) are calibrated before each experiment. Cells are plated on a polystyrene petri dish coated with a thin layer of Matrigel (100 μg ml^{-1}) approximately 24 hours prior to each experiment. Force curves are acquired by indenting the central cytoplasmic region of 25 to 35 cells for each cell line. To avoid possible contribution of adjacent cells, only single cells were probed. Approach and retract speeds for all experiments are 5 μm s^{-1}. The elastic modulus for each cell is determined by fitting force curves with the Hertz–Sneddon model[87,88] using Asylum Research software.

Gene expression and bioinformatics analysis

We use publicly available RNA-seq data for 41 PDAC cell lines for gene expression analysis.[46] Using STAR v.2.4.2a,[89] we align RNA sequence reads to the human reference genome (hg38) with Ensembl v.82 gene annotations. STAR is run with the following parameters: minimum/maximum intron sizes are set to 30 and 500 000; noncanonical, unannotated junctions are removed; maximum tolerated mismatches is set to 10; and the outSAMstrandField intron motif option is enabled. To quantify per-sample read abundances we use the Cuffquant command included with Cufflinks v.2.2.1,[90] with fragment bias correction and multiread correction enabled. All other options are set to default. Finally, fragments per kilobase of exon per million fragments mapped (FPKM) are calculated using the Cuffnorm command with default parameters. We use these FPKM values to compare expression levels of genes whose protein products are implicated in regulation of cell mechanical properties.[40–45] To identify the mechanoregulating genes with the highest variability in expression across PDAC cell lines, we calculate the standard deviation of mRNA levels for genes that encode proteins that are implicated in mechanotype.

Imaging flow cytometry

To visualize F-actin, cells are fixed with 4% paraformaldehyde (Sigma) in 1× PBS (Corning), permeabilized with 0.3% Triton X-100 in 1× PBS (Corning), and stained with phalloidin conjugated to AlexaFluor488 (1 : 100 in 0.3% Triton X-100 in 1× PBS; Life Technologies) at room temperature for 30 minutes. To image the nucleus, cells are stained with DRAQ5 (1 : 250 in 0.3% Triton X-100 in 1× PBS; ThermoFisher) at room temperature for 20 minutes. Images of individual cells in suspension are acquired using imaging flow cytometry (Amnis ImageStream, Millipore). Quantification of F-actin intensity, cell size, and nuclear size is conducted using the IDEAS software (Amnis, Millipore).

Western blots

Western blots are performed as previously described[21] with slight modifications. Cell lysates are prepared from 2×10^6 cells with 100 μl urea lysis buffer that has a final concentration of 9 M urea, 10 mM Tris–HCl (pH 8), 10 μM EDTA, 500 μM phenylmethylsulfonyl fluoride, 20 μl of β-mercaptoethanol (Sigma), and protease inhibitor at the suggested working concentration (cOmplete ULTRA tablets). Proteins are separated on a 4–12% Bis-Tris gel (Life Technologies) with 1× MES running buffer (Life Technologies) and then transferred to nitrocellulose membranes, blocked with 5% fat-free milk, and labeled with primary antibodies against vimentin (MS-129-P0, ThermoFisher), β-actin (MA5-15739, ThermoFisher), lamin A/C (sc-6215, Santa Cruz Biotech), and GAPDH (MA5-15738, ThermoFisher) as a loading control. Membranes are then incubated with host-specific secondary antibodies conjugated to horseradish peroxidase (HRP) (Abcam) and imaged using chemiluminescence (ThermoFisher) on a digital imaging system (AlphaImager IS-1000, Alpha Innotech Corporation). Expression levels are quantified by analysis of optical density in the linear regime using ImageJ software (National Institutes of Health).

Statistical analysis

All data are obtained from at least 3 independent experiments. For data with normal distributions, we determine statistical significance using a Student's *t*-test (Excel, Microsoft). For data that exhibit a non-normal distribution, we perform bootstrapping to obtain the bootstrapped median and confidence intervals; we then use the Mann–Whitney *U* test to determine statistically significant differences between non-normal distributions the Statistical and Machine Learning Toolbox in MATLAB (Mathworks) and Origin (OriginLab). Density scatter plots for transit time data are plotted using the dscatter function (Richard Henson, MathWorks File Exchange) in MATLAB (Mathworks).

Acknowledgements

We thank Shivani Sharma and Adam Steig for consultations on AFM and Tae-Hyung Kim for assistance with gene expression analysis and critical feedback on the manuscript. We thank James Tidball for generous use of the AlphaImager imaging system. Imaging flow cytometry was performed in the UCLA Flow Cytometry Core Facility that is supported by National Institutes of Health awards CA-16042 and AI-28697, the Jonsson Comprehensive Cancer Center, the Center for AIDS Research, and the David Geffen School of Medicine at UCLA. IncuCyte Zoom experiments were performed in facilities supported by the Eli & Edythe Broad Center of Regenerative Medicine & Stem Cell Research at UCLA and the Jonsson Comprehensive Cancer Center. We are grateful for our funding from the NSF (CAREER DBI-1254185 to ACR), the NIH/National Center for Advancing Translational Science (NCATS) (UCLA CTSI Grant Number UL1TR000124), and the Farber Family Foundation. AVN is supported by a David Geffen Scholarship and the UCLA-IBP Eureka Scholarship Fund. AHN is supported by an NIH T32 from Department of Gastroenterology (NIH GI Training Grant (T32 DK07180-37)), as well as the Gerald S. Levey Surgical Research Training Award. AMW is supported by the UCLA Undergraduate Research Scholars Program (Gottlieb Endowment) and Whitcome Summer Research Fellowship.

References

1 C. Bosetti, P. Bertuccio, E. Negri, C. La Vecchia, M. P. Zeegers and P. Boffetta, *Mol. Carcinog.*, 2012, **51**, 3–13.

2 L. Rahib, B. D. Smith, R. Aizenberg, A. B. Rosenzweig, J. M. Fleshman and L. M. Matrisian, *Cancer Res.*, 2014, **74**, 2913–2921.

3 D. T. Butcher, T. Alliston and V. M. Weaver, *Nat. Rev. Cancer*, 2009, **9**, 108–122.

4 H. Laklai, Y. A. Miroshnikova, M. W. Pickup, E. A. Collisson, G. E. Kim, A. S. Barrett, R. C. Hill, J. N. Lakins, D. D. Schlaepfer, J. K. Mouw, V. S. LeBleu, N. Roy, S. V. Novitskiy, J. S. Johansen, V. Poli, R. Kalluri, C. A. Iacobuzio-Donahue, L. D. Wood, M. Hebrok, K. Hansen, H. L. Moses and V. M. Weaver, *Nat. Med.*, 2016, **22**, 497–505.

5 F. Kai, H. Laklai and V. Weaver, *Trends Cell Biol.*, 2016, **26**, 1–12.

6 D. E. Discher, P. Janmey and Y.-L. Wang, *Science*, 2005, **310**, 1139–1143.

7 E. L. Baker, J. Lu, D. Yu, R. T. Bonnecaze and M. H. Zaman, *Biophys. J.*, 2010, **99**, 2048–2057.

8 V. Swaminathan, K. Mythreye, E. Tim O'Brien, A. Berchuck, G. C. Blobe and R. Superfine, *Cancer Res.*, 2011, **71**, 5075–5080.

9 W. Xu, R. Mezencev, B. Kim, L. Wang, J. McDonald and T. Sulchek, *PLoS One*, 2012, **7**, e46609.

10 M. H. Lee, P. H. Wu, J. R. Staunton, R. Ros, G. D. Longmore and D. Wirtz, *Biophys. J.*, 2012, **102**, 2731–2741.

11 S. E. Cross, Y.-S. Jin, J. Rao and J. K. Gimzewski, *Nat. Nanotechnol.*, 2007, **2**, 780–783.

12 T. W. Remmerbach, F. Wottawah, J. Dietrich, B. Lincoln, C. Wittekind and J. Guck, *Cancer Res.*, 2009, **69**, 1728–1732.

13 H. T. K. Tse, D. R. Gossett, Y. S. Moon, M. Masaeli, M. Sohsman, Y. Ying, K. Mislick, R. P. Adams, J. Rao and D. Di Carlo, *Sci. Transl. Med.*, 2013, **5**, 212ra163.

14 S. Byun, S. Son, D. Amodei, N. Cermak, J. Shaw, J. H. Kang, V. C. Hecht, M. M. Winslow, T. Jacks, P. Mallick and S. R. Manalis, *Proc. Natl. Acad. Sci. U. S. A.*, 2013, **110**, 7580–7585.

15 D. Qi, N. Kaur Gill, C. Santiskulvong, J. Sifuentes, O. Dorigo, J. Rao, B. Taylor-Harding, W. Ruprecht Wiedemeyer and A. C. Rowat, *Sci. Rep.*, 2015, **5**, 17595.

16 H. W. Hou, Q. S. Li, G. Y. H. Lee, A. P. Kumar, C. N. Ong and C. T. Lim, *Biomed. Microdevices*, 2009, **11**, 557–564.

17 M. Plodinec, M. Loparic, C. A. Monnier, E. C. Obermann, R. Zanetti-Dallenbach, P. Oertle, J. T. Hyotyla, U. Aebi, M. Bentires-Alj, R. Y. H. Lim and C.-A. Schoenenberger, *Nat. Nanotechnol.*, 2012, **7**, 757–765.

18 L.-S. Z. Rathje, N. Nordgren, T. Pettersson, D. Rönnlund, J. Widengren, P. Aspenström and A. K. B. Gad, *Proc. Natl. Acad. Sci. U. S. A.*, 2014, **111**, 1515–1520.

19 H. W. Yu, Y. Q. Chen, C. M. Huang, C. Y. Liu, A. Chiou, Y. K. Wang, M. J. Tang and J. C. Kuo, *J. Cell. Mol. Med.*, 2015, **19**, 934–947.

20 G. Salbreux, G. Charras and E. Paluch, *Trends Cell Biol.*, 2012, **22**, 536–545.

21 A. C. Rowat, D. E. Jaalouk, M. Zwerger, W. L. Ung, I. A. Eydelnant, D. E. Olins, A. L. Olins, H. Herrmann, D. A. Weitz and J. Lammerding, *J. Biol. Chem.*, 2013, **288**, 8610–8618.

22 T. Harada, J. Swift, J. Irianto, J. W. Shin, K. R. Spinler, A. Athirasala, R. Diegmiller, P. C. D. P. Dingal, I. L. Ivanovska and D. E. Discher, *J. Cell Biol.*, 2014, **204**, 669–682.

23 J. L. Mackay and S. Kumar, *Methods Mol. Biol.*, 2013, **931**, 313–329.

24 M. L. Rodriguez, P. J. Mcgarry and N. J. Sniadecki, *Appl. Mech. Rev.*, 2013, **65**, 1–41.

25 S. Tojkander, G. Gateva and P. Lappalainen, *J. Cell Sci.*, 2012, **125**, 1855–1864.

26 N. Wang, I. M. Tolic-Norrelykke, J. Chen, S. M. Mijailovich, J. P. Butler, J. J. Fredberg and D. Stamenovic, *Am. J. Physiol.: Cell Physiol.*, 2002, **282**, 606–616.

27 C. M. Kraning-rush, J. P. Califano and C. A. Reinhart-king, *PLoS One*, 2012, **7**, e32572.

28 E. L. Deer, J. González-Hernández, J. D. Coursen, J. E. Shea, J. Ngatia, C. L. Scaife, M. A. Firpo and S. J. Mulvihill, *Pancreas*, 2010, **39**, 425–435.

29 K. D. Nyberg, M. B. Scott, S. L. Bruce, A. B. Gopinath, D. Bikos, T. G. Mason, W. Kim, H. Sung and A. C. Rowat, *Lab Chip*, 2016, **16**, 3330–3339.

30 M. Unbekandt, D. R. Croft, D. Crighton, M. Mezna, D. Mcarthur, P. Mcconnell, A. W. Schüttelkopf, S. Belshaw, A. Pannifer, M. Sime, J. Bower, M. Drysdale and M. F. Olson, *Cell Commun. Signaling*, 2014, **12**, 1–15.

31 M. Kobayashi, C. Salomon, J. Tapia, S. E. Illanes, M. D. Mitchell and G. E. Rice, *J. Transl. Med.*, 2014, **12**, 1–12.

32 K. Nabeshima, T. Inoue, Y. Shimao and T. Sameshima, *Pathol. Int.*, 2002, **52**, 255–264.

33 X. Zhao, S. Gao, W. Sun, H. Zhang, J. Sun, S. Yang and J. Hao, *Cancer Res.*, 2014, **74**, 2455–2464.

34 C. Ma, B. Wu, X. Huang, Z. Yuan, K. Nong, B. Dong, Y. Bai, H. Zhu, W. Wang and K. Ai, *Tumor Biol.*, 2014, **35**, 12729–12735.

35 M. H. Zaman, L. M. Trapani, A. L. Sieminski, D. Mackellar, H. Gong, R. D. Kamm, A. Wells, D. A. Lauffenburger and P. Matsudaira, *Proc. Natl. Acad. Sci. U. S. A.*, 2006, **103**, 15–16.

36 V. Ellenrieder, B. Alber, U. Lacher, S. F. Hendler, A. Menke, W. Boeck, M. Wagner, M. Wilda, H. Friess, M. Büchler, G. Adler and T. M. Gress, *Int. J. Cancer*, 2000, **85**, 14–20.

37 T. Fujisawa, B. Rubin, A. Suzuki, P. S. Patel, W. A. Gahl, B. H. Joshi and R. K. Puri, *PLoS One*, 2012, **7**, 1–10.

38 A. Haage and I. C. Schneider, *FASEB J.*, 2014, **28**, 3589–3599.

39 M. J. Rosenbluth, W. A. Lam and D. A. Fletcher, *Lab Chip*, 2008, **8**, 1062–1070.

40 T. P. Stossel and J. H. Hartwig, *Cell*, 2003, **4**, 444–445.

41 R. McBeath, D. M. Pirone, C. M. Nelson, K. Bhadriraju and C. S. Chen, *Dev. Cell*, 2004, **6**, 483–495.

42 A. Cuadrado, Z. Martín-Moldes, J. Ye and I. Lastres-Becker, *J. Biol. Chem.*, 2014, **289**, 15244–15258.

43 A. J. Engler, S. Sen, H. L. Sweeney and D. E. Discher, *Cell*, 2006, **126**, 677–689.

44 W. Zhang, K. Kai, D. S. Choi, T. Iwamoto, Y. H. Nguyen, H. Wong, M. D. Landis, N. T. Ueno, J. Chang and L. Qin, *Proc. Natl. Acad. Sci. U. S. A.*, 2012, **109**, 18707–18712.

45 J. Swift, I. L. Ivanovska, A. Buxboim, T. Harada, P. C. D. P. Dingal, J. Pinter, J. D. Pajerowski, K. R. Spinler, J.-W. Shin, M. Tewari,

F. Rehfeldt, D. W. Speicher and D. E. Discher, *Science*, 2013, **341**, 1240104.

46 J. Barretina, G. Caponigro, N. Stransky, K. Venkatesan, A. A. Margolin, S. Kim, C. J. Wilson, J. Lehár, G. V. Kryukov, D. Sonkin, A. Reddy, M. Liu, L. Murray, M. F. Berger, J. E. Monahan, P. Morais, J. Meltzer, A. Korejwa, J. Jané-Valbuena, F. A. Mapa, J. Thibault, E. Bric-Furlong, P. Raman, A. Shipway, I. H. Engels, J. Cheng, G. K. Yu, J. Yu, P. Aspesi, M. de Silva, K. Jagtap, M. D. Jones, L. Wang, C. Hatton, E. Palescandolo, S. Gupta, S. Mahan, C. Sougnez, R. C. Onofrio, T. Liefeld, L. MacConaill, W. Winckler, M. Reich, N. Li, J. P. Mesirov, S. B. Gabriel, G. Getz, K. Ardlie, V. Chan, V. E. Myer, B. L. Weber, J. Porter, M. Warmuth, P. Finan, J. L. Harris, M. Meyerson, T. R. Golub, M. P. Morrissey, W. R. Sellers, R. Schlegel and L. A. Garraway, *Nature*, 2012, **483**, 603–607.

47 L. Kreplak and D. Fudge, *BioEssays*, 2007, **29**, 26–35.

48 E. Gladilin, P. Gonzalez and R. Eils, *J. Biomech.*, 2014, **47**, 2598–2605.

49 M. G. Mendez, S.-I. Kojima and R. D. Goldman, *FASEB J.*, 2010, **24**, 1838–1851.

50 B. Eckes, D. Dogic, E. Colucci-guyon, N. Wang, A. Maniotis, D. Ingber, A. Merckling, F. Langa, M. Aumailley, A. Delouvée, V. Koteliansky, C. Babinet and T. Krieg, *J. Cell Sci.*, 1998, **111**, 1897–1907.

51 D. Stamenovic and N. Wang, *Am. J. Physiol.: Cell Physiol.*, 2000, **2115**, 188–194.

52 C. Liu, H. Lin, M. Tang and Y. Wang, *Oncotarget*, 2015, **6**, 15966–15983.

53 K. Vuoriluoto, H. Haugen, S. Kiviluoto, J. Mpindi, J. Nevo, C. Gjerdrum, C. Tiron, J. B. Lorens and J. Ivaska, *Oncogene*, 2010, **30**, 1436–1448.

54 H. Yamaguchi and J. Condeelis, *Biochim. Biophys. Acta, Mol. Cell Res.*, 2007, **1773**, 642–652.

55 M. Olson and E. Sahai, *Clin. Exp. Metastasis*, 2009, **26**, 273–287.

56 C. Guo, S. Liu, J. Wang, M. Z. Sun and F. T. Greenaway, *Clin. Chim. Acta*, 2013, **417**, 39–44.

57 T. Dechat, K. Pfleghaar, K. Sengupta, T. Shimi, D. K. Shumaker, L. Solimando and R. D. Goldman, *Genes Dev.*, 2008, **22**, 832–853.

58 J. Lammerding, P. C. Schulze, T. Takahashi, S. Kozlov, T. Sullivan, R. D. Kamm, C. L. Stewart and R. T. Lee, *J. Clin. Invest.*, 2004, **113**, 370–378.

59 L. A. Lautscham, C. Kammerer, J. R. Lange, T. Kolb, C. Mark, A. Schilling, P. L. Strissel, R. Strick, C. Gluth, A. C. Rowat, C. Metzner and B. Fabry, *Biophys. J.*, 2015, **109**, 900–913.

60 D. B. Agus, J. F. Alexander, W. Arap, S. Ashili, J. E. Aslan, R. H. Austin, V. Backman, K. J. Bethel, R. Bonneau, W.-C. Chen, C. Chen-Tanyolac, N. C. Choi, S. A. Curley, M. Dallas, D. Damania, P. C. W. Davies, P. Decuzzi, L. Dickinson, L. Estevez-Salmeron, V. Estrella, M. Ferrari, C. Fischbach, J. Foo, S. I. Fraley, C. Frantz, A. Fuhrmann, P. Gascard, R. A. Gatenby, Y. Geng, S. Gerecht, R. J. Gillies, B. Godin, W. M. Grady, A. Greenfield, C. Hemphill, B. L. Hempstead, A. Hielscher, W. D. Hillis, E. C. Holland, A. Ibrahim-Hashim, T. Jacks, R. H. Johnson, A. Joo, J. E. Katz, L. Kelbauskas, C. Kesselman, M. R. King, K. Konstantopoulos, C. M. Kraning-Rush, P. Kuhn, K. Kung, B. Kwee, J. N. Lakins, G. Lambert, D. Liao, J. D. Licht, J. T. Liphardt, L. Liu, M. C. Lloyd, A. Lyubimova, P. Mallick, J. Marko, O. J. T. McCarty, D. R. Meldrum, F. Michor, S. M. Mumenthaler, V. Nandakumar, T. V. O'Halloran, S. Oh, R. Pasqualini, M. J. Paszek, K. G. Philips, C. S. Poultney, K. Rana, C. A. Reinhart-King, R. Ros, G. L. Semenza, P. Senechal, M. L. Shuler, S. Srinivasan, J. R. Staunton, Y. Stypula, H. Subramanian, T. D. Tlsty, G. W. Tormoen, Y. Tseng, A. van Oudenaarden, S. S. Verbridge, J. C. Wan, V. M. Weaver, J. Widom, C. Will, D. Wirtz, J. Wojtkowiak and P.-H. Wu, *Sci. Rep.*, 2013, **3**, 1449.

61 M. J. Paszek, N. Zahir, K. R. Johnson, J. N. Lakins, G. I. Rozenberg, A. Gefen, C. A. Reinhart-king, S. S. Margulies, M. Dembo, D. Boettiger, D. A. Hammer and V. M. Weaver, *Cancer Cell*, 2005, **8**, 241–254.

62 D. Stamenovic and M. F. Coughlin, *J. Theor. Biol.*, 1999, **201**, 63–74.

63 D. R. Gossett, H. T. K. Tse, S. A. Lee, Y. Ying, A. G. Lindgren, O. O. Yang, J. Rao, A. T. Clark and D. Di Carlo, *Proc. Natl. Acad. Sci. U. S. A.*, 2012, **109**, 7630–7635.

64 A. Maniotis, C. S. Chen and D. Ingber, *Proc. Natl. Acad. Sci. U. S. A.*, 2000, **94**, 849–854.

65 C. Y. Park, D. Tambe, A. M. Alencar, X. Trepat, E. H. Zhou, E. Millet, J. P. Butler and J. J. Fredberg, *Am. J. Physiol.: Cell Physiol.*, 2010, **298**, 1245–1252.

66 S. Kumar, I. Z. Maxwell, A. Heisterkamp, T. R. Polte, T. P. Lele, M. Salanga, E. Mazur and D. E. Ingber, *Biophys. J.*, 2006, **90**, 3762–3773.

67 S. Hu, J. Chen, J. P. Butler and N. Wang, *Biochem. Biophys. Res. Commun.*, 2005, **329**, 423–428.

68 A. Mazumder and G. V. Shivashankar, *J. R. Soc., Interface*, 2010, **7**, S321–S330.

69 H. Lee, W. J. Adams, P. W. Alford, M. L. Mccain, A. W. Feinberg, S. P. Sheehy, J. A. Goss and K. K. Parker, *Exp. Biol. Med.*, 2015, **240**, 1543–1554.

70 J. L. V. Broers, E. A. G. Peeters, H. J. H. Kuijpers, J. Endert, C. V. C. Bouten, C. W. J. Oomens, F. P. T. Baaijens and F. C. S. Ramaekers, *Hum. Mol. Genet.*, 2004, **13**, 2567–2580.

71 C. M. Denais, R. M. Gilbert, P. Isermann, A. L. Mcgregor, M. Lindert, B. Weigelin, P. M. Davidson, P. Friedl, K. Wolf and J. Lammerding, *Science*, 2016, **352**, 353–358.

72 M. Raab, M. Gentili, H. De Belly, H. Thiam, P. Vargas, A. J. Jimenez, F. Lautenschlaeger, R. Voituriez, N. Manel and M. Piel, *Science*, 2016, **352**, 359–362.

73 O.-Y. Revach, A. Weiner, K. Rechav, I. Sabanay, A. Livne and B. Geiger, *Sci. Rep.*, 2015, **5**, 9466.

74 S. B. Khatau, R. J. Bloom, S. Bajpai, D. Razafsky, S. Zang, A. Giri, D. Hodzic and D. Wirtz, *Sci. Rep.*, 2012, **488**, 1–11.

75 J. I. De las Heras, D. G. Batrakou and E. C. Schirmer, *Semin. Cancer Biol.*, 2013, **23**, 125–137.

76 L. Kong, G. Schäfer, H. Bu, Y. Zhang, Y. Zhang and H. Klocker, *Carcinogenesis*, 2012, **33**, 751–759.

77 M. Prokocimer, M. Davidovich, M. Nissim-Rafinia, N. Wiesel-Motiuk, D. Z. Bar, R. Barkan, E. Meshorer and Y. Gruenbaum, *J. Cell. Mol. Med.*, 2009, **13**, 1059–1085.

78 S. Zhao, Y. Wang, L. Cao, M. M. Ouellette and J. W. Freeman, *Int. J. Cancer*, 2010, **127**, 2076–2087.

79 Y.-W. Chen, P.-J. Hsiao, C.-C. Weng, K.-K. Kuo, T.-L. Kuo, D.-C. Wu, W.-C. Hung and K.-H. Cheng, *BMC Cancer*, 2014, **14**, 181.

80 M. Amano, M. Nakayama and K. Kaibuchi, *Cytoskeleton*, 2010, **67**, 545–554.

81 S. Sharma, C. Santiskulvong, J. Rao, J. K. Gimzewski and O. Dorigo, *Integr. Biol.*, 2014, **6**, 611–617.

82 I. Aifuwa, A. Giri, N. Longe, S. H. Lee, S. S. An and D. Wirtz, *Oncotarget*, 2015, **6**, 30516–30531.

83 S. Yachida, S. Jones, I. Bozic, T. Antal, R. Leary, B. Fu, M. Kamiyama, R. H. Hruban, J. R. Eshleman, M. A. Nowak, V. E. Velculescu, K. W. Kinzler, B. Vogelstein and C. A. Iacobuzio-Donahue, *Nature*, 2010, **467**, 1114–1117.

84 C. A. Sartorius, C. T. Hanna, B. Gril, H. Cruz, N. J. Serkova, K. M. Huber, P. Kabos, T. B. Schedin, V. F. Borges, P. S. Steeg and D. M. Cittelly, *Oncogene*, 2015, **35**, 2881–2892.

85 D. C. Duffy, J. C. McDonald, O. J. A. Schueller and G. M. Whitesides, *Anal. Chem.*, 1998, **70**, 4974–4984.

86 D. J. Hoelzle, B. A. Varghese, C. K. Chan and A. C. Rowat, *J. Visualized Exp.*, 2014, **91**, e51474.

87 I. N. Sneddon, *Int.J. Eng. Sci.*, 1965, **3**, 47–57.

88 V. M. Laurent, S. Kasas, A. Yersin, T. E. Schäffer, S. Catsicas, G. Dietler, A. B. Verkhovsky and J.-J. Meister, *Biophys. J.*, 2005, **89**, 667–675.

89 A. Dobin, C. A. Davis, F. Schlesinger, J. Drenkow, C. Zaleski, S. Jha, P. Batut, M. Chaisson and T. R. Gingeras, *Bioinformatics*, 2013, **29**, 15–21.

90 C. Trapnell, B. A. Williams, G. Pertea, A. Mortazavi, G. Kwan, M. J. van Baren, S. L. Salzberg, B. J. Wold and L. Pachter, *Nat. Biotechnol.*, 2010, **28**, 511–515.

Supplemental Figure 1

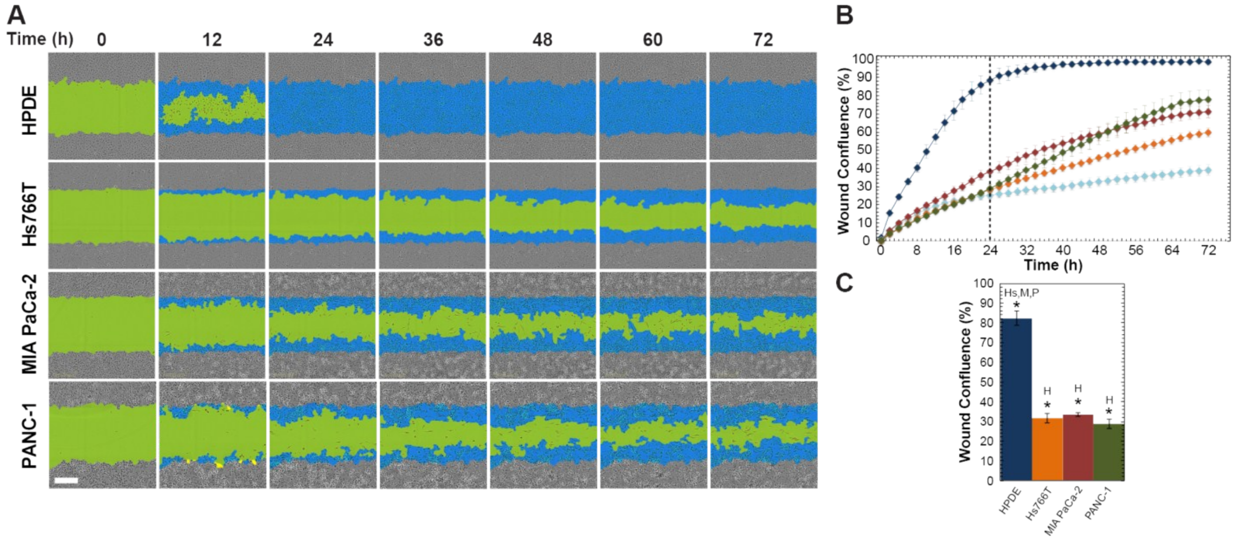

Migration behavior of pancreatic ductal cell lines. A. Time series of images showing scratch wound migration of pancreatic ductal cells without Matrigel. Wound confluence is the percentage of wound area covered by cells. Color legend: green is the wound area, grey represents the confluent cells outside of the wound area, and blue shows wound confluence in the wound area. Scale, 300 μm. **B.** Quantification of migration across three independent experiments. Dotted line indicates the 24-hour time point, which we use compare wound confluence values for statistical significance. **C.** Bar plot of migration data after 24 hours. Error bars represent standard error. P-values determined by student's T-test. *p < 0.05. The significance of pairwise comparisons between cell lines is shown in panel C by the initial(s) of the cell lines that are significantly different where H: HPDE, Hs: Hs766T, M: MIA PaCa-2, and P: PANC-1. For example, HPDE is significantly different (*p < 0.05) from Hs766T (Hs), MIA PaCa-2 (M), and PANC-1 (P).

Supplemental Figure 2

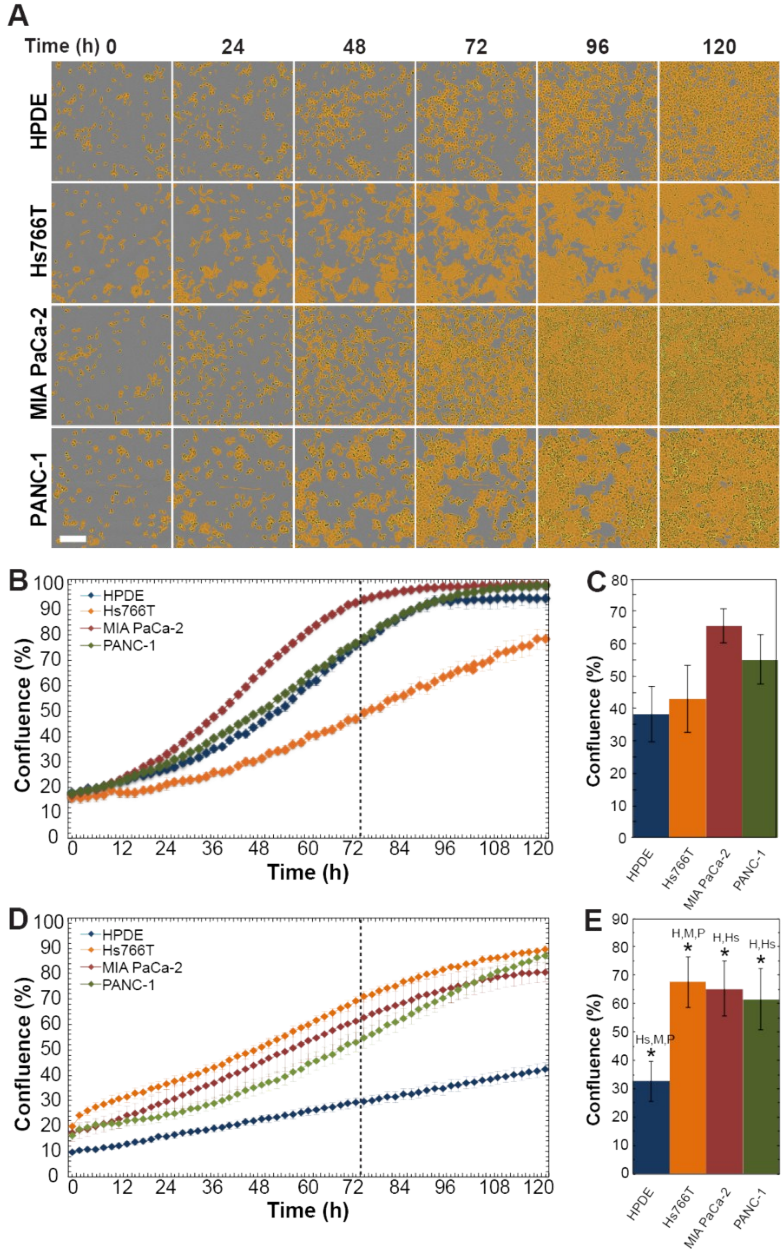

Proliferation of pancreatic ductal cell lines. A. Time series of images showing confluence of pancreatic ductal cells. Scale, 300 µm. **B.** Representative quantification from one experiment of percent confluence, which denotes the percentage area coverage of cells plated on a thin layer of Matrigel. Dotted line indicates the 72-hour time point, which we use compare confluence values for statistical significance. **C.** Bar plot of confluence data after 72 hours averaged across three individual experiments. Error bars represent standard error. P-values determined by student's T-test. None of the pairwise comparisons between pancreatic ductal cell lines are significant ($p > 0.05$). **D.** Representative quantification from one experiment of percent confluence of cells plated on a thin layer of Matrigel and overlaid with a thick layer of Matrigel. Dotted line indicates the 72-hour time point, which we use compare confluence values for statistical significance. **E.** Bar plot of confluence data after 72 hours averaged across three individual experiments. The significance of pairwise comparisons between cell lines is shown in panel E by the initial(s) of the cell lines that are significantly different where H: HPDE, Hs: Hs766T, M: MIA PaCa-2, and P: PANC-1. For example, HPDE is significantly different ($*p < 0.05$) from Hs766T (Hs), MIA PaCa-2 (M), and PANC-1 (P).

Supplemental Figure 3

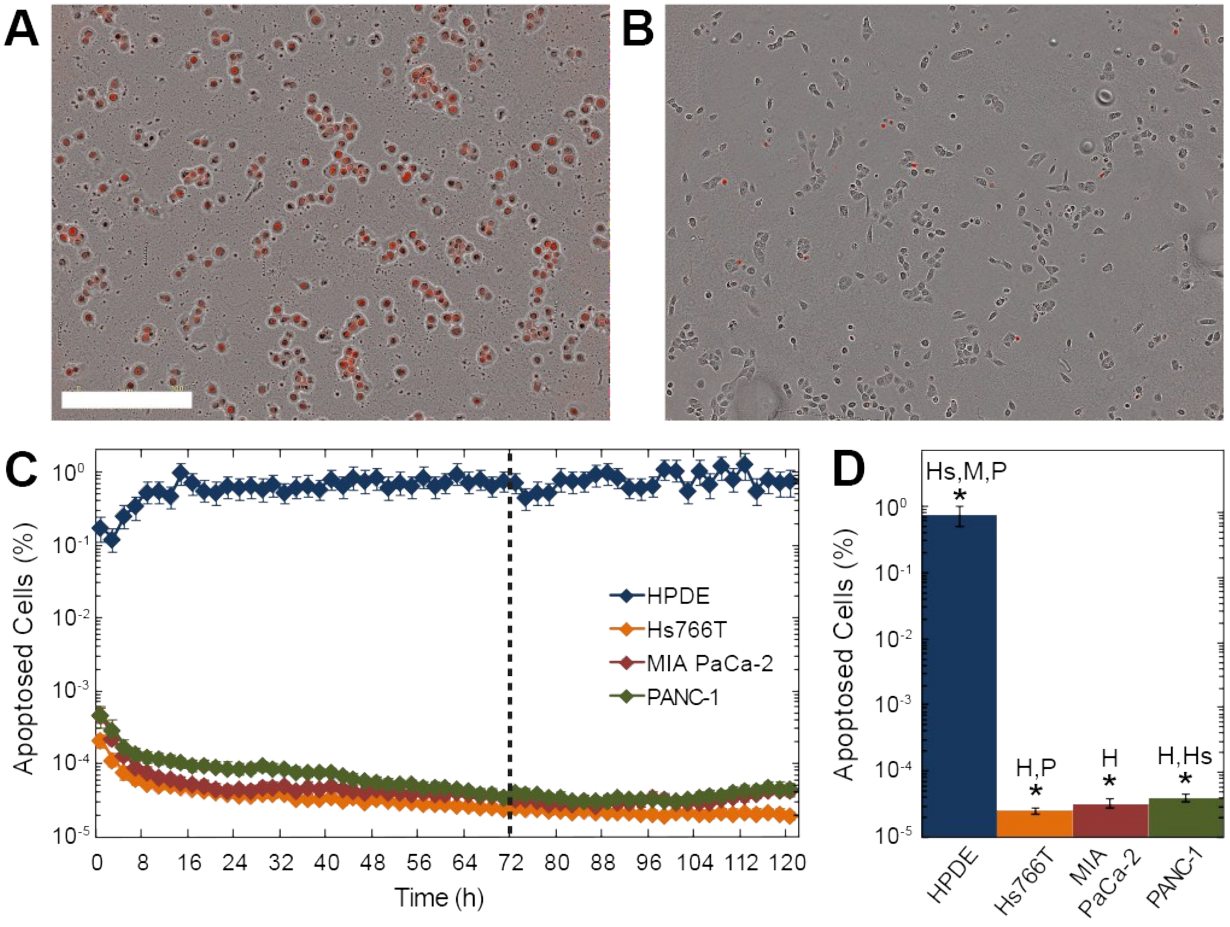

Apoptosis of pancreatic ductal cell lines with Matrigel overlay. Representative images of cells stained with DRAQ7 to quantify apoptosis: **A.** positive control (HPDE cells treated with DMEM, which is causes these cells to undergo apoptosis) and **B.** HPDE cells with a Matrigel overlay after 72 hours. Scale, 350 μm. **C.** Data of apoptosis across 4 pancreatic ductal cell lines over 3 independent experiments. Data points represent average % apoptosis over 3 independent experiments and error bars represent standard deviation. Dotted line indicates the 72-hour time point, which we use compare % apoptosis for statistical significance. **D.** Bar plot of apoptosis data after 72 hours averaged across three individual experiments. Error bars represent standard deviation. Statistical significance determined using a Student's t-test. $^*p < 0.05$. The significance of pairwise comparisons between cell lines is shown in panel C by the initial(s) of the cell lines that are significantly different where H: HPDE, Hs: Hs766T, M: MIA PaCa-2, and P: PANC-1. For example, HPDE is significantly different ($^*p < 0.05$) from Hs766T (Hs), MIA PaCa-2 (M), and PANC-1 (P).

Supplemental Figure 4

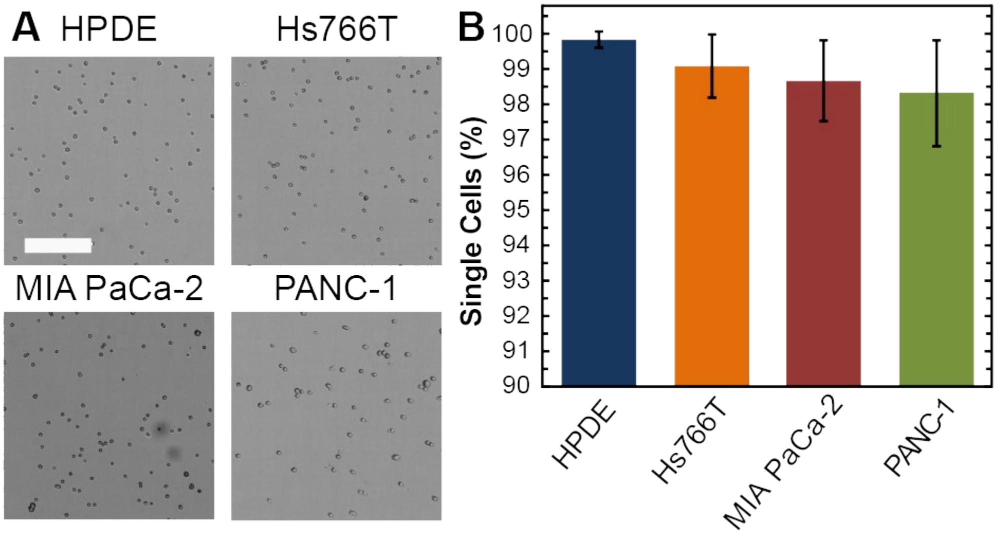

Cell suspensions for PMF assay contain over 98% single cells. A. Representative images of cell suspensions prior to PMF. Scale, 300 µm. B. Quantification of single cells determined by image analysis. Bar plot represents the average from 3 independent experiments. Error bars represent standard deviation. Statistical significance determined using a Student's t-test. No significance is observed ($p > 0.05$) for all pairwise comparisons between cell lines.

Supplemental Figure 5

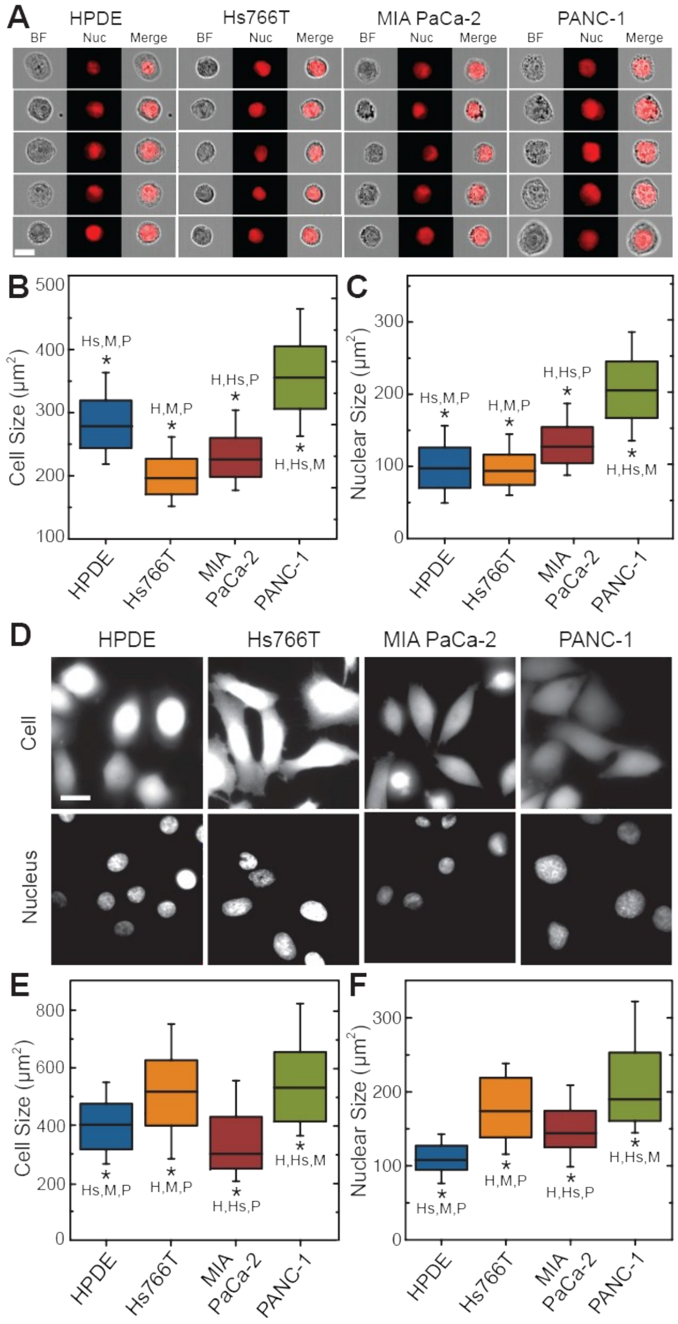

Cell and nuclear size of PDAC cells. A. Imaging flow cytometry of HPDE and PDAC cells that are fixed in a suspended state. Nuclei are labeled with DRAQ5. Scale, 15 µm. We use this data to quantify **B.** Cell size and **C.** Nuclear size. **D.** Images of adhered pancreatic ductal cells obtained by confocal microscopy. From this data, we measure **E.** Cell size and **F.** Nuclear size. Boxes represent the 25-75 percentile, whiskers represent the 10-90 percentile, and the horizontal line represents the median. P-values are calculated with a Mann-Whitney U test. *$p < 0.05$. All error bars represent standard errors. The significance of pairwise comparisons between cell lines is shown in panels B, C, E, and F by the initial(s) of the cell lines that are significantly different where H: HPDE, Hs: Hs766T, M: MIA PaCa-2, and P: PANC-1. For example, in panel B, HPDE is significantly different (*$p < 0.05$) from Hs766T (Hs), MIA PaCa-2 (M) and PANC-1 (P).

Supplemental Figure 6

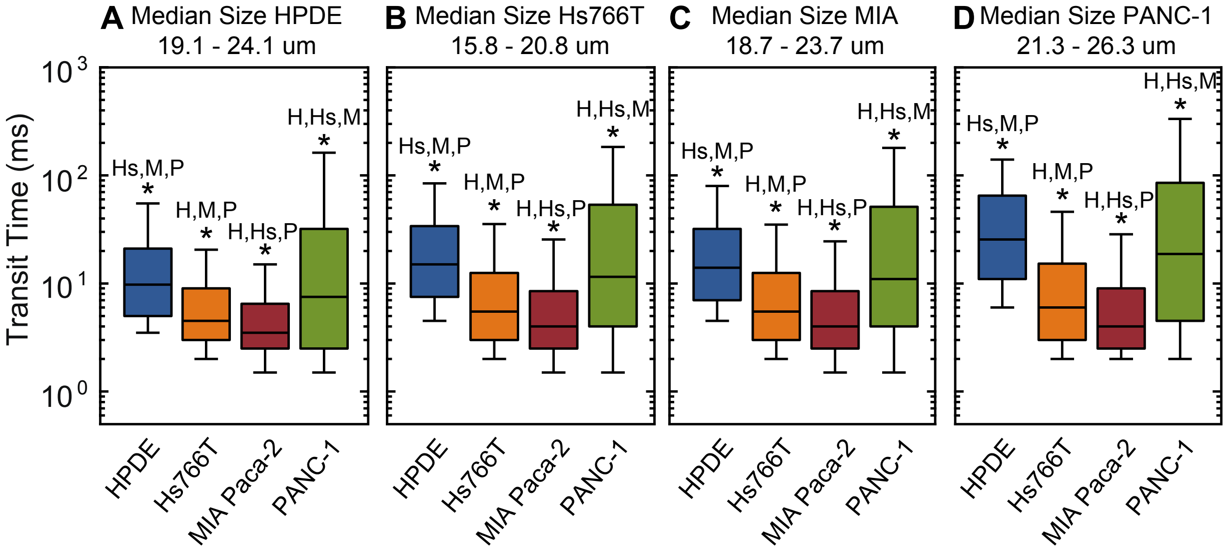

Microfluidics data gated for cell size. Each plot shows transit time data obtained by microfluidic deformability cytometry for pancreatic ductal cell lines within a 5 μm range of the median size of each cell line: **A.** HPDE, **B.** Hs766T, **C.** MIA PaCa-2, and **D.** PANC-1. Boxes represent the 25^{th} and 75^{th} percentiles, whiskers represent the 10^{th} and 90^{th} percentiles, and the horizontal line represents the median. n > 350 cells for each box. The significance of pairwise comparisons between cell lines is shown in panels B, C, E, and F by the initial(s) of the cell lines that are significantly different where H: HPDE, Hs: Hs766T, M: MIA PaCa-2, and P: PANC-1. For example, in panel A, HPDE is significantly different (*$p < 0.05$) from Hs766T (Hs), MIA PaCa-2 (M), and PANC-1 (P).

Supplemental Figure 7

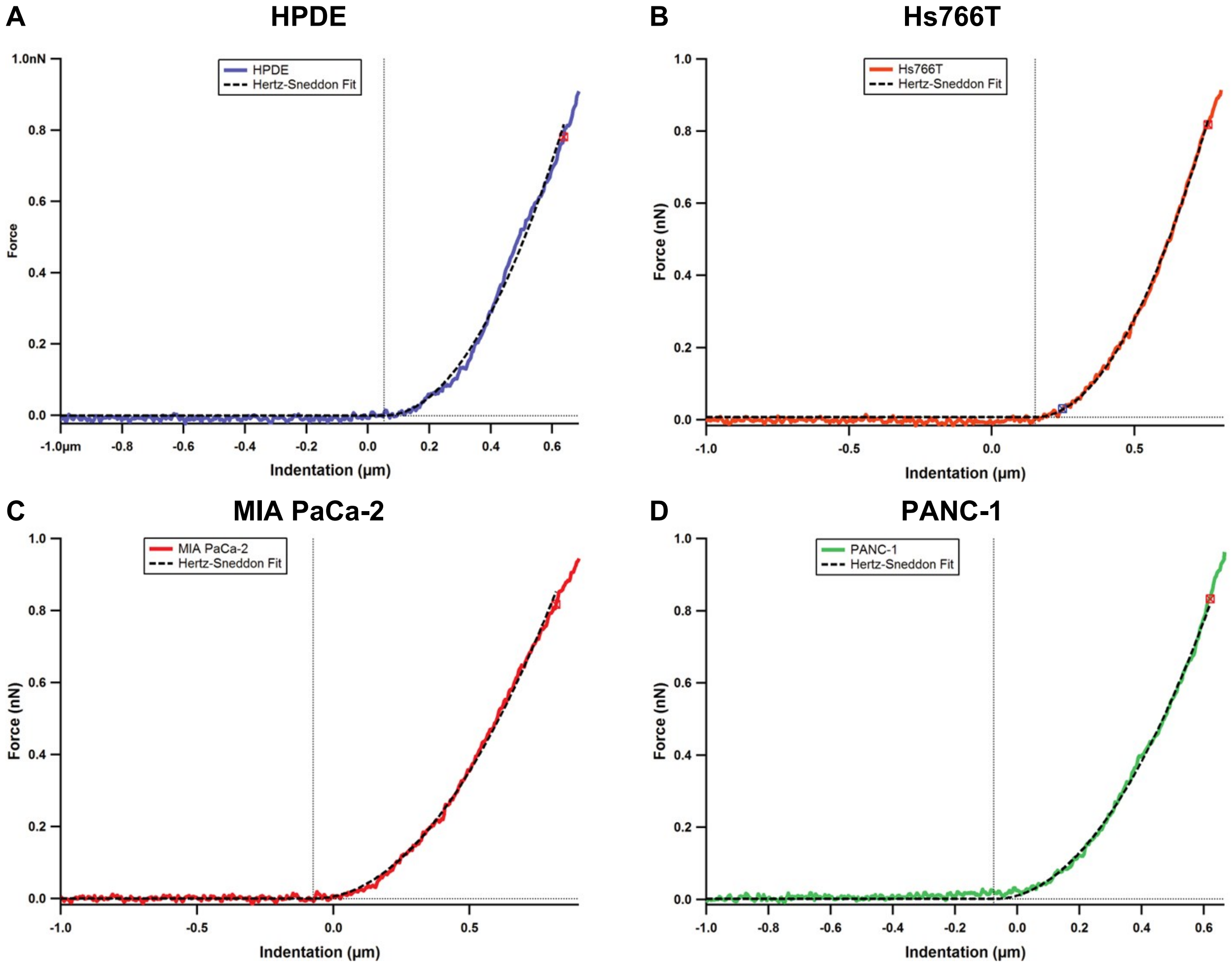

Hertz-Sneddon fits for AFM force curves. Each plot shows an example force curve obtained by atomic force microscopy (AFM) for pancreatic ductal cell lines: **A.** HPDE, **B.** Hs766T, **C.** MIA PaCa-2, and **D.** PANC-1. Hertz-Sneddon fits are indicated by black dashed lines.

Supplemental Figure 8

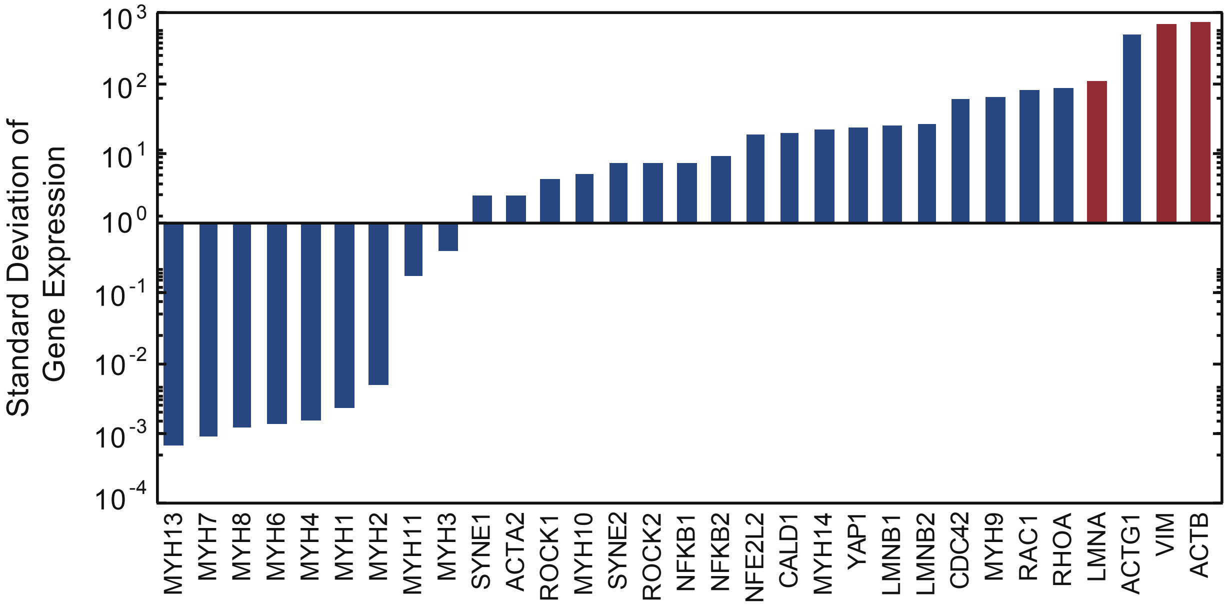

RNAseq analysis of mechanome proteins across cohort of 41 pancreatic cancer cell lines. Bar plot represents the standard deviation in gene expression levels of proteins that contribute to cell mechanotype.

Supplemental Table 1. Founder mutations in PDAC cell lines.

Adapted from Deer, E. L., González-Hernández, J., Coursen, J. D., Shea, J. E., Ngatia, J., Scaife, C. L., … Mulvihill, S. J. (2010). Phenotype and genotype of pancreatic cancer cell lines. *Pancreas*, *39*(4), 425–35.

Gene	**HPDE**	**HPAF**	**MIA PaCa-2**	**PANC-I**	**Hs766T**
KRAS	WT	Mut	Mut	Mut	Mut
TP53	WT	Mut	Mut	Mut	Mut
CDKN2A/p16	WT	Mut	Mut	Mut	Mut
SMAD4/DPC4	WT	WT	WT	WT	Mut

Supplemental Table 2. Pearson's values (top) and significance values (bottom) for correlation heat map as shown in Figure 5.

		Invasive Potential		Deformability			Structural Proteins				
	PEARSON'S CORRELATIONS	Invasion	Transwell Migration	Young's Modulus	Retention	Transit Time	Vimentin	F-actin	Beta-actin	Lamin A	Lamin C
Invasive Potential	Invasion	1	0.98711	0.97116	0.2098	-0.23968	0.62	-0.94657	0.99489	0.95849	0.55184
	Transwell Migration	0.98711	1	0.92047	0.0506	-0.39198	0.73759	-0.88274	0.99823	0.90049	0.41124
Deformability	Young's Modulus	0.97116	0.92047	1	0.43688	-0.00128	0.41505	-0.99616	0.94211	0.99883	0.73476
	Retention	0.2098	0.0506	0.43688	1	0.89896	-0.63706	-0.51392	0.10998	0.47987	0.93117
	Transit Time	-0.23968	-0.39198	-0.00128	0.89896	1	-0.91033	-0.08623	-0.33651	0.04709	0.67738
Structural Proteins	Vimentin	0.62	0.73759	0.41505	-0.63706	-0.91033	1	-0.33384	0.69608	0.37056	-0.31218
	F-actin	-0.94657	-0.88274	-0.99616	-0.51392	-0.08623	-0.33384	1	-0.90915	-0.99923	-0.7913
	Beta-actin	0.99489	0.99823	0.94211	0.10998	-0.33651	0.69608	-0.90915	1	0.92479	0.46479
	Lamin A	0.95849	0.90049	0.99883	0.47987	0.04709	0.37056	-0.99923	0.92479	1	0.76671
	Lamin C	0.55184	0.41124	0.73476	0.93117	0.67738	-0.31218	-0.7913	0.46479	0.76671	1

		Invasive Potential		Deformability			Structural Proteins				
	SIGNIFICANCE	Invasion	Transwell Migration	Young's Modulus	Retention	Transit Time	Vimentin	F-actin	Beta-actin	Lamin A	Lamin C
Invasive Potential	Invasion	--	0.10234	0.15327	0.86544	0.84591	0.57426	0.20905	0.06441	0.18407	0.62786
	Transwell Migration	0.10234	--	0.2556	0.96777	0.74358	0.47192	0.31139	0.03793	0.28641	0.73019
Deformability	Young's Modulus	0.15327	0.2556	--	0.71217	0.99918	0.72753	0.05578	0.21767	0.0308	0.47459
	Retention	0.86544	0.96777	0.71217	--	0.28865	0.5603	0.65639	0.92984	0.68137	0.23758
	Transit Time	0.84591	0.74358	0.99918	0.28865	--	0.27165	0.94503	0.78151	0.97001	0.52623
Structural Proteins	Vimentin	0.57426	0.47192	0.72753	0.5603	0.27165	--	0.78331	0.50986	0.75833	0.79788
	F-actin	0.20905	0.31139	0.05578	0.65639	0.94503	0.78331	--	0.27346	0.02498	0.4188
	Beta-actin	0.06441	0.03793	0.21767	0.92984	0.78151	0.50986	0.27346	--	0.24848	0.69226
	Lamin A	0.18407	0.28641	0.0308	0.68137	0.97001	0.75833	0.02498	0.24848	--	0.44378
	Lamin C	0.62786	0.73019	0.47459	0.23758	0.52623	0.79788	0.4188	0.69226	0.44378	--

Chapter III: Myosin II, Arp2/3, and formin activity contribute to cancer cell stiffness and invasion

Myosin II, Arp2/3, and formin activity contribute to cancer cell stiffness and invasion

Angelyn V. Nguyen[1], Brittany Trompetto[1], Marvin Tan[2], Kenneth Hsueh-heng Hu[3], Manish Butte[4,5], Eric Chiou[2,6], Amy C. Rowat[1,6,7]

Author Affiliations: [1]Department of Integrative Biology and Physiology, University of California, Los Angeles, [2]Department of Mechanical and Aerospace Engineering, University of California, Los Angeles, Los Angeles, [3]Stanford Biophysics, Stanford University, Stanford, CA 94305, USA, [4]Department of Pediatrics, University of California, Los Angeles, [5]Department of Microbiology, Immunology, and Molecular Genetics, University of California, Los Angeles, [6]Department of Bioengineering, University of California, Los Angeles, [7]Jonsson Comprehensive Cancer Center, University of California, Los Angeles

Abstract

Metastasis is a fundamentally physical process in which cells are required to deform through narrow gaps and generate forces to invade surrounding tissues. In many cancers, more invasive cells are more deformable than less invasive cells, but we previously found that more invasive pancreatic ductal adenocarcinoma (PDAC) cells are stiffer than less invasive PDAC cells. Here we investigate potential factors that contribute to the simultaneous increase in cell stiffness and invasion, including actomyosin contractility and actin polymerization. To measure the invasive potential of PDAC cells, we use a scratch wound invasion assay with Matrigel overlay. To measure the stiffness of PDAC cells, we perform atomic force microscopy (AFM). We use the pharmacological inhibitor blebbistatin to perturb actomyosin contractility, and CK-666 and SMIFH2 to inhibit actin polymerization through the Arp2/3 and formin pathways, respectively.

The results of this study show that both actomyosin contractility and actin polymerization contribute to the stiffness of pancreatic cancer cells but that the invasion potential of different PDAC cell lines is differentially affected by inhibitors to myosin II and actin polymerization, suggesting that different PDAC cell lines may require different mechanisms to invade.

Introduction

Cell physical phenotypes, including deformability, adhesion, and contractility, are critical in cell invasion (1–3). The physical phenotypes of tumor cells may also be implicated in metastasis; to spread to distant sites, cells invade into the extracellular matrix, intravasate, and extravasate, which all require movement through micron-scale pores smaller than the size of their own diameter (3, 4). Cancer cell phenotypes such as deformability and adhesion are emerging as label-free, complementary biomarkers for cancer diagnosis (5). Since the proteins and pathways that regulate cell physical phenotypes also contribute to cell invasion (1–3), mechanotransduction (6–10), and chemoresistance (11, 12), understanding the molecular origins of physical phenotypes can provide mechanistic insight into cancer progression and new therapeutic strategies. For example, the contractility of cells is reduced with treatment of the Rho-associated protein kinase (ROCK) inhibitor fasudil (13); this drug also decreases the physical tension within the tumor, leading to increased drug sensitivity, as well as reduced cancer cell invasion *in vitro* and metastasis *in vivo* (12). With a deeper knowledge of the relationship between cell physical phenotypes and clinically relevant metrics, such as invasion, we could identify additional therapeutic strategies to improve patient outcomes.

The mechanical phenotype, or mechanotype, of cancer cells shows strong associations with *in vitro* measurements of cell invasion (2, 14–20), which reflect the ability of cells to metastasize *in vivo* (21). Mechanotype is a physical property of cells that describes the extent to which a cell deforms in response to mechanical stresses. A frequently observed trend is that more invasive tumor cells are more deformable; this has been shown across prostate, ovarian, and breast cancer cell lines *in vitro* (2, 14–16), as well as the tumor cells of human breast biopsies *in situ* (22, 23). Since increased deformability enables cells to more readily deform through narrow gaps (24, 25), a more compliant mechanotype could provide a selective advantage in metastasis. Conversely, cells with increased cellular and nuclear stiffness are more likely to occlude narrow gaps (24, 25) and exhibit reduced cell invasion (2, 26–28). However, there are examples where more invasive cells are stiffer, including lung cancer cells (18), pancreatic ductal adenocarcinoma cells (19), fibroblasts with genetic alterations that result in oncogenic transformation (17), and cancer cells with increased beta-adrenergic signaling (20). While decreased cellular and nuclear deformability can explain why stiffer cells exhibit increased occlusion of pores and reduced invasion, it remains poorly understood what factors contribute to the simultaneous increase in cell stiffness and invasion. With a greater understanding of why stiffer cells are more invasive, we can advance mechanotype as a clinical biomarker and gain insights into novel therapeutic targets.

Cells are complex, dynamic materials whose mechanotype is determined by both intrinsic and extrinsic factors. Intrinsic determinants of cell mechanotype include levels and subcellular organization of cytoskeletal proteins, such as actin and microtubules. Cell mechanotype is also determined by the forces that cells generate in response to extrinsic factors, such as soluble molecules and the physical properties of the microenvironment. The intrinsic and extrinsic factors that determine cell physical properties also mediate cell invasion (29–32). For example, actin is a key structural protein that is also crucial in dynamic cellular behaviors, such as the generation of force through the conversion of ATP into mechanical energy. Both the structural organization of actin and its contribution to the generation of contractile and protrusive forces influence cell stiffness (26, 33–35). In addition to its contribution to mechanotype, the generation of contractile and protrusive forces that result for actin dynamics increases cell invasion (36, 37). For example, reducing contractile actomyosin activity by pharmacologic inhibition of myosin II results in decreased cell migration and invasion (38, 39), as well as decreased stiffness of fibroblasts and ovarian cancer cells (26, 35). The protrusive forces generated by actin nucleation and polymerization, which are mediated by the Arp2/3 complex and formins such as diaphanous proteins, are also critical for certain modes of cancer cell motility and invasion: reducing the activity of Arp2/3 and formins diminishes the formation of lamellipodia and invadopodia (36, 40, 41), and decrease the invasion of head and neck squamous cancer cells (42). The activity of Arp2/3 and formins also contribute to cancer cell stiffness (43). We previously investigated whether levels of beta-actin and filamentous actin contribute to the increased stiffness of more invasive PDAC cells (19). However, we found no significant differences in the levels of actin across cell lines with varying stiffness and invasive potential, suggesting that the levels of actin cannot fully explain the contribution of this protein to cancer cell behaviors.

Here we test the hypothesis that more invasive cancer cells are stiffer due to active force generation that is mediated by myosin II, Arp2/3, and formins. We use a panel of PDAC cell lines as a model system, as they have well-defined mechanotype and invasive potential (19); this allows us to investigate factors that contribute to stiffer cells being more invasive across cell lines with similar genetic background and tissue origin (44). We measure cell stiffness using atomic force microscopy (AFM) and invasion using a 3D scratch-wound assay. We determine contributions of myosin II, Arp2/3, and formin activity to cell stiffness and invasion using pharmacologic inhibitors. While there is a strong, positive correlation between stiffness and invasion of the untreated PDAC cell lines, we find that the relationship between stiffness and invasion is weaker when the activity of myosin II, Arp2/3, and formins is pharmacologically inhibited. In addition, we find that the activity of myosin II, Arp2/3, and formins have different levels of contribution to invasion across our cell panel, indicating that different PDAC cell lines, despite similar tissue origins, may rely on different mechanisms for invasion. Our results highlight how a deeper understanding of the pathways that regulate cell mechanotype and invasion could provide valuable information for the use of physical phenotypes as biomarkers and the development multi-target therapeutics for improved clinical benefit.

Results

To investigate the relationship between cell stiffness, actomyosin contractility or protrusive forces, and invasion, we use three immortalized PDAC cell lines: Hs766T, MIA PaCa-2, and PANC-1. The MIA PaCa-2 and PANC-1 cell lines have similar founder mutations (*Kras*, *TP53*, and *CDKN2A*), while the Hs766T cell line has an additional *SMAD4* mutation (44). We previously determined that across our panel of PDAC cell lines, more invasive cells tend to be stiffer (19). The Hs766T cells are the stiffest and most invasive of these three cell lines, while the MIA PaCa-2 are the most deformable and least invasive (19).

Myosin II activity is critical for the invasion of MIA PaCa-2 and PANC-1 cells but not Hs766T cells. Myosin II is essential to both the generation of forces involved in motility (45) and cell stiffness (26, 46). Therefore, we first investigated the role of myosin II in the increased stiffness of more invasive PDAC cells. To test our hypothesis, we first determine the effect of myosin II activity on PDAC cell invasion using a 3D scratch-wound assay overlaid with a Matrigel protein matrix. To reduce the activity of myosin II, we treat cells with blebbistatin, a small molecule inhibitor that binds to the myosin-ADP-P_i complex, which is the actin-detached state of myosin (47). When we treat our panel with the DMSO vehicle control, we observe that invasion varies across PDAC cell lines, with the order from most to least invasive being Hs766T > PANC1 > MiAPaCa-2 (Fig. 3-1); these results are consistent with our previous findings (19). Interestingly, we find that blebbistatin has cell line-dependent effects on PDAC invasion (Fig. 3-1). Both PANC-1 and MIA PaCa-2 show significant, dose-dependent decreases in invasion with increasing concentrations of blebbistatin. For example, at 72 hours, MIA PaCa-2 cells show an 8% reduction in invasion from 19% ± 2% to 11% ± 1% with a 50 µM blebbistatin treatment ($P = 2.1 \times 10^{-4}$). Similarly, the PANC-1 cells show a 15% reduction from 30% ± 1% to 13% ± 2% ($P = 5.9 \times 10^{-10}$). Our results showing reduced invasion potential for the MIA PaCa-2 and PANC-1 cells with blebbistatin treatment are consistent with other studies that observe reduced invasion with decreased actomyosin activity (39, 48), as well as studies that inhibit targets from other pathways involved in actomyosin contractility (49–51). By contrast, Hs766T cells show no significant change in invasion with 50 µM blebbistatin treatment when compared to the vehicle control at 72 hours (50% ± 2% versus 52% ± 3%, $p = 6.1 \times 10^{-1}$). Since changes in proliferation rates between cells and treatment conditions can impact invasion results, we also measure cell proliferation by tracking confluence over time. We find that treatment with 50 µM blebbistatin decreases the confluence of MIA PaCa-2 cells by 41% after 72 hours. Although the observed decrease in MIA PaCa-2 proliferation may contribute to the reduced invasion that we observe in the scratch-wound assay, the proliferation of PANC-1 cells is not altered despite the decreased invasion (Supp. Fig. 3-1). In addition, the Hs766T cells exhibit no significant changes in invasion but show a decrease in proliferation with 50 µM blebbistatin treatment, suggesting that the unaltered invasion of Hs766T cells cannot be simply explained by the insensitivity of these cells to blebbistatin treatment. Taken together, the differences we observe in PDAC cell proliferation cannot explain the differences observed in invasion when our cell panel is treated with the myosin II inhibitor blebbistatin (Supp. Fig. 3-1, $R^2 = 0.04$). Therefore, our data suggest that while myosin II activity is required for the invasion of the MIA PaCa-2 and PANC-1 cells, other factors govern the invasion of Hs766T cells.

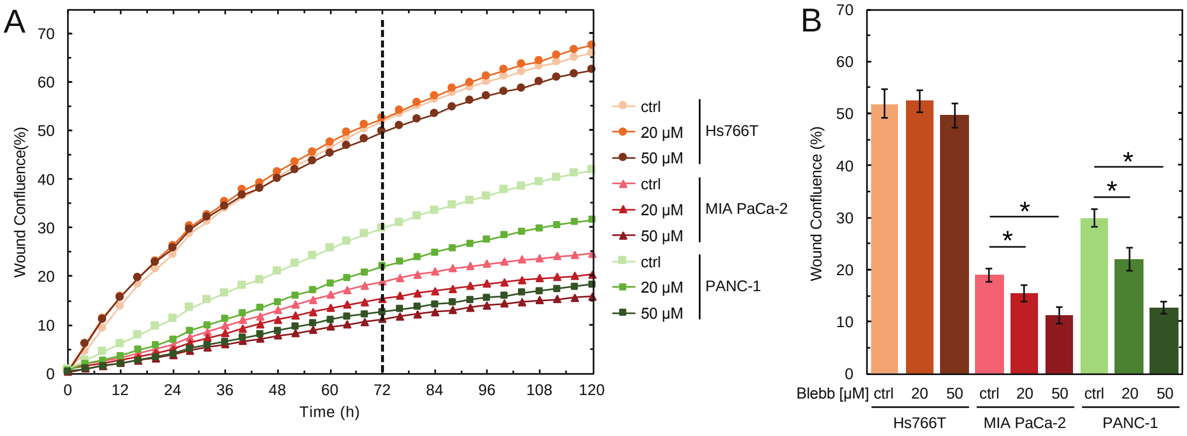

Figure 3-1. Myosin II activity is required for the invasion of MIA PaCa-2 and PANC-1 cells, but not Hs766T cells. (A) Invasion through Matrigel is measured by wound confluence in 3D scratch wound invasion assays. Scatter plot shows the quantification of wound confluence over time. The dashed line indicates the 72 h time point, which we use to compare wound confluence values for statistical significance. Cells are treated with blebbistatin or DMSO (ctrl) from t = 0. (B) Bar plot shows average wound confluence at the 72 h time point. Error bars represent standard error from 3 independent experiments. Pairwise p-values are determined by a student’s t-test. *$p < 0.05$.

The inhibition of myosin II slows the rate of PDAC cell rounding. To further evaluate the contributions of myosin II to the ability of cells to generate forces, we perform a cell rounding assay by detaching cells from their substrate with trypsin and measuring the rate of cell rounding (Fig. 3-2). Cells with higher levels of myosin II activity will have a faster rounding time compared to cells with reduced myosin II activity (52). After our invasion experiments without drug treatments (19), we anticipated that the Hs766T cells would have a fastest rounding time since they invade more quickly than the other two cell lines. However, the null effects of blebbistatin on the invasion of Hs766T cells (Fig. 3-1) led us to hypothesize that the MIA PaCa-2 and PANC-1 cells may be more dependent on myosin II activity, and may thus round faster with the addition of trypsin. We find that MIA PaCa-2 cells have the slowest cell rounding rate, as indicated by the highest rounding time constant of 119 s; this is consistent with the Mia PaCa-2 cells being the least invasive cells. By contrast, the Hs766T and PANC-1 cells round more quickly, as indicated by the shorter rounding time constants of 73 s and 45 s (Fig. 3-2B). With blebbistatin treatment, the cell rounding rate is reduced most significantly for the MIA PaCa-2 and PANC-1 cells: the MIA PaCa-2 have a 909% increase in rounding time constants, while the PANC-1 show a larger 1670% increase. Interestingly, the Hs766T cells show a much smaller 241% increase in the rounding time constant with blebbistatin treatment. The reduced effects of blebbistatin on the rounding rate of the Hs766T cells compared to the MIA PaCa-2 and PANC-1 cells corroborates out invasion results with blebbistatin treatment, further substantiating that both invasion and cell rounding of MIA PaCa-2 and PANC-1 cells are more dependent on myosin II activity than the Hs766T cells. These findings further underscore the differential effects of myosin II inhibition across different cell lines.

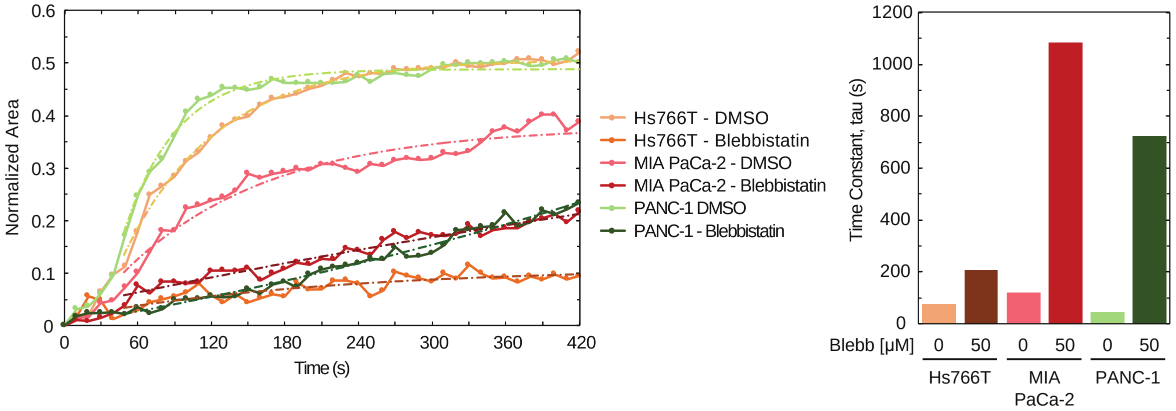

Figure 3-2. Contributions of myosin II to cell rounding rate vary across cell lines. A. Representative images show time sequence of cell shape change following trypsin treatment. Scale, 10 μm. B. Quantification of cell area as a function of time for cells treated with DMSO (ctrl) and 50 μM blebbistatin. Curves are fit using an exponential function. C. Time constants are extracted from fitting an exponential function to area data, as shown in panel B. Cells are treated with 50 μM blebbistatin for 30 min. Data shows averages and error bars represent at least 21 cells across 3 independent experiments.

PANC-1 cells exert increased traction stresses compared to Hs766T cells. The ability of cells to generate forces and pull on the surrounding extracellular matrix is critical during invasion, a process that is dependent on the activity of myosin II (53). To corroborate our cell rounding results, we next quantify the traction stresses that cells exert on their substrate using a micropillar assay, which also requires myosin II-dependent force generation. In our micropillar assay, cells are plated on polydimethylsiloxane (PDMS) micropillars that have a well-characterized elastic modulus and an average force per square area exerted by cells is extracted by measuring the resultant pillar displacements (Fig. 3-3A). Here we focus on Hs766T and PANC-1 cells, which are not only both stiffer and more invasive than the MIA PaCa-2 cells but also the two cell lines that are most differentially affected by blebbistatin treatment in our cell rounding assay. Since the PANC-1 cells round the most quickly in our myosin II-dependent cell rounding assay, we hypothesize that PANC-1 cells will exert higher traction stresses than the Hs766T cells because traction stresses are also dependent on myosin II activity (54, 55). Our results show that the average traction stress exerted by the PANC-1 cells is 44 ± 7 nN/µm^2 while the Hs766T cells have a 38% lower average traction stress of 27 ± 7 nN/µm^2 ($p = 2.0 \times 10^{-2}$) (Fig. 3-3B, 3-3C). These findings are consistent with the cell rounding data, which reveal that the PANC-1 cells round more quickly than the Hs766T cells. To determine the contributions of myosin II to the forces measured in our micropillar assay, we next measure traction stresses following blebbistatin treatment. For the PANC-1 cells, we find that the average traction stress significantly decreases by 30% ($p = 2.7 \times 10^{-1}$) (Fig. 3-3B, 3-3C); these results are consistent with previous studies showing that myosin II activity is a major contributor to cellular traction stresses (54, 55). By contrast, the average traction stress exerted by the Hs766T cells do not show any significant change with pharmacologic inhibition of myosin II (26 ± 7 nN/µm^2 for the vehicle control cells vs. 28 ± 7 nN/µm^2 for the blebbistatin-treated cells, $p = 2.7 \times 10^{-1}$) (Fig. 3-3B, 3-3C). Our findings reveal the differential contributions of myosin II activity to the traction stresses generated by the PANC-1 and Hs766T cells, and further suggest that Hs766T cells may be using a myosin-II-independent strategy to invade.

Myosin II activity contributes to PDAC cell stiffness. We next determine the extent to which myosin II activity contributes to the stiffness of the most invasive PDAC cells of our panel, Hs766T and PANC-1. Using atomic force microscopy (AFM), we measure the elastic modulus, *E*, of PDAC cells with and without the myosin II inhibitor blebbistatin (Fig. 3-4A). We find that pharmacological inhibition of myosin II activity significantly reduces the stiffness (*E)* of Hs766T and PANC-1 cells: Hs766T cell stiffness decreases 3.1-fold from 3.5 kPa to 1.1 kPa ($p = 3.0 \times$

10^{-6}), while PANC-1 cell stiffness decreases 2.9-fold from 2.0 kPa to 0.7 kPa ($p = 2.5 \times 10^{-4}$). Our results are consistent with other reports that blebbistatin makes adherent cells more deformable (26). Interestingly, while we found myosin II had no significant effect on the invasion or traction stresses of Hs766T cells, we do find a significant decrease in cell stiffness, which suggests that cell stiffness is not always coupled to invasive potential. Since myosin II contributes to both the generation of contractile (56, 57) and the crosslinking of actin (58), inhibition of myosin II could decrease cell stiffness by decreasing the crosslinking density of the actomyosin network in Hs766T cells, and thereby show more subtle effects on invasion.

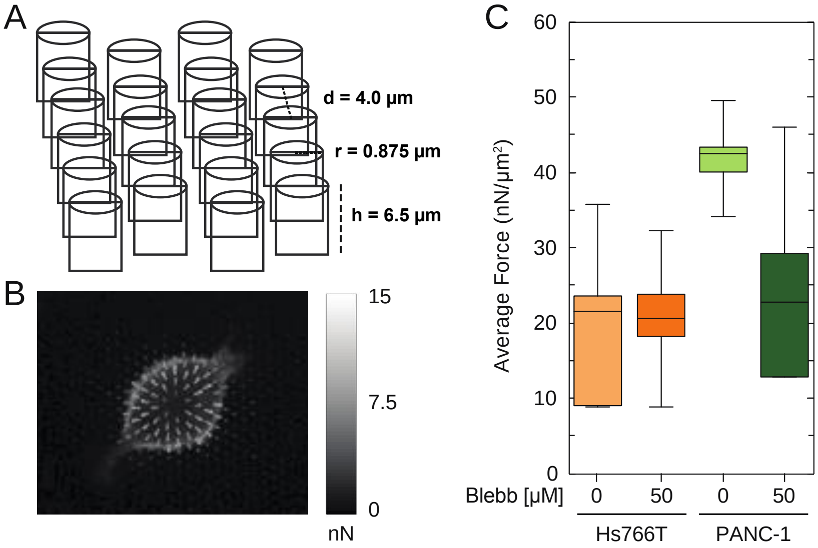

Figure 3-3. PANC-1 cells exert increased traction stresses compared to Hs766T cells. (A) Schematic illustration of the micropillar assay with device dimensions. d = distance between pillars, r = radius of pillar, h = height of pillar. (B) Representative force map. (C) Box plots quantifying the traction stresses exerted by Hs766T and PANC-1 cells, with and without blebbistatin treatment. Boxes represent the 25th and 75th percentiles, whiskers represent the 10th and 90th percentiles, and the horizontal line represents the median. Average force per pillar is determined by analysis of the displacement of each gold-coated micropillar 18 hours after plating of cells. Cells are treated with 50 μM blebbistatin for 30 min immediately before fixation. P-values are determined by a student's t-test. $^*p < 0.05$. We measure the traction stresses of at least 18 cells across 3 independent experiments.

To evaluate the relationship between cell stiffness and invasion in more detail, we perform linear regression to generate R^2-values across our PDAC cell lines with blebbistatin treatment and the DMSO vehicle control. While we previously found a strong correlation between the stiffness and invasion of untreated PDAC cell lines ($R^2 = 1.00$) (19), we find only a weak correlation between cell stiffness and invasion when cells are treated with blebbistatin ($R^2 = 0.37$) (Fig. 3-4B). The moderate correlation can largely be attributed to the Hs766T cells treated with blebbistatin; this outlier reduces the R^2 from 1.00. Overall, our data revealing the differential effects of blebbistatin on the stiffness and invasion of PDAC cell lines highlight that while there are shared molecular mediators of both cell stiffness and invasion, the factors that determine stiffness and/or invasion in a particular cell type may not operate with the same proportions across all cell types.

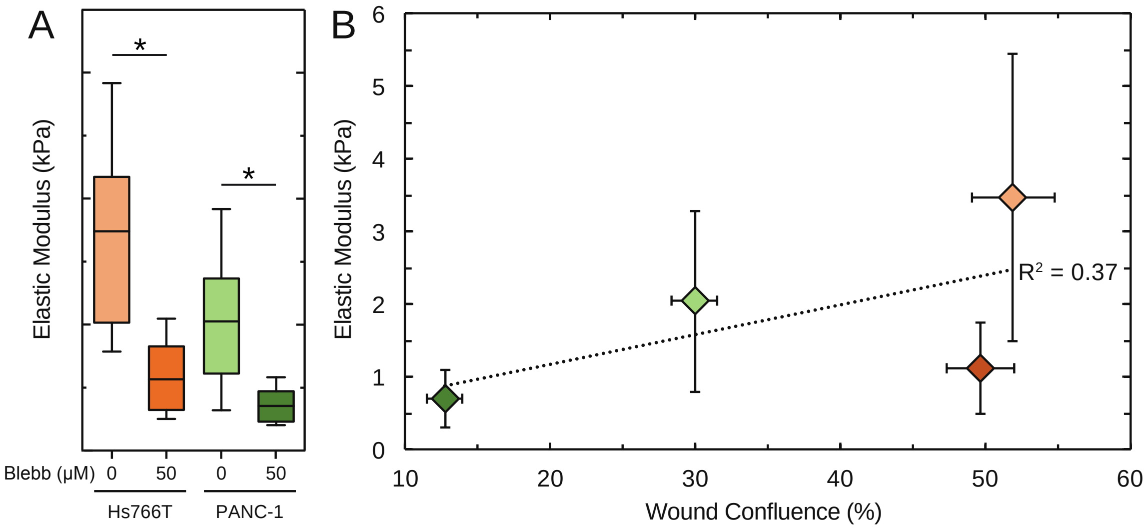

Figure 3-4. Myosin II activity contributes to PDAC cell stiffness. (A) Elastic modulus (*E*) of PDAC cells that are adhered to a glass surface coated with Matrigel and treated with DMSO (ctrl) or 50 µM blebbistatin for 30 min. Boxes represent the 25th and 75th percentiles, whiskers represent the 10th and student's t-test. *p < 0.05. Data represents 22-37 cells per treatment measured over 3 independent experiments. (B) Linear regression of elastic modulus obtained by AFM versus invasion measured as wound confluence by 3D scratch-wound invasion at 72 hours for PDAC cells treated with blebbistatin. R = Pearson's correlation coefficient.

Invasion is not altered by matrix metalloproteinase inhibition. We next investigate the activity of matrix metalloproteinases (MMPs) across PDAC cells as a possible explanation of why Hs766T cells are stiffer, most invasive, and do not rely on myosin II for invasion. MMPs provide major contributions to cancer cell invasion as these enzymes degrade the surrounding protein matrix and thereby enlarge the size of gaps that cells must deform into during invasion (59). The secretion of MMPs is also regulated/mediated by invadopodia, which generate forces as they protrude from the plasma membrane (60); thus, MMP production could also contribute to cell stiffness and provide an explanation of why stiffer cells are more invasive. To determine if Hs766T cells have increased levels of MMPs, we first analyze RNAseq data of our 3 PDAC cell lines. The Hs766T cells have a 145-fold and 36-fold higher in *MMP14* compared to MIA PaCa-2 and PANC-1 cells, as well as a 1716-fold and 1274-fold higher in *MMP28* expression levels (Supp Fig 3-3A). PANC-1 cells have a 4-fold and 425-fold higher expression of *MMP2* compared to the other two cell lines (Supp Fig 3-3A). MMP2, MMP14, MMP28 have all been implicated in the invasive potential of PDAC cells (61–64). However, MMP activity depends on secretion and activation of the proteinases, and thus cannot be predicted by transcript levels alone. Therefore, we next measure the activity of MMPs secreted from our PDAC cell lines using a Fluorescence Resonance Energy Transfer (FRET)-based MMP activity assay. We observe that Hs766T cells exhibits a 2.9-fold increase in MMP activity compared to MIA PaCa-2 ($p = 7.5 \times 10^{-8}$) cells and a 1.5-fold increase compared to PANC-1 cells ($p = 1.2 \times 10^{-5}$), while the PANC-1 cells have a 1.9-fold increase in MMP activity compared to the MIA paCa-2 cells ($p = 2.0 \times 10^{-9}$) (Supp Fig 3-3B). To determine the contributions of MMP activity to cell invasion, we next performed 3D invasion assays in the presence of the broad-spectrum MMP inhibitor GM6001. While treatment with 10 or 25 µM GM6001 significantly decreased MMP activity across all three PDAC cell lines (Supp Fig 3-3B), we observe no significant effect of MMP inhibition on the invasion of the Hs766T, MIA PaCa-2, or PANC-1 cells (Supp Fig 3-3C). These results indicate that the invasion of these PDAC cell lines – as measured by this 3D scratch-wound invasion assay – is not predominantly driven by MMPs. Thus, the increased invasion of Hs766T cells cannot be explained by increased MMP activity.

Arp2/3 and formin activity contribute to the invasion of Hs766T cells. While myosin II activity may explain why PANC-1 cells are stiffer and more invasive (Ref. 19, Fig. 3-1), it is still unclear what contributes to the concurrent increase in stiffness and invasion of the Hs766T cells. We hypothesized that Hs766T cells may utilize alternative, mechanisms for invasion that do not strongly rely on myosin II (65). For example, the generation of protrusive forces is critical for the formation of lamellipodia and invadopodia, structures that are implicated in cell invasion (40, 42). Two of the main components required for the formation of protrusions are formins and Arp2/3, which mediate actin nucleation and branching. Therefore, we hypothesize that the invasion of Hs766T cells relies on the activity Arp2/3 and formins, while myosin II dependent forces are more critical for the invasion of MIA PaCa-2 and PANC-1 cells.

A characteristic hallmark of myosin II-independent invasion is the formation of protrusions at the leading edge of an invading cell. We first evaluate differences in the morphology of our cell panel using confocal microscopy, and find that the Hs766T cells are much more elongated and polarized that the MIA Paca-2 and PANC-1 cells (data not shown). We next quantify the length of the front of invading cells in the 3D scratch wound invasion assays: a longer front length

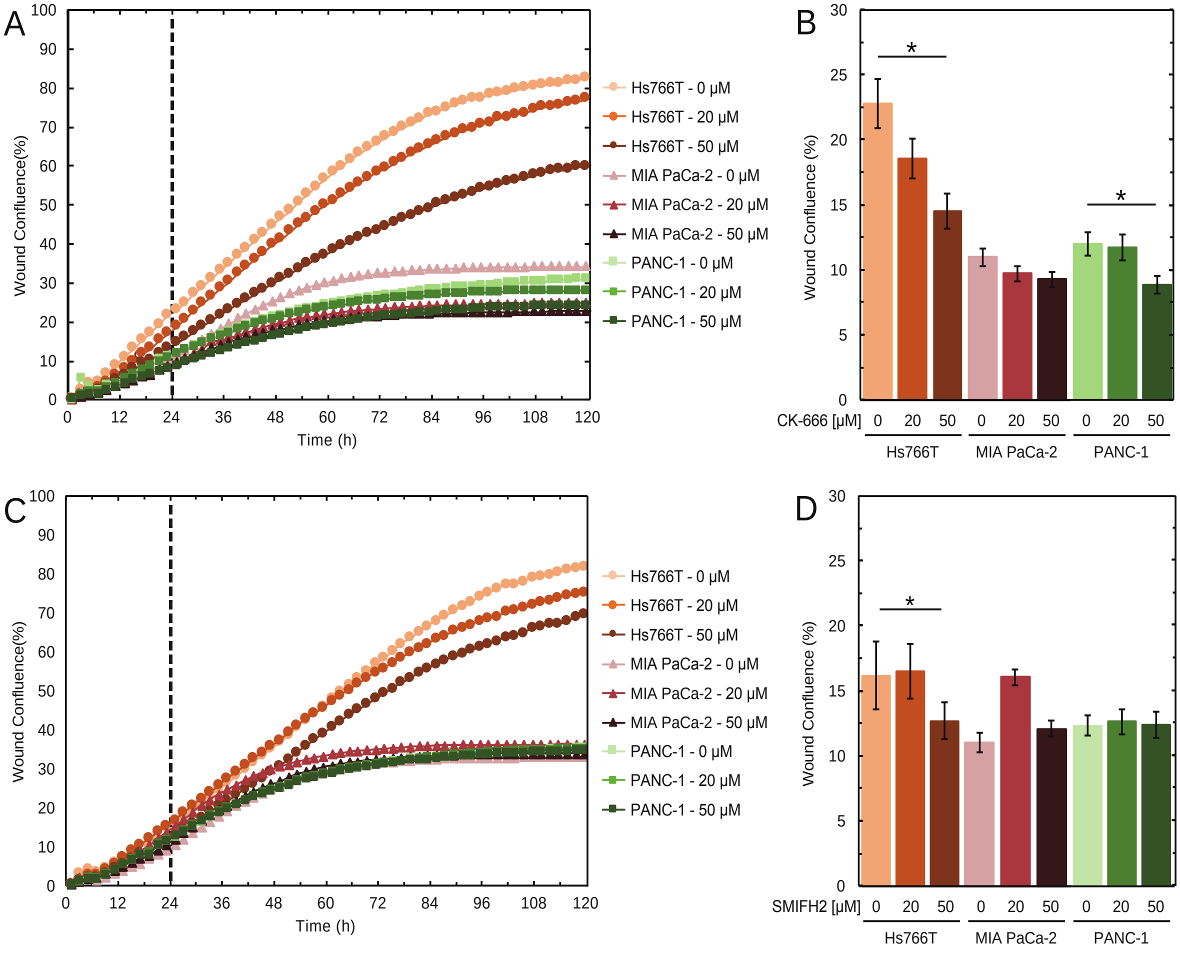

Figure 3-5. Activity of Arp2/3 and formin, which mediate actin nucleation and polymerization, are critical for the invasion of Hs766T cells. To assay invasion, we measure the wound confluence during a 3D scratch wound invasion assay. Scatter plot shows the quantification of wound confluence over time when cells are treated either with (A) CK-666 or (C) SMIFH2. Bar plots show quantification of wound confluence at 24 h for (B) CK-666 or (D) SMIFH2. The dotted line indicates the 24 h time point, which we use to compare wound confluence values for statistical significance. Pairwise p-values are determined by a student's t-test. *$p < 0.05$. Data shows average values over 3 experiments. Error bars represent standard errors.

indicates a higher number and/or length of protrusions, while a shorter front length reflects that the invading cell front exhibits fewer and/or shorter protrusions. We find that the Hs766T cells have an average invasion front length of 6283 ± 1461 µm compared 3680 ± 454 µm and 3119 ±

574 µm for the MIA PaCa-2 and PANC-1 cells (Supp. Fig. 3-2). These data suggest that Hs766T cells have increased protrusion formation compared to the MIA PaCa-2 and PANC-1 cells, which is consistent with invasion that depends on Arp2/3 and formin activity.

To define the role of actin nucleation and polymerization in PDAC cell invasion, we next determine the effect of Arp2/3 activity on PDAC cell invasion. We use the Arp2/3 inhibitor, CK-666, which is a small molecule inhibitor that stabilizes the inactive state of the complex by stopping the movement of the Arp2 and Arp3 subunits (66). We first determine how CK-666 affects cell proliferation, which can contribute to decreased invasion in this 3D scratch wound invasion assay. While we observe an overall decrease in cell proliferation at longer time points (Supp. Fig. 4), there are no effects on proliferation at time points less than 24 h. Interestingly, we find no significant differences in the invasion of PANC-1 and MIA PaCa-2 cells following 24 h of CK-666 treatment (Fig. 3-5A, 3-5B), suggesting that Arp2/3 inhibition does not significantly contribute to the invasion of these cell types through a Matrgiel protein matrix. However, we observe a significant decrease in invasion of the Hs766T cells with increasing CK-666 concentration (Fig. 3-5A, 3-5B). For example, Hs766T cells treated with 50 µM CK-666 have a wound confluence of 14% compared to 23% for untreated cells at 24 h ($p = 2.1 \times 10^{-4}$). These findings suggest that Arp2/3 activity is a major contributor to the invasion of Hs766T cells, while myosin II is a major contributor to the invasion of the MIA PaCa-2 and PANC-1 cells.

We next investigate how the activity of formins contributes to PDAC cell invasion since these proteins are integral in actin nucleation and polymerization (67). To evaluate how formin activity impacts PDAC cell invasion, we treat cells with the formin inhibitor SMIFH2, which is proposed to inhibit formin activity by binding to the FH2 domain of formins (68, 69). We find there is no significant difference in the invasion of MIA PaCa-2 and PANC-1 cells with SMIFH2 treatment compared to vehicle control (for 50 µM at 24 h, $p_{MIA} = 0.23$ $p_{PANC} = 0.91$) (Fig. 3-5C, 3-5D). However, we observe a small but statistically significant difference in Hs766T cells treated with SMIFH2 (Fig 3-5C, 3-5D). The Hs766T cells exhibit a wound confluence of 12% if treated with 50 µM SMIFH2 compared to 16% if treated with the DMSO vehicle control at 24 h ($p = 2.6 \times 10^{-2}$). Collectively, our results show that Hs766T cell invasion relies on the activity of Arp2/3 and formins, while the contributions of Arp2/3 and formins are less essential to the invasion of MIA PaCa-2 and PANC-1 cells.

Inhibition of actin filament formation decreases cell stiffness. We next perform AFM to determine whether actin filament formation plays a role in cell stiffness. To perturb actin filament formation, we treat the Hs766T and PANC-1 cells, the most invasive and stiffest PDAC cell lines of our panel, with either CK-666 to inhibit Arp2/3 or SMIFH2 to inhibit formins. As we observed with blebbistatin, both drugs also significantly decrease the Young's modulus of our PDAC cells (Fig. 3-6A, 3-6C), except when the PANC-1 cells are treated with CK-666. This treatment shows a 12%, but insignificant, decrease in Young's modulus. Our data confirm that PDAC cell stiffness is influenced by actin filament formation.

We again perform linear regression to evaluate the relationship between cell stiffness and invasion when PDAC cells are treated with CK-666 and SMIFH2. The R^2-values across for these drug treatments is much higher than those for blebbistatin treated PDAC cells (CK-666: $R^2 = 0.79$, SMIFH2: $R^2 = 0.75$, Blebbistatin: $R^2 = 0.37$) (Fig. 3-4B, 3-6B, 3-6D). These results highlight that the relationship between cell stiffness and invasion may be context-dependent, and that stiffness may only be a good indicator of cell invasion for certain conditions.

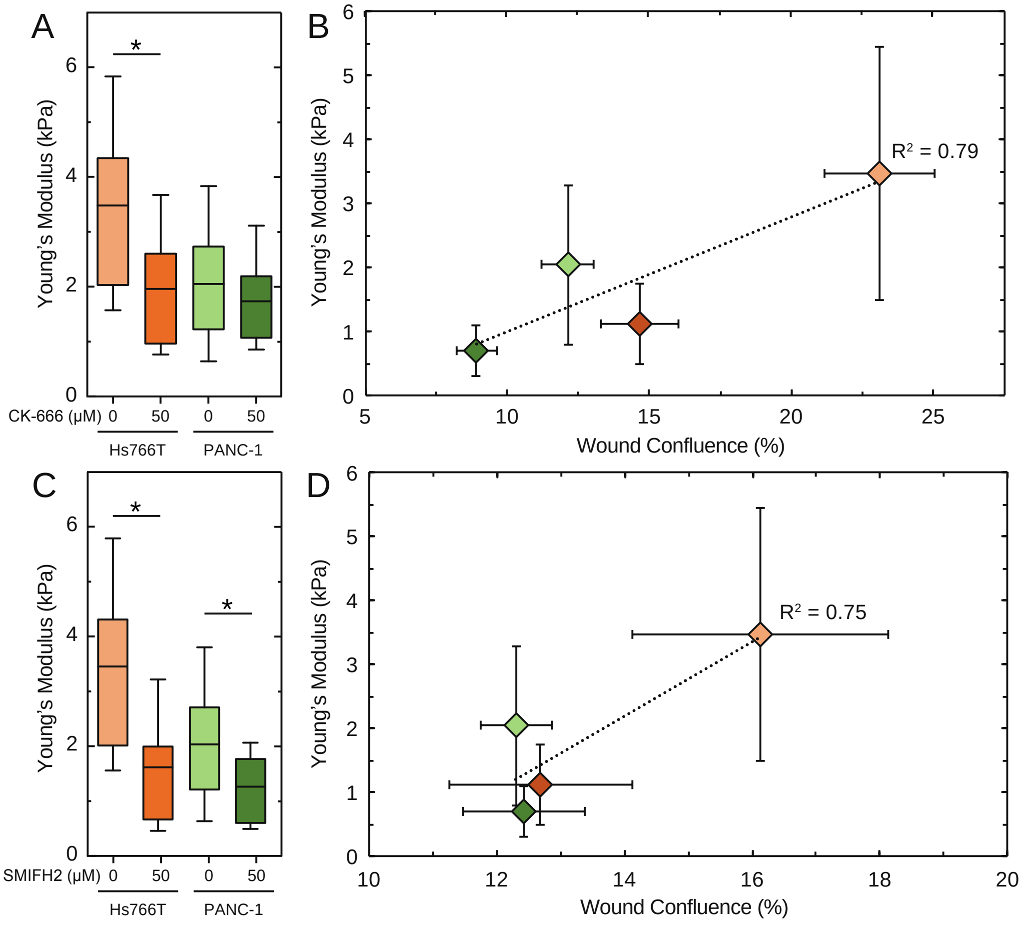

Figure 3-6. Arp2/3 and formin activity influence PDAC cell stiffness. The elastic modulus, *E*, of PDAC cells adhered to Matrigel-coated glass is measured using atomic force microscopy (AFM) when cells are treated with (A) 50 μM CK-666 or (C) 50 μM SMIFH2 for 30 minutes. Boxes represent the 25th and 75th percentiles, whiskers represent the 10th and 90th percentiles, and the horizontal line represents the median. Statistical significance calculated with Mann Whitney U test. $^*p < 0.05$. Linear regression of elastic modulus versus invasion, as measured by wound confluence using a 3D scratch-wound invasion (Fig. 5-5) for (B) CK-666 and (D) SMIFH2. R = Pearson's correlation coefficient.

Discussion

Here we show that the activity of three proteins involved in active force generation – myosin II, Arp2/3, and formins – provide a possible explanation for why stiffer PDAC cells are more invasive. Our measurements of stiffness with the inhibition of myosin II, Arp2/3, and formins show marked reductions in cell stiffness, suggesting that a decrease in actomyosin contractility and actin polymerization cause cells to be more compliant; these findings are consistent with *in vitro* studies of cultured cells (26, 35, 42), as well as studies that quantify the stiffness of isolated protein networks.

Our three cancer cell lines – the Hs766T, MIA PaCa-2, and PANC-1 – are all pancreatic ductal cells that have undergone oncogenic transformation. Each cell line of this panel carries three common founder mutations (*KRAS, TP53,* and *CDKN2A*), while the Hs766T cells have an additional *SMAD4* mutation (44). The Cancer Cell Line Encyclopedia (CCLE) (70) provides full genetic profiles and transcriptomics data for each of our three cell lines, yet analysis of the available RNAseq data does not fully predict the physical phenotype of our PDAC cells. For example, analysis of actin mRNA levels revealed that across the Hs766T, MIA PaCa-2, and PANC-1 cells, this protein is one of the most differentially expressed. Yet upon analysis of actin levels with western blotting, we found less than a 2-fold differences in protein levels (19). Further, RNA-seq analysis of MMPs predicted that Hs766T cells have a ~3-fold higher expression level of MMPs (Supp. Fig. 5-3A) but when we measure the MMP activity across our PDAC cell lines, we find that MMP activity is only ~30% greater in Hs766T cells compared to PANC-1 cells. Similarly, expression analysis of myosin proteins (Supp. Fig. 5-5) show that the Hs766T cells have the highest expression of MYH9 and MYH10, yet the PANC-1 cells exert a higher level of contractile forces as measured by our cell rounding and micropillar assays (Fig. 5-2, 5-3). Thus, our RNA-seq analysis suggests that that physical phenotypes that are influenced by proteins of the mechanome and contractome, cannot be fully explained by analysis of genetics or transcriptomics alone, as these physical phenotypes may be influenced by post-translational modifications, as well as higher-order protein structure or dynamics and remodeling, that contribute to cellular phenotypes and behaviors.

Context-dependent relationship between cell stiffness and invasion. Our results highlight the context-dependent relationship between cell stiffness and invasion. While we previously found a strong correlation between the stiffness and invasion of untreated PDAC cell lines ($R^2 = 1.00$) (19), we find only a moderate correlation between cell stiffness and invasion when cells are treated with blebbistatin, CK-666, or SMIFH2 ($R^2 = 0.45$) (Fig. 5-7A). Since cell stiffness and invasion are not strongly correlated in all contexts, the analysis of multiple physical phenotypes, such as adhesion and contractility, may provide stronger indicators of invasion or metastatic potential than single parameters, such as deformability. Multivariate analysis of physical phenotypes enhances cell classification (71). Therefore, measurements of additional physical phenotypes may enhance the applicability of physical phenotypes as a biomarker for cancer cell invasion across PDAC samples, as well as different tissue types.

The origin of the weakened correlation reflects the differential effects of drugs, such as blebbistatin, on the invasion of different cell lines. For example, while blebbistatin treatment decreases the stiffness of both Hs766T and PANC-1 cells, only the invasion potential of PANC-1 cells decreases. The differential effect across cell lines may stem from the multiple roles of proteins involved in cell stiffness and invasion. For instance, in addition to its contribution to actomyosin contractility, myosin II also acts as an actin crosslinker (58). We speculate that blebbistatin treatment decreases the crosslinking density of actin in the Hs766T cells, thus also decreases stiffness, yet only has a subtle effect on invasion since the Hs766T cells may use alternative modes of invasion. Therefore, while the inhibition of myosin II activity decreases the invasion of MIA PaCa-2 and PANC-1 cells, it appears to be less essential for the invasion of Hs766T cells. Similarly, Arp2/3 and formin activity are major contributors to the invasion of Hs766T but not MIA PaCa-2 and PANC-1 cells, yet still decreases the stiffness of PANC-1 cells. While the regulation of invasion by different modes is well described (72, 73), how these mechanisms determine cell stiffness are not as well defined. Our data suggest that while there are common proteins involved in cell stiffness and invasion, individual proteins may not effect each phenotype equally, and that different cell lines may utilize proteins to different extents.

It is important to acknowledge how cell mechanotype may be affected by the measurement method, which can vary in the time and lengthscales of deformation as well as state of cells during measurement. In this study, we use AFM to measure the stiffness of cells that are adhered to a Matrigel-coated surface, revealing that the stiffest to most compliant cells are Hs766T> PANC-1 > MIA PaCa-2. We previously measured these same cells in a suspended state using the microfluidic-based method, quantitative deformability cytometry (q-DC) (19, 74). Interestingly, we found that the ranking of cell stiffness using q-DC was PANC-1 > Hs766T> MIA PaCa-2. While there are differences in the time and lengthscale of deformations between AFM and q-DC – nanometer-scale deformations over seconds by AFM versus micron-scale deformations over milliseconds in q-DC – there are also clear differences in both intrinsic and extrinsic factors that determine cell mechanotype when cells are in an adhered versus suspended state. For example, when cells are adhered to their substrate via integrins and focal adhesion, cells exert traction stresses, which promote the activity of myosin II and increases the generation of contractile forces and intracellular tension. Tractions stresses in turn increase the stiffness (75) and invasive behavior of cancer cells (76). By contrast, fluidic methods, such as microfluidic q-DC, measure cells in a suspended state, where cortical actin (77) and the nucleus (24, 25) contribute to the deformation of cells through micron-scale pores. Thus, the mechanotype of suspended cells may be less dependent on intracellular tension and more predominantly reflect intrinsic factors, such as levels of cytoskeletal proteins. Comparisons of the same types of PDAC cell lines using multiple, complementary methods provides more detailed insights into cancer cell mechanotype.

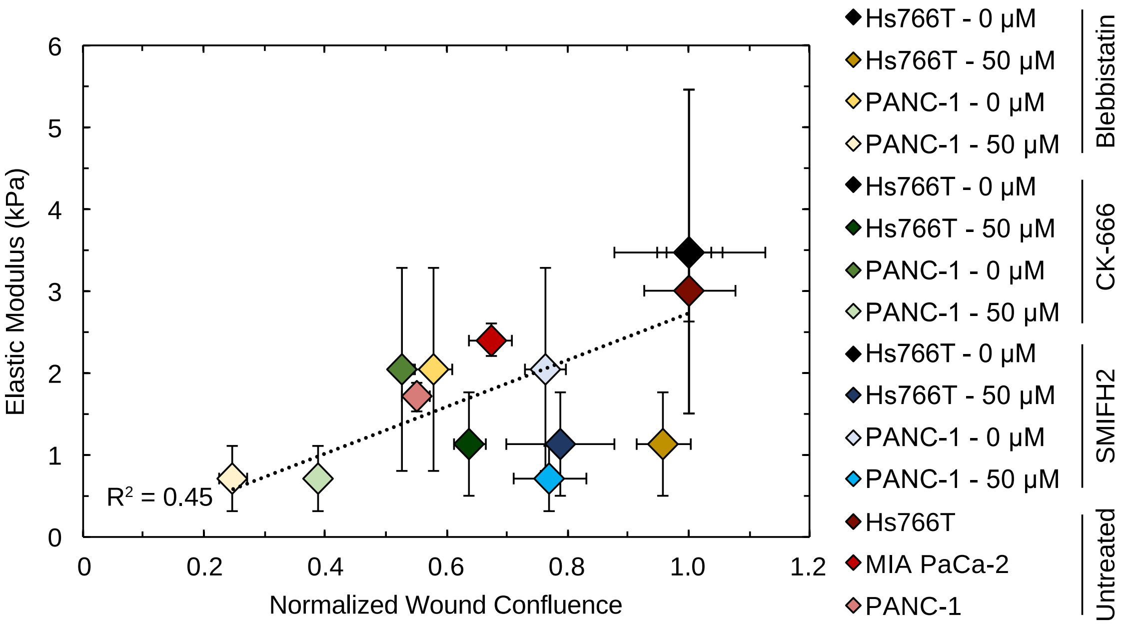

Figure 3-7. Linear regression of elastic modulus versus invasion, as measured as wound confluence by 3D scratch-wound invasion for untreated PDAC cells, as well as PDAC cells treated with blebbistatin, CK-666, or SMIFH2. R = Pearson's correlation coefficient.

Strategies of invasion.

Our results showing the differential effects of myoII, Arp2/3, and formin inhibitors on different cell types suggest that cancer cells may have alternative strategies for invasion. Interestingly the PDAC cells we investigate are derived from similar tissue sources. The different physical phenotypes that we observe across cell lines could thus represent both intra-tumor and inter-patient heterogeneity, which could be attributed to genetic variations or phenotypic variability of isogenic cells. For example, the PANC-1 and MIA PaCa-2 cell lines have similar genetic background but differing invasion potential. The Hs766T cells have an additional SMAD4 mutation, which could contribute to additional variability in the physical phenotypes across Hs766T, MIA PaCa-2 and PANC-1 cells.

We previously found that the stiffest, most invasive cells, Hs766T, have higher levels of lamin A compared to other PDAC cell lines. While high levels of lamin A associated with decreased ability of cells to deform through narrow gaps (24, 25), low levels of lamin A can promote nuclear rupture and DNA damage (27, 28). The ability of the cell nucleus to resist deformation may also enhance invadopodia formation (60). It is intriguing to speculate that cells with higher levels of lamin A use different modes of force generation to optimize invasion, or protect the nucleus from shape changes and DNA damage.

Why understanding mechanotype is valuable.

Our analysis of cell mechanotype during pharmacological inhibition of active force generation provides deeper insights into functional behaviors, such as invasion. While cell mechanical properties, including deformability and contractility, are regulated by similar sets of proteins that also regulate motility, we find that some drug treatments result in decreased cell stiffness without a significant change to cell invasion, suggesting that different PDAC cell lines may use different mechanisms to invade. Given the heterogeneity of cancer cells within a single patient and across different patients, it may be an important clinical strategy to devise a multi-arm treatment plan to inhibit cell invasion and metastasis since blocking a single pathway may cause cells to adapt to another. Collectively, we find that the relationship between stiffness and invasion is complex and requires deeper mechanistic studies before application in a clinical setting yet establish the foundation to more deeply understand the physical phenotypes of PDAC cells.

Experimental Methods

Cell Culture

Pancreatic ductal adenocarcinoma (PDAC) cell lines (Hs766T, MIA PaCa-2, and PANC-1) are from the American Type Culture Collection (ATCC). Cells are cultured at 5% CO2 and 37°C in high glucose, L-glutamine Dulbecco's Modified Eagle Medium (DMEM) (Life Technologies) with 10% fetal bovine serum and 1% v/v penicillin-streptomycin (Gemini BioProducts). To inhibit myosin II, Arp2/3, and formins, cells are treated with either vehicle control (DMSO), 20 µM, or 50 µM of blebbistatin, CK-666, and SMIFH2. For AFM and micropillar experiments, cells are treated with drugs for 30 min; for scratch-wound invasion experiments, cells are treated for 5 days. To inhibit matrix metalloproteinases (MMPs), cells are treated for 48 h with 10 or 25 µM GM6001.

Atomic Force Microscopy (AFM)

AFM is performed as previously described (19) using the MFP-3D-BIO system (Asylum Research, Oxford Instruments). Cells are probed with the “C” tip of an MLCT probe (Bruker). The sensitivity and spring constant of each probe are calibrated before each experiment. Force curves are acquired by indenting the cytoplasmic region of 20 to 30 cells for each cell line and drug treatment. Approach and retract speeds for all experiments are 5 µm/s. The elastic modulus for each cell is determined by fitting force curves to the Hertz-Sneddon model using Asylum Research software.

Scratch Wound Invasion and Proliferation Assays

We perform invasion and proliferation assays using the IncuCyte time-lapse imaging system (EssenBioscience). To measure cell invasion through a 3D matrix, we perform scratch wound invasion assays with Matrigel to simulate the ECM. We plate cells in the wells of a 96-well plate at 95% confluency, create a scratch wound (EssenBioscience WoundMaker), overlay the scratch with 8 mg/ml Matrigel (Corning), and perform time-lapse imaging using the IncuCyte Zoom at 5% CO2 and 37°C. Phase contrast images of cells are acquired every 4 hours for 120 hours. We determine the confluence of cells in the wound area at each time point using quantitative image analysis (Essen Bioscience). Since scratch wound invasion assays may be influenced by cell proliferation, we also measure percent confluence by sparsely plating cells (20% confluency) and acquiring phase contrast images every 2 hours for 120 hours. To quantify the number of protrusions at the invasion front, the length of each invasion front is measured using the free hand tool of ImageJ.

Cell Rounding Assay

To determine the cell rounding time constant, we measure the rate of cell rounding after trypsinization. We plate cells to 40% confluency in a 60 mm petri dish coated with 100 µg/ml Matrigel (overnight at 37℃), wash twice with 1X phosphate buffered saline (Corning), and then treat with 1X trypsin-EDTA to induce cell rounding (Gemini BioProducts). To quantify changes in cell shape during rounding, we acquire images every 10 s starting immediately before trypsin-EDTA is added (t = 0 s). Cell area is determined using a custom MatLab (Mathworks) script. The rounding time constant is determined by fitting exponential decay curves to experimental data starting at 45 s to account for the delay in cell contraction observed after trypsin is added (Sen et al, Cell. and Mol. Bioengineering 2009).

Micropillar Traction Stress Assay

Gold micro-disks on top of PDMS micropillars were fabricated in a similar fashion as in F. Xiao *et al*. (78). Darkfield images of 10 regions were taken before cell seeding. After drug treatments, we fix the cells with 4% paraformaldehyde for 15 mins at 37℃. To fluorescently label cells, we use Wheat Germ Agglutinin (WGA), Alexa Fluor 488 conjugate (Invitrogen). The same 10 regions of the micropillar devices are then imaged using both darkfield and fluorescent microscopy. Displacement of gold-tipped pillars are quantified by tracking darkfield images of the pillars, and forces are determined by the following equation:

$$F = \frac{4}{3}\pi E \frac{r^4}{L^3}\, \Delta x$$

Where *F* is the force exerted by a cell on the pillar, *E* is the elastic modulus of the PDMS, *r* is the radius of the pillar, *L* is the height of the pillar, and *x* is the horizontal displacement of the pillar.

Matrix Metalloproteinase (MMP) Activity Assay

To measure activity of MMPs, we use the red MMP activity assay (abcam). In brief, we retrieve 90 µl of conditioned media from each well of a 96-well plate after 18 h of culture from wells that have cells at ~30 % confluency. Media is transferred to a black-walled, clear-bottom 96-well plate (Greiner BioProducts, catalog no. 969500). To inhibit MMP activity, we treat cells with 0, 10, or 25 µM GM6001 (MMP inhibitor) for 48 hours before measuring MMP activity.

Statistical analysis

All data are obtained from at least 3 independent experiments. For data with normal distributions, we determine statistical significance using a student's t-test (Excel, Microsoft). For data that exhibit a non-normal distribution, we perform bootstrapping to obtain the bootstrapped median and confidence intervals; we then use the Mann-Whitney U test to determine statistically significant differences between non-normal distributions using Matlab (Mathworks) and Origin (OriginLab).

Acknowledgements

We would like to thank Timothy Donahue and his laboratory for their insight into PDAC, as well as their generous contributions of the PDAC cell lines used in our studies. The MMP activity assay was performed in the UCLA Molecular Shared Screening Resource in the California NanoSystems Institute. We are grateful for our funding from the NSF (CAREER DBI-1254185 to ACR), the NIH/National Center for Advancing Translational Science (NCATS) (UCLA CTSI Grant Number UL1TR000124), and the Farber Family Foundation. AVN is supported by a

David Geffen Scholarship and the UCLA-IBP Eureka Scholarship Fund. MJB is supported by the National Institute of Health (R01 GM110482).

Supplemental Figures

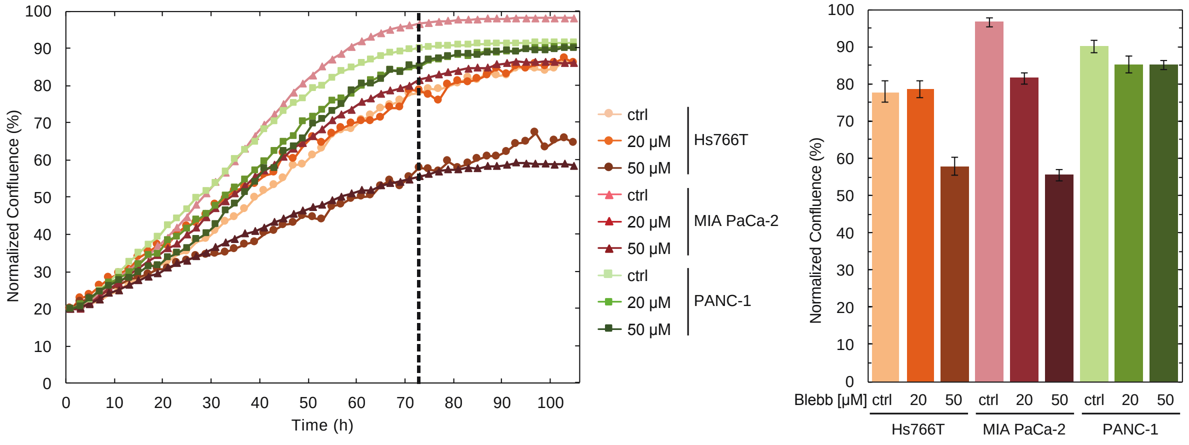

Supplemental Figure 3-1. Blebbistatin decreases proliferation of Hs766T and MIA PaCa-2 cells. (A) Proliferation measured by confluence of cell populations. Line plot shows the quantification of confluence over time. The dotted line indicates the 72 h time point, which we use to compare wound confluence values for statistical significance. Cells are treated with blebbistatin or DMSO (ctrl) from t = 0. (B) Bar plot showing average wound confluence at the 72 h time point. Error bars represent standard error from 3 independent experiments. Pairwise p-values are determined by a student's t-test. $^{*}p < 0.05$.

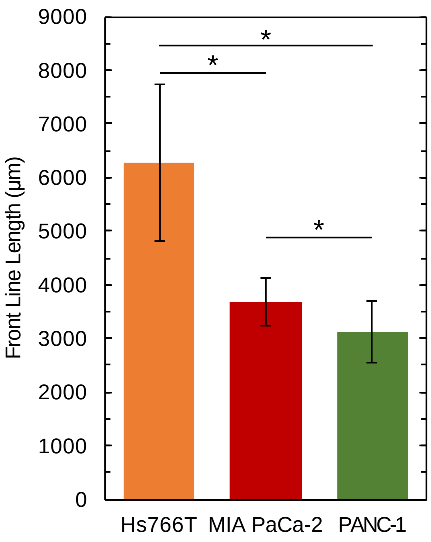

Supplemental Figure 3-2. Hs766T cells have a greater front line length than MIA PaCa-2 and PANC-1 cells. Front line length measured from representative IncuCyte invasion images. Error bars represent standard deviation from 3 independent experiments. Pairwise p-values are determined by a student's t-test. *$p < 0.05$.

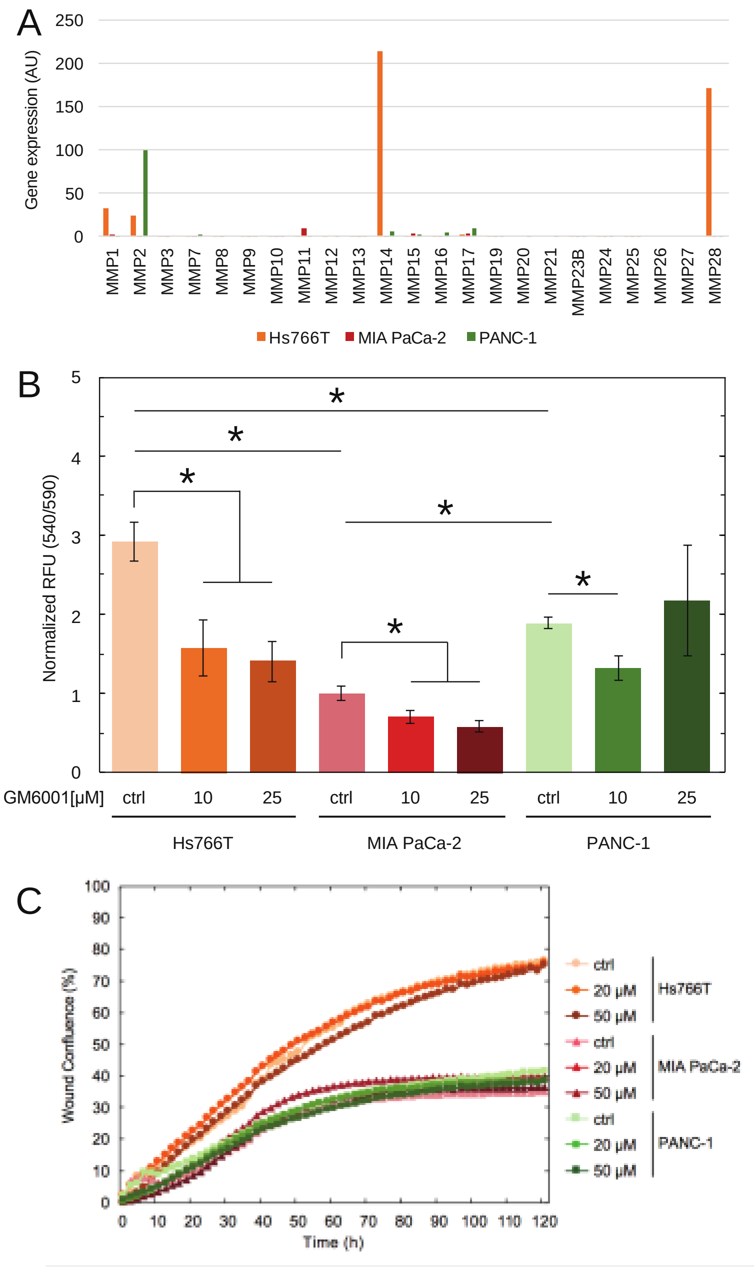

Supplemental Figure 3-3. MMP activity does not influence PDAC cell invasion through a protein matrix. (A) RNAseq analysis of the gene expression of various MMPs. Bar plot represents arbitrary expression values of the denoted protein for each cell line. (B) MMP activity levels of PDAC cell panel normalized to cell number. Error bars represent standard deviation from 3 independent experiments. Pairwise p-values are determined by a student's t-test. *$p < 0.05$. (C) Invasion through Matrigel is measured by wound confluence in 3D scratch wound invasion assays. Scatter plot shows the quantification of wound confluence over time. Cells are treated with the MMP inhibitor GM6001 or DMSO (ctrl) from t = 0.

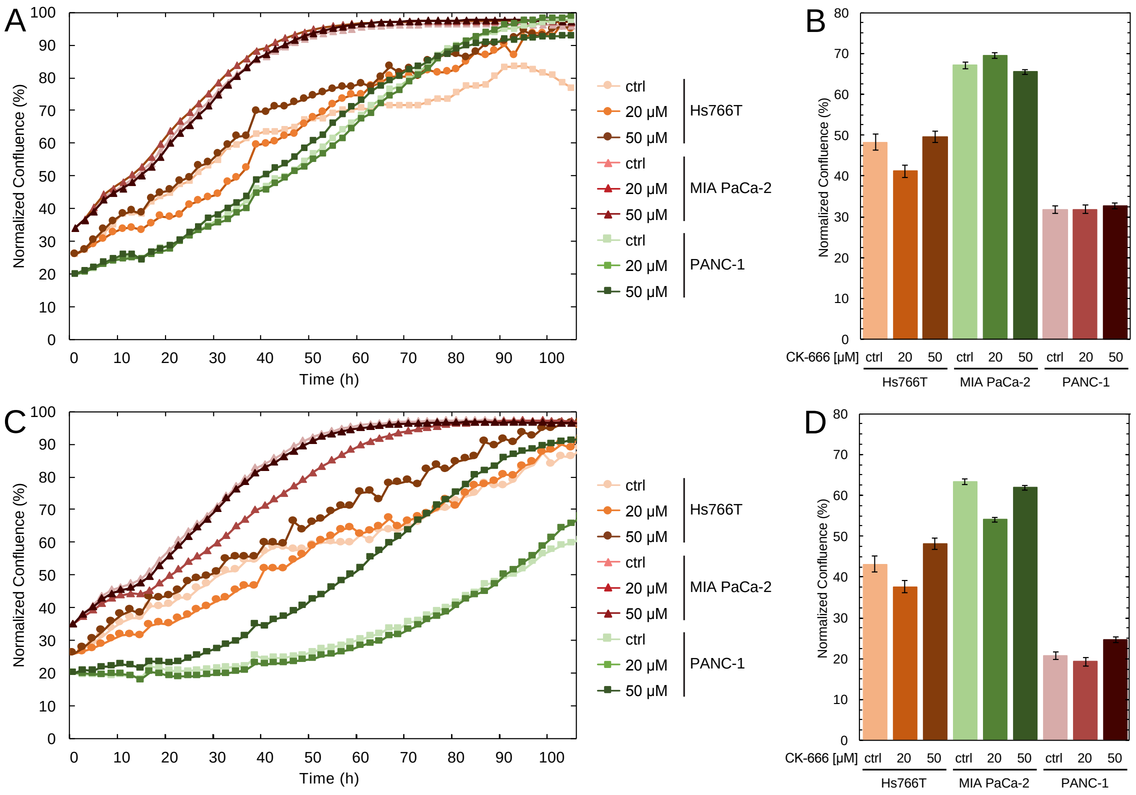

Supplemental Figure 3-4. CK-666 and SMIFH2 do not significantly affect PDAC cell proliferation at 24 h. (A) Proliferation measured by confluence of cell populations. Line plot shows the quantification of confluence over time. The dotted line indicates the 24 h time point, which we use to compare wound confluence values for statistical significance. Cells are treated with CK-666 or DMSO (ctrl) from t = 0. (B) Bar plot showing average wound confluence at the 24 h time point. (C) Proliferation measured by confluence of cell populations. Line plot shows the quantification of confluence over time. The dotted line indicates the 24 h time point, which we use to compare wound confluence values for statistical significance. Cells are treated with CK-666 or DMSO (ctrl) from t = 0. (D) Bar plot showing average wound confluence at the 24 h time point. Error bars represent standard error from 3 independent experiments. Pairwise p-values are determined by a student's t-test. *$p < 0.05$.

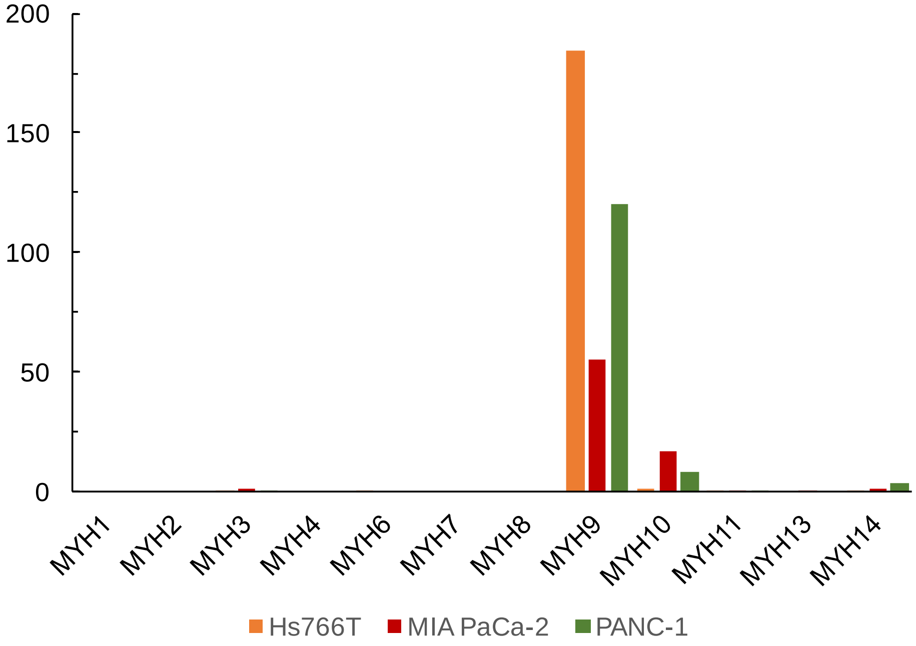

Supplemental Figure 3-5. Myosin expression levels across panel of PDAC cell lines. Bar plot represents arbitrary expression values of the denoted protein for each cell line.

References

1. Beadle Christopher, C, A. M., Pascale, M., Richard, V., S, R. S., and Peter, C. (2008) The Role of Myosin II in Glioma Invasion of the Brain. *Mol. Biol. Cell*. **19**, 3357–3368
2. Xu, W., Mezencev, R., Kim, B., Wang, L., McDonald, J., and Sulchek, T. (2012) Cell stiffness is a biomarker of the metastatic potential of ovarian cancer cells. *PLoS One*. **7**, e46609
3. Wirtz, D., Konstantopoulos, K., and Searson, P. C. (2011) The physics of cancer: the role of physical interactions and mechanical forces in metastasis. *Nat. Rev. Cancer*. **11**, 512–522
4. Kim, T.-H., Rowat, A. C., and Sloan, E. K. (2016) Neural regulation of cancer: from mechanobiology to inflammation. *Clin. Transl. Immunol.* **5**, e78
5. Tse, H. T. K., Gossett, D. R., Moon, Y. S., Masaeli, M., Sohsman, M., Ying, Y., Mislick, K., Adams, R. P., Rao, J., and Di Carlo, D. (2013) Quantitative diagnosis of malignant pleural effusions by single-cell mechanophenotyping. *Sci. Transl. Med.* **5**, 212ra163
6. Chin, L., Xia, Y., Discher, D. E., and Janmey, P. A. (2016) Mechanotransduction in Cancer. *Curr. Opin. Chem. Eng.* **11**, 77–84
7. Jaqaman, K., and Grinstein, S. (2012) Regulation from within: the cytoskeleton in transmembrane signaling. *Trends Cell Biol.* **22**, 515–26
8. Yachida, S., Jones, S., Bozic, I., Antal, T., Leary, R., Fu, B., Kamiyama, M., Hruban, R. H., Eshleman, J. R., Nowak, M. A., Velculescu, V. E., Kinzler, K. W., Vogelstein, B., and Iacobuzio-Donahue, C. A. (2010) Distant metastasis occurs late during the genetic evolution of pancreatic cancer. *Nature*. **467**, 1114–7
9. Shi, Q., Hjelmeland, A. B., Keir, S. T., Song, L., Wickman, S., Jackson, D., Ohmori, O.,

Bigner, D. D., Friedman, H. S., and Rich, J. N. (2007) A novel low-molecular weight inhibitor of focal adhesion kinase, TAE226, inhibits glioma growth. *Mol. Carcinog.* **46**, 488–496

10. Kim, S., and Coulombe, P. A. (2010) Emerging role for the cytoskeleton as an organizer and regulator of translation. *Nat. Rev. Mol. Cell Biol.* **11**, 75–81

11. Laklai, H., Miroshnikova, Y. A., Pickup, M. W., Collisson, E. A., Kim, G. E., Barrett, A. S., Hill, R. C., Lakins, J. N., Schlaepfer, D. D., Mouw, J. K., LeBleu, V. S., Roy, N., Novitskiy, S. V, Johansen, J. S., Poli, V., Kalluri, R., Iacobuzio-Donahue, C. A., Wood, L. D., Hebrok, M., Hansen, K., Moses, H. L., and Weaver, V. M. (2016) Genotype tunes pancreatic ductal adenocarcinoma tissue tension to induce matricellular fibrosis and tumor progression. *Nat. Med.* **22**, 497–505

12. Vennin, C., Chin, V. T., Warren, S. C., Lucas, M. C., Herrmann, D., Magenau, A., Melenec, P., Walters, S. N., Del Monte-Nieto, G., Conway, J. R. W., Nobis, M., Allam, A. H., McCloy, R. A., Currey, N., Pinese, M., Boulghourjian, A., Zaratzian, A., Adam, A. A. S., Heu, C., Nagrial, A. M., Chou, A., Steinmann, A., Drury, A., Froio, D., Giry-Laterriere, M., Harris, N. L. E., Phan, T., Jain, R., Weninger, W., McGhee, E. J., Whan, R., Johns, A. L., Samra, J. S., Chantrill, L., Gill, A. J., Kohonen-Corish, M., Harvey, R. P., Biankin, A. V, Australian Pancreatic Cancer Genome Initiative (APGI), Evans, T. R. J., Anderson, K. I., Grey, S. T., Ormandy, C. J., Gallego-Ortega, D., Wang, Y., Samuel, M. S., Sansom, O. J., Burgess, A., Cox, T. R., Morton, J. P., Pajic, M., and Timpson, P. (2017) Transient tissue priming via ROCK inhibition uncouples pancreatic cancer progression, sensitivity to chemotherapy, and metastasis. *Sci. Transl. Med.* **9**, eaai8504

13. Tsuno, A., Nasu, K., Kawano, Y., Yuge, A., Li, H., Abe, W., and Narahara, H. (2011)

Fasudil Inhibits the Proliferation and Contractility and Induces Cell Cycle Arrest and Apoptosis of Human Endometriotic Stromal Cells: A Promising Agent for the Treatment of Endometriosis. *J. Clin. Endocrinol. Metab.* **96**, E1944–E1952

14. Rother, J., Nöding, H., Mey, I., and Janshoff, A. (2014) Atomic force microscopy-based microrheology reveals significant differences in the viscoelastic response between malign and benign cell lines. *Open Biol.* [online] http://rsob.royalsocietypublishing.org/content/4/5/140046 (Accessed September 7, 2017)
15. Cross, S. E., Jin, Y.-S., Rao, J., and Gimzewski, J. K. (2007) Nanomechanical analysis of cells from cancer patients. *Nat. Nanotechnol.* **2**, 780–783
16. Faria, E. C., Ma, N., Gazi, E., Gardner, P., Brown, M., Clarke, N. W., Snook, R. D., Vickerman, J. C., Clarke, N. W., Shanks, J. H., Scott, L. J., Hart, C. A., and Brown, M. (2008) Measurement of elastic properties of prostate cancer cells using AFM. *Analyst.* **133**, 1498
17. Rathje, L.-S. Z., Nordgren, N., Pettersson, T., Rönnlund, D., Widengren, J., Aspenström, P., and Gad, A. K. B. (2014) Oncogenes induce a vimentin filament collapse mediated by HDAC6 that is linked to cell stiffness. *Proc. Natl. Acad. Sci. U. S. A.* **111**, 1515–20
18. Yu, H. W., Chen, Y. Q., Huang, C. M., Liu, C. Y., Chiou, A., Wang, Y. K., Tang, M. J., and Kuo, J. C. (2015) ??-PIX controls intracellular viscoelasticity to regulate lung cancer cell migration. *J. Cell. Mol. Med.* **19**, 934–947
19. Nguyen, A. V., Nyberg, K. D., Scott, M. B., Welsh, A. M., Nguyen, A. H., Wu, N., Hohlbauch, S. V., Geisse, N. A., Gibb, E. A., Robertson, A. G., Donahue, T. R., Rowat, A. C., Vogelstein, B., Iacobuzio-Donahue, C. A., Damania, D., Davies, P. C. W., Decuzzi, P., Dickinson, L., Estevez-Salmeron, L., Estrella, V., Ferrari, M., Fischbach, C., Foo, J.,

Fraley, S. I., Frantz, C., Fuhrmann, A., Gascard, P., Gatenby, R. A., Geng, Y., Gerecht, S., Gillies, R. J., Godin, B., Grady, W. M., Greenfield, A., Hemphill, C., Hempstead, B. L., Hielscher, A., Hillis, W. D., Holland, E. C., Ibrahim-Hashim, A., Jacks, T., Johnson, R. H., Joo, A., Katz, J. E., Kelbauskas, L., Kesselman, C., King, M. R., Konstantopoulos, K., Kraning-Rush, C. M., Kuhn, P., Kung, K., Kwee, B., Lakins, J. N., Lambert, G., Liao, D., Licht, J. D., Liphardt, J. T., Liu, L., Lloyd, M. C., Lyubimova, A., Mallick, P., Marko, J., McCarty, O. J. T., Meldrum, D. R., Michor, F., Mumenthaler, S. M., Nandakumar, V., O'Halloran, T. V., Oh, S., Pasqualini, R., Paszek, M. J., Philips, K. G., Poultney, C. S., Rana, K., Reinhart-King, C. A., Ros, R., Semenza, G. L., Senechal, P., Shuler, M. L., Srinivasan, S., Staunton, J. R., Stypula, Y., Subramanian, H., Tlsty, T. D., Tormoen, G. W., Tseng, Y., Oudenaarden, A. van, Verbridge, S. S., Wan, J. C., Weaver, V. M., Widom, J., Will, C., Wirtz, D., Wojtkowiak, J., and Wu, P.-H. (2016) Stiffness of pancreatic cancer cells is associated with increased invasive potential. *Integr. Biol.* **8**, 1232–1245

20. Kim, T.-H., Gill, N. K., Nyberg, K. D., Nguyen, A. V., Hohlbauch, S. V., Geisse, N. A., Nowell, C. J., Sloan, E. K., and Rowat, A. C. (2016) Cancer cells become less deformable and more invasive with activation of β-adrenergic signaling. *J. Cell Sci.* [online] http://jcs.biologists.org/content/129/24/4563 (Accessed September 7, 2017)

21. Katt, M. E., Placone, A. L., Wong, A. D., Xu, Z. S., and Searson, P. C. (2016) In Vitro Tumor Models: Advantages, Disadvantages, Variables, and Selecting the Right Platform. *Front. Bioeng. Biotechnol.* **4**, 12

22. Lopez, J. I., Kang, I., You, W.-K., McDonald, D. M., and Weaver, V. M. (2011) In situ force mapping of mammary gland transformation. *Integr. Biol.* **3**, 910

23. Plodinec, M., Loparic, M., Monnier, C. a, Obermann, E. C., Zanetti-Dallenbach, R., Oertle, P., Hyotyla, J. T., Aebi, U., Bentires-Alj, M., Lim, R. Y. H., and Schoenenberger, C.-A. (2012) The nanomechanical signature of breast cancer. *Nat. Nanotechnol.* **7**, 757–65

24. Rowat, A. C., Jaalouk, D. E., Zwerger, M., Ung, W. L., Eydelnant, I. a, Olins, D. E., Olins, A. L., Herrmann, H., Weitz, D. a, and Lammerding, J. (2013) Nuclear envelope composition determines the ability of neutrophil-type cells to passage through micron-scale constrictions. *J. Biol. Chem.* **288**, 8610–8

25. Harada, T., Swift, J., Irianto, J., Shin, J. W., Spinler, K. R., Athirasala, A., Diegmiller, R., Dingal, P. C. D. P., Ivanovska, I. L., and Discher, D. E. (2014) Nuclear lamin stiffness is a barrier to 3D migration, but softness can limit survival. *J. Cell Biol.* **204**, 669–682

26. Swaminathan, V., Mythreye, K., Tim O'Brien, E., Berchuck, A., Blobe, G. C., and Superfine, R. (2011) Mechanical Stiffness grades metastatic potential in patient tumor cells and in cancer cell lines. *Cancer Res.* **71**, 5075–5080

27. Denais, C. M., Gilbert, R. M., Isermann, P., Mcgregor, A. L., Lindert, M., Weigelin, B., Davidson, P. M., Friedl, P., Wolf, K., and Lammerding, J. (2016) Nuclear envelope rupture and repair during cancer cell migration. *Science (80-.).* **352**, 353–358

28. Raab, M., Gentili, M., Belly, H. De, Thiam, H., Vargas, P., Jimenez, A. J., Lautenschlaeger, F., Voituriez, R., Manel, N., and Piel, M. (2016) ESCRT III repairs nuclear envelope ruptures during cell migration to limit DNA damage and cell death. *Science (80-.).* **352**, 359–362

29. Gardel, M. L., Schneider, I. C., Aratyn-Schaus, Y., and Waterman, C. M. (2010) Mechanical Integration of Actin and Adhesion Dynamics in Cell Migration. *Annu. Rev. Cell Dev. Biol.* **26**, 315–333

30. Mendez, M. G., Kojima, S.-I., and Goldman, R. D. (2010) Vimentin induces changes in cell shape, motility, and adhesion during the epithelial to mesenchymal transition. *FASEB J.* **24**, 1838–51

31. RIDLEY, A. J. (2013) RhoA, RhoB and RhoC have different roles in cancer cell migration. *J. Microsc.* **251**, 242–249

32. Chan, C. K., Pan, Y., Nyberg, K., Marra, M. A., Lim, E. L., Jones, S. J. M., Maar, D., Gibb, E. A., Gunaratne, P. H., Robertson, A. G., and Rowat, A. C. (2016) Tumour-suppressor microRNAs regulate ovarian cancer cell physical properties and invasive behaviour. *Open Biol.* [online] http://rsob.royalsocietypublishing.org/content/6/11/160275.long (Accessed September 7, 2017)

33. Fletcher, D. A., and Mullins, R. D. (2010) Cell mechanics and the cytoskeleton. *Nature*. **463**, 485–92

34. Calzado-Martín, A., Encinar, M., Tamayo, J., Calleja, M., and San Paulo, A. (2016) Effect of Actin Organization on the Stiffness of Living Breast Cancer Cells Revealed by Peak-Force Modulation Atomic Force Microscopy. *ACS Nano*. **10**, 3365–3374

35. Cartagena-Rivera, A. X., Logue, J. S., Waterman, C. M., and Chadwick, R. S. (2016) Actomyosin Cortical Mechanical Properties in Nonadherent Cells Determined by Atomic Force Microscopy. *Biophys. J.* **110**, 2528–2539

36. Yamaguchi, H., and Condeelis, J. (2007) Regulation of the actin cytoskeleton in cancer cell migration and invasion. *Biochim. Biophys. Acta - Mol. Cell Res.* **1773**, 642–652

37. Nürnberg, A., Kitzing, T., and Grosse, R. (2011) Nucleating actin for invasion. *Nat. Rev. Cancer*. **11**, 177–187

38. Poincloux, R., Collin, O., Lizárraga, F., Romao, M., Debray, M., Piel, M., and Chavrier, P. (2011) Contractility of the cell rear drives invasion of breast tumor cells in 3D Matrigel. *Proc. Natl. Acad. Sci. U. S. A.* **108**, 1943–8

39. Jimenez Valencia, A. M., Wu, P.-H., Yogurtcu, O. N., Rao, P., DiGiacomo, J., Godet, I., He, L., Lee, M.-H., Gilkes, D., Sun, S. X., and Wirtz, D. (2015) Collective cancer cell invasion induced by coordinated contractile stresses. *Oncotarget*. **6**, 43438–51

40. Goley, E. D., and Welch, M. D. (2006) The ARP2/3 complex: an actin nucleator comes of age. *Nat. Rev. Mol. Cell Biol.* **7**, 713–726

41. Suraneni, P., Rubinstein, B., Unruh, J. R., Durnin, M., Hanein, D., and Li, R. (2012) The Arp2/3 complex is required for lamellipodia extension and directional fibroblast cell migration. *J. Cell Biol.* [online] http://jcb.rupress.org/content/197/2/239 (Accessed September 7, 2017)

42. Gardberg, M., Kaipio, K., Lehtinen, L., Mikkonen, P., Heuser, V. D., Talvinen, K., Iljin, K., Kampf, C., Uhlen, M., Grénman, R., Koivisto, M., and Carpén, O. (2013) FHOD1, a Formin Upregulated in Epithelial-Mesenchymal Transition, Participates in Cancer Cell Migration and Invasion. *PLoS One*. **8**, e74923

43. Fritzsche, M., Erlenkämper, C., Moeendarbary, E., Charras, G., and Kruse, K. (2016) Actin kinetics shapes cortical network structure and mechanics. *Sci. Adv.* [online] http://advances.sciencemag.org/content/2/4/e1501337 (Accessed September 7, 2017)

44. Deer, E. L., González-Hernández, J., Coursen, J. D., Shea, J. E., Ngatia, J., Scaife, C. L., Firpo, M. A., and Mulvihill, S. J. (2010) Phenotype and genotype of pancreatic cancer cell lines. *Pancreas*. **39**, 425–35

45. Murrell, M., Oakes, P. W., Lenz, M., and Gardel, M. L. (2015) Forcing cells into shape:

the mechanics of actomyosin contractility. *Nat. Rev. Mol. Cell Biol.* **16**, 486–498

46. Smith, B. A., Tolloczko, B., Martin, J. G., and Grütter, P. (2005) Probing the viscoelastic behavior of cultured airway smooth muscle cells with atomic force microscopy: stiffening induced by contractile agonist. *Biophys. J.* **88**, 2994–3007

47. Kovács, M., Tóth, J., Hetényi, C., Málnási-Csizmadia, A., and Sellers, J. R. (2004) Mechanism of blebbistatin inhibition of myosin II. *J. Biol. Chem.* **279**, 35557–63

48. Duxbury, M. S., Ashley, S. W., and Whang, E. E. (2004) Inhibition of pancreatic adenocarcinoma cellular invasiveness by blebbistatin: a novel myosin II inhibitor. *Biochem. Biophys. Res. Commun.* **313**, 992–7

49. Unbekandt, M., Croft, D. R., Crighton, D., Mezna, M., Mcarthur, D., Mcconnell, P., Schüttelkopf, A. W., Belshaw, S., Pannifer, A., Sime, M., Bower, J., Drysdale, M., and Olson, M. F. (2014) A novel small-molecule MRCK inhibitor blocks cancer cell invasion. *Cell Commun. Signal.* **12**, 1–15

50. Wang, Z.-M., Yang, D.-S., Liu, J., Liu, H.-B., Ye, M., and Zhang, Y.-F. (2016) ROCK inhibitor Y-27632 inhibits the growth, migration, and invasion of Tca8113 and CAL-27 cells in tongue squamous cell carcinoma. *Tumor Biol.* **37**, 3757–3764

51. Rodriguez-Hernandez, I., Cantelli, G., Bruce, F., and Sanz-Moreno, V. (2016) Rho, ROCK and actomyosin contractility in metastasis as drug targets. *F1000Research*. **5**, 783

52. Sen, S., and Kumar, S. (2009) Cell-matrix de-adhesion dynamics reflect contractile mechanics. *Cell. Mol. Bioeng.* **2**, 218–230

53. Koch, T. M., Münster, S., Bonakdar, N., Butler, J. P., and Fabry, B. (2012) 3D Traction Forces in Cancer Cell Invasion. *PLoS One*. **7**, e33476

54. MIERKE, C., ROSEL, D., FABRY, B., and BRABEK, J. (2008) Contractile forces in

tumor cell migration. *Eur. J. Cell Biol.* **87**, 669–676

55. Burridge, K., and Guilluy, C. (2016) Focal adhesions, stress fibers and mechanical tension. *Exp. Cell Res.* **343**, 14–20

56. Even-Ram, S., Doyle, A. D., Conti, M. A., Matsumoto, K., Adelstein, R. S., and Yamada, K. M. (2007) Myosin IIA regulates cell motility and actomyosin–microtubule crosstalk. *Nat. Cell Biol.* **9**, 299–309

57. Ouderkirk, J. L., and Krendel, M. (2014) Non-muscle myosins in tumor progression, cancer cell invasion, and metastasis. *Cytoskeleton*. **71**, 447–463

58. Laevsky, G., and Knecht, D. A. (2003) Cross-linking of actin filaments by myosin II is a major contributor to cortical integrity and cell motility in restrictive environments. *J. Cell Sci.* [online] http://jcs.biologists.org/content/116/18/3761.long (Accessed September 7, 2017)

59. Wolf, K., te Lindert, M., Krause, M., Alexander, S., te Riet, J., Willis, A. L., Hoffman, R. M., Figdor, C. G., Weiss, S. J., and Friedl, P. (2013) Physical limits of cell migration: Control by ECM space and nuclear deformation and tuning by proteolysis and traction force. *J. Cell Biol.* [online] http://jcb.rupress.org/content/201/7/1069 (Accessed September 7, 2017)

60. Revach, O.-Y., Weiner, A., Rechav, K., Sabanay, I., Livne, A., and Geiger, B. (2015) Mechanical interplay between invadopodia and the nucleus in cultured cancer cells. *Sci. Rep.* **5**, 9466

61. Ali, M. H., Pearlstein, D. P., Mathieu, C. E., Schumacker, P. T., Mir, H., and Paul, T. (2004) Mitochondrial requirement for endothelial responses to cyclic strain : implications for mechanotransduction. *Am. J. Physiol. Lung Cell. Mol. Physiol.* **60637**, 486–496

62. Rasheed, Z. A., Matsui, W., and Maitra, A. (2012) *Pathology of pancreatic stroma in PDAC*, Transworld Research Network, [online] http://www.ncbi.nlm.nih.gov/pubmed/22876385 (Accessed September 10, 2017)

63. Shields, M. A., Dangi-Garimella, S., Krantz, S. B., Bentrem, D. J., and Munshi, H. G. (2011) Pancreatic cancer cells respond to type I collagen by inducing snail expression to promote membrane type 1 matrix metalloproteinase-dependent collagen invasion. *J. Biol. Chem.* **286**, 10495–504

64. Zhao, X., Gao, S., Sun, W., Zhang, H., Sun, J., Yang, S., and Hao, J. (2014) Hypoxia-Inducible factor-1 promotes pancreatic ductal adenocarcinoma invasion and metastasis by activating transcription of the actin-Bundling protein fascin. *Cancer Res.* **74**, 2455–2464

65. Nakayama, M., Amano, M., Katsumi, A., Kaneko, T., Kawabata, S., Takefuji, M., and Kaibuchi, K. (2005) Rho-kinase and myosin II activities are required for cell type and environment specific migration. *Genes to Cells*. **10**, 107–117

66. Hetrick, B., Han, M. S., Helgeson, L. A., and Nolen, B. J. (2013) Small molecules CK-666 and CK-869 inhibit actin-related protein 2/3 complex by blocking an activating conformational change. *Chem. Biol.* **20**, 701–12

67. Pruyne, D., Evangelista, M., Yang, C., Bi, E., Zigmond, S., Bretscher, A., and Boone, C. (2002) Role of Formins in Actin Assembly: Nucleation and Barbed-End Association. *Science (80-.).* [online] http://science.sciencemag.org/content/297/5581/612 (Accessed September 7, 2017)

68. Rizvi, S. A., Neidt, E. M., Cui, J., Feiger, Z., Skau, C. T., Gardel, M. L., Kozmin, S. A., and Kovar, D. R. (2009) Identification and Characterization of a Small Molecule Inhibitor of Formin-Mediated Actin Assembly. *Chem. Biol.* **16**, 1158–1168

69. Kim, H.-C., Jo, Y.-J., Kim, N.-H., and Namgoong, S. (2015) Small Molecule Inhibitor of Formin Homology 2 Domains (SMIFH2) Reveals the Roles of the Formin Family of Proteins in Spindle Assembly and Asymmetric Division in Mouse Oocytes. *PLoS One*. **10**, e0123438

70. Barretina, J., Caponigro, G., Stransky, N., Venkatesan, K., Margolin, A. A., Kim, S., Wilson, C. J., Lehár, J., Kryukov, G. V., Sonkin, D., Reddy, A., Liu, M., Murray, L., Berger, M. F., Monahan, J. E., Morais, P., Meltzer, J., Korejwa, A., Jané-Valbuena, J., Mapa, F. A., Thibault, J., Bric-Furlong, E., Raman, P., Shipway, A., Engels, I. H., Cheng, J., Yu, G. K., Yu, J., Aspesi, P., de Silva, M., Jagtap, K., Jones, M. D., Wang, L., Hatton, C., Palescandolo, E., Gupta, S., Mahan, S., Sougnez, C., Onofrio, R. C., Liefeld, T., MacConaill, L., Winckler, W., Reich, M., Li, N., Mesirov, J. P., Gabriel, S. B., Getz, G., Ardlie, K., Chan, V., Myer, V. E., Weber, B. L., Porter, J., Warmuth, M., Finan, P., Harris, J. L., Meyerson, M., Golub, T. R., Morrissey, M. P., Sellers, W. R., Schlegel, R., and Garraway, L. A. (2012) The Cancer Cell Line Encyclopedia enables predictive modelling of anticancer drug sensitivity. *Nature*. **483**, 603–307

71. Bongiorno, T., Kazlow, J., Mezencev, R., Griffiths, S., Olivares-Navarrete, R., McDonald, J. F., Schwartz, Z., Boyan, B. D., McDevitt, T. C., and Sulchek, T. (2014) Mechanical stiffness as an improved single-cell indicator of osteoblastic human mesenchymal stem cell differentiation. *J. Biomech.* **47**, 2197–2204

72. Mierke, C. T. (2015) Physical view on migration modes. *Cell Adh. Migr*. **9**, 367–79

73. Krakhmal, N. V, Zavyalova, M. V, Denisov, E. V, Vtorushin, S. V, and Perelmuter, V. M. (2015) Cancer Invasion: Patterns and Mechanisms. *Acta Naturae*. **7**, 17–28

74. Nyberg, K. D., Hu, K. H., Kleinman, S. H., Khismatullin, D. B., Butte, M. J., and Rowat,

A. C. (2017) Quantitative Deformability Cytometry (q-DC): rapid, calibrated measurements of single cell viscoelastic properties. *Biophys. J.*

75. Wang, N., Tolic-Norrelykke, I. M., Chen, J., Mijailovich, S. M., Butler, J. P., Fredberg, J. J., and Stamenovic, D. (2002) Cell prestress . I . Stiffness and prestress are closely associated in adherent contractile cells. *Am J Physiol Cell Physiol*. **282**, 606–616
76. Kraning-rush, C. M., Califano, J. P., and Reinhart-king, C. A. (2012) Cellular Traction Stresses Increase with Increasing Metastatic Potential. *PLoS One*. **7**, e32572
77. Salbreux, G., Charras, G., and Paluch, E. (2012) Actin cortex mechanics and cellular morphogenesis. *Trends Cell Biol.* **22**, 536–545
78. Xiao, F., Wen, X., and Chiou, P. Y. (2017) Plasmonic micropillars for massively parallel precision cell force measurement. *Proc. IEEE Int. Conf. Micro Electro Mech. Syst.* 10.1109/MEMSYS.2017.7863386

Chapter IV: Label-free prediction of cancer cell invasion by single-cell physical phenotyping

Label-free prediction of cancer cell invasion by single-cell physical phenotyping

Kendra D. Nyberg[1,2], Samuel L. Bruce[1], Angelyn V. Nguyen[1], Clara K. Chan[1], Navjot K. Gill[1], Tae-Hyung Kim[1,3], Erica K. Sloan[3-7], Amy C. Rowat[1,2,6,*]

---

[1] Department of Integrative Biology and Physiology, University of California, Los Angeles, USA.

[2] Department of Bioengineering, University of California, Los Angeles, USA

[3] Semel Institute for Neuroscience and Human Behavior, University of California, Los Angeles, USA.

[4] Drug Discovery Biology Theme, Monash Institute of Pharmaceutical Sciences, Monash University, Parkville, Victoria, Australia.

[5] Division of Cancer Surgery, Peter MacCallum Cancer Centre, Melbourne, Victoria, Australia.

[6] UCLA Jonsson Comprehensive Cancer Center, University of California, Los Angeles, USA.

[7] UCLA AIDS Institute, University of California, Los Angeles, USA.

ABSTRACT

The physical properties of cells, such as cell deformability, are promising label-free biomarkers for cancer diagnosis and prognosis. Here we determine the physical phenotypes that best distinguish human cancer cell lines, and their relationship to cell invasion. We use the high throughput, single-cell microfluidic method, quantitative deformability cytometry (q-DC), to measure six physical phenotypes including elastic modulus, cell fluidity, transit time, creep time, cell size, and maximum strain at rates of 10^2 cells/s. By training a simple k-nearest neighbor machine learning algorithm, we demonstrate that multiparameter analysis of physical phenotypes enhances the accuracy of classifying pancreatic cancer cell lines compared to single parameters alone. We also discover a set of four physical phenotypes that predict invasion; using these four parameters, we generate the physical phenotype model of invasion by training a machine learning algorithm with experimental data from a set of human ovarian cancer (HEYA8) cells that overexpress a panel of tumor suppressor microRNAs. We validate the model using breast and ovarian human cancer cell lines with both genetic and pharmacologic perturbations. Our results reveal that the physical phenotype model correctly predicts the invasion of five cancer cell samples. We also identify a context where our model does not accurately predict invasion, which incites deeper investigation into the role of additional physical phenotypes in cancer cell invasion. Taken together, our results highlight how physical phenotyping of single cells coupled with machine learning provide a complementary biomarker to predict the invasion of cancer cells.

INTRODUCTION

Predicting disease and treatment outcomes based on single cell phenotypes is critical in medicine from cancer diagnosis to stem cell therapies. In clinical oncology and immunology, single cell analysis of protein markers and DNA content using flow cytometry is used for diagnosis, prognosis, and monitoring patient response to therapy[1]. Yet pathological and physiological changes can also manifest as altered cell physical phenotypes, including cell and nuclear size, stiffness, and viscosity, which are convenient, label-free biomarkers. For example, grading of tumor biopsies based on nuclear morphology is widely used for cancer prognosis[2–4]. The mechanical phenotype, or 'mechanotype', of cancer cells also shows promise as a prognostic biomarker, since more invasive cancer cells have altered mechanotype compared to less invasive cells[5–16]. While cell mechanotype impacts the ability of cells to deform through narrow gaps and can thus have consequences for functional behaviors, such as invasion, the relationship between invasion and cell stiffness remains unclear: many studies show that more invasive cancer cells tend to be more compliant than less invasive or benign cells[5–11]; however, there are also contexts where more invasive cells are found to be stiffer[12–16]. These contrasting results motivate deeper investigation into additional physical phenotypes that may collectively be stronger predictors of invasion.

Microfluidic methods are especially valuable for physical phenotyping, as they enable rapid measurements of single cells. One such method is transit-based deformability cytometry, which probes physiologically-relevant deformations of cells through narrow gaps across varying deformation time and length scales[10,17–20]. While transit time T_T is a relative measurement, this parameter can distinguish sets of two to three cancer cell lines[10,19]. However, a population of cells typically exhibits T_T that span several orders of magnitude[21]; together with the inherent variability of T_T measurements, it is thus challenging to robustly compare cell samples, scale up measurements to larger panels of cells, and achieve successful translation to clinical applications. We recently presented the quantitative deformability cytometry (q-DC) method, which uses calibration particles and power law rheology to obtain calibrated single-cell measurements of elastic modulus E and fluidity β[22]. Measuring additional physical phenotypes, such as E and β, could achieve more robust classification of cells using transit-based deformability cytometry.

Studies of cell physical phenotypes using atomic force microscopy (AFM)[23–27], cross-slot deformability cytometry[28], and optofluidic time-stretch microscopy[29] demonstrate that multiple physical phenotypes, such as cell morphology, stiffness, and relaxation time, can enhance the accuracy of cell classification. Multiparameter analysis of physical phenotypes can also result in clinical benefits; biophysical signatures of mesenchymal stromal cells are predictive of their regenerative capability as indicated by *in vivo* ectopic bone formation in mouse models[30]. However, it is unclear which additional parameters can enhance the use of transit-based deformability cytometry to classify cancer cells. More broadly, identifying the physical phenotypes of cancer cells that are predictors of invasion would provide a set of valuable complementary biomarkers for metastatic potential.

Here we investigate the relationship between physical phenotypes and invasion of human cancer cell lines. We perform multiparameter analyses of six physical phenotypes across nineteen cancer cell samples. To measure the physical phenotypes of single cells, we use quantitative deformability cytometry (q-DC) to obtain calibrated measurements of elastic modulus E and cell fluidity β, as well as transit time T_T, creep time T_C, cell size D_{cell}, and maximum strain ϵ_{max}, at rates of 10^2 cells/s[22]. We show that multiparameter analysis of these physical phenotypes can enhance classification of cancer cell lines. From our analysis across well-established pancreatic cancer cell lines as well as ovarian cancer cells that overexpress tumor-suppressor microRNAs, we build the predictive physical phenotyping model for invasion, which we validate using both genetic and pharmacologic perturbations of cancer cells. Our results demonstrate the predictive power of physical phenotypes and machine learning to generate complementary biomarkers for invasion.

MATERIALS AND METHODS

Cell culture. HPDE cells are obtained from Dr. Ming-Sound Tsao (University Health Network-Princess Margaret Hospital, Canada and University of Toronto, Canada). HPDE cells are cultured in Keratinocyte-SFM medium supplemented with prequalified human recombinant Epidermal Growth Factor 1-53, Bovine Pituitary Extract, and 1% penicillin-streptomycin. The human pancreatic ductal adenocarcinoma (PDAC) cell lines (AsPC-1, Hs766T, MIA PaCa-2, and PANC-1) are from the American Type Culture Collection (ATCC). AsPC-1, Hs766T, MIA PaCa-2 and PANC-1 cells are grown in high glucose, L-glutamine without sodium pyruvate DMEM medium with 10% heat-inactivated fetal bovine serum and 1% penicillin-streptomycin. Fetal bovine serum and penicillin-streptomycin are from Gemini BioProducts, West Sacramento, CA. All cell media and additional media supplements are from Thermo Fisher Scientific Inc., Canoga Park, CA. Human ovarian cancer (HEYA8) cells, microRNA mimics, mock, and scrambled (SCR) negative controls are from Dr. Preethi Gunaratne (University of Houston, USA)[31,32]. HEYA8 cells are cultured in RPMI 1640 medium supplemented with 10% fetal bovine serum and 1% of penicillin-streptomycin. Cells are transiently transfected at 24 nM using Lipofectamine 2000 in serum-free OptiMEM medium, followed by the addition of 10% fetal bovine serum after 4 hours in serum-free conditions. All assays are performed 72 hours post transfection. Human ovarian cancer (OVCA433-GFP, OVCA433-Snail) cells are from Dr.

Ruprecht Wiedemeyer (Cedars-Sinai Medical Center, USA)[33]. OVCA433 cells are cultured in DMEM medium with L-Glutamine, Glucose, and Sodium Pyruvate. Medium is supplemented with 10% fetal bovine serum, 1% Anti-anti, and 2.5 µg/ml Plasmocin Prophylactic with 5 µg/ml blasticidin S HCl.

A highly metastatic variant of the MDA-MB-231 cells (MDA-MB-231-HM, gift from Dr. Zhou Ou, Fudan University Shanghai Cancer Center, China)[34] is cultivated in DMEM medium with L-Glutamine, Glucose, and Sodium Pyruvate, supplemented with 10% fetal bovine serum and 1% penicillin-streptomycin. The agonist (isoproterenol) for the β-adrenergic receptor is from Sigma-Aldrich (St. Louis, MO). Cells are treated for 24 hours prior to measurements.

All cells are cultured at 37^{o}C with 5% CO_2. Cell line authentication is performed using short tandem repeat (STR) profiling (Laragen Inc., Culver City, CA, USA and CellBank Australia, Westmead, NSW, Australia). Prior to deformability measurements, 0.01% (v/v) Pluronic F-127 surfactant (Sigma-Aldrich, St. Louis, MO, USA) is added to the cell suspension to reduce cell adhesion to the PDMS walls. While F-127 treatment does not significantly affect E values of suspended cells[22], we observe a significant decrease in cell-to-PDMS adhesion in some cell types such as HPDE cells[21].

Microfluidic chip fabrication. Negative photomasks are designed in AutoCAD (Autodesk, Inc., San Rafael, CA) and printed on chrome by the Nanolab at UCLA. The design of the q-DC devices is described previously[21]. Silicone masters are fabricated using soft photolithography techniques[35]. Polydimethylsiloxane (PDMS) (Sylgard Dow Corning, Midland, MI, USA) with a 10:1 w/w ratio of base and curing agent is poured onto the master wafer and placed under vacuum to degas for 1 hour. To cure the PDMS, the wafer and PDMS mixture is placed in a

65^oC oven for 2 hours. Inlets and outlets are created using a biopsy punch with a 0.75 mm bore size (Sigma-Aldrich, St. Louis, MO, USA). The devices are then bonded to coverglass (#1.5 thickness) by plasma and baked at 80^oC for 5 minutes to facilitate bonding. To ensure consistent device surface properties, q-DC experiments are performed 24 h after plasma treatment[21].

q-DC microfluidic experiment. To measure the physical properties of single cells, we use the q-DC method as previously reported[22]. In brief, q-DC microfluidic devices are mounted onto an inverted microscope (Zeiss Observer, Zeiss, Oberkochen, Germany) that is equipped with a 20×/0.40 NA objective. A constant air pressure (69 kPa) drives cell suspensions to flow through the channels. As cells deform through microfluidic constrictions with 10 µm height and 9 µm width, a CMOS camera (MicroRNAcoEx4, Vision Research, Wayne, NJ, USA) is used to capture brightfield images at rates of 600 to 2000 frames per second. For cell suspensions with a density of 2×10^6 cells/mL that are driven by an applied pressure of 69 kPa (10 psi), single cell measurements can be acquired at rates of 10^2 cells/s. While the timescale of the initial cell deformation into microfluidic constrictions is largely determined by cell deformability (32–34), 0.01% (w/v) pluronic F-127 surfactant (Sigma-Aldrich, St. Louis, MO, USA) is added to the cell media to minimize cell-surface interactions.

Physical property measurements using q-DC. To conduct multiparameter analysis of cell physical properties, the displacement and shape of single cells are tracked using a MATLAB code (Mathworks, Natick, MA, USA; code available online on GitHub)[22]. This enables us to acquire cell size D_{cell}, maximum strain $\epsilon_{\max}$, creep time T_C, and transit time T_T. To extract elastic modulus E and cell fluidity β, the applied stress during cell deformation is measured using agarose calibration particles with well-characterized Young's moduli for the $9 \times 10\ \mu m^2$ and 7 x

10 µm^2 device geometries[22]. By tracking the change in cell strain during deformation and fitting power law rheology to the creep function, we can extract elastic modulus and cell fluidity. The creep function, $J(t)$, is defined as the ratio between the strain and applied stress:

$$J(t) = \frac{\epsilon(t)}{\bar{\sigma}}, \qquad \text{Eq. 1}$$

where $\epsilon(t)$ is the strain and $\bar{\sigma}$ is the time-averaged stress. Here, strain is measured as $\epsilon(t) = \frac{C_o - C(t)}{C_o}$, where C is the circularity, $C(t) = \frac{4\pi A(t)}{P(t)^2}$. We set the initial circularity value as $C_o = 1$, which is the value of a perfect circle, since the cells exhibit a circularity close to 1 prior to deformation through the constrictions. Using least squares residual fitting, we fit the power law model to the creep trajectories of individual cells:

$$J(t) = \frac{\epsilon(t)}{0.032\, P_{applied}}, \qquad \text{Eq. 2}$$

where E is the elastic modulus when $t = \tau$; τ is the characteristic timescale, set to 1 s; and β is the power law exponent, which represents cell fluidity. For purely elastic materials, $\beta = 0$; for purely viscous materials, $\beta = 1$. As elastic modulus E, cell fluidity β, creep time T_C, and transit time T_T depend on cell size, we analyze only cells that have D_{cell} that is the population median ± 1 µm.

Classification using q-DC. To evaluate the power of q-DC parameters to classify cells, we perform supervised machine learning using the k-nearest neighbor (k-NN) algorithm. The k-NN classification algorithm assigns the output class as the most common class of an integer, k, closest neighbors; in this study we use k = 10. The distance is defined as the Euclidian distance between input feature vectors—in our case the sets of qDC predictors. We supply a known set of input data by generating 1000 randomly-sampled subsets with replacement, containing 200 single cells, for each cancer cell line and measuring the medians of the corresponding q-DC parameters for each sample set, such as median cell size and maximum strain. Using the summary statistics dataset in custom Python code, we train classification models based on the k-NN algorithm for sets of q-DC predictors. We execute the training with 5-fold cross validation, which enables us to determine the classification accuracy. Here, the classification accuracy is defined as the percentage of correct predictions on each observation in the validation sets.

Physical phenotype model of invasion using q-DC. The physical phenotype model of invasion is determined by multiple linear regression in MATLAB (Mathworks, Natick, MA, USA). To evaluate linear regression error, we utilize the single-cell q-DC data to train linear regression models using 1000 bootstrapped samples of single-cell physical phenotypes. Each bootstrapped sample generates a linear combination of physical phenotypes to predict invasion and their associated coefficients that minimize residuals. The physical phenotype model is determined by the median coefficient for each parameter. The correlation coefficient between predicted invasion and measured invasion is determined as the average correlation coefficient. Similar to the training analysis, we predict invasion using the physical phenotype model with 1000 bootstrapped samples of the q-DC data of single-cells; this enables us to determine the average predicted invasion.

RESULTS

Multiparameter physical phenotyping by q-DC. To rapidly measure the physical phenotypes of single cells, we use transit-based deformability cytometry; this microfluidic device consists of an array of branching channels[18,20,21,36,37], which lead to micron-scale constrictions. The timescale for cells to transit through the micron-scale constrictions of these channels provides a simple measure of cell deformability (Fig. 4-1A,B): stiffer cells tend to have longer transit times (T_T) compared to more compliant cells[38]. We recently developed quantitative deformability cytometry (q-DC), which enables calibrated single-cell measurements of physical phenotypes including elastic modulus E and fluidity β that are extracted using power law rheology. Using q-DC, we also obtain cell size D_{cell}, from the diameter of the unconstrained cell prior to deformation; maximum strain $\epsilon_{\max}$, based on the minimum circularity that occurs as the cell deforms through the constriction; and creep time T_C, which is the time required for a cell to reach maximum strain (Fig 4-1A). While q-DC enables measurements of physical phenotypes in addition to T_T, it is not clear how this added information benefits cell classification and prediction of invasion.

Pairwise correlation analysis of q-DC parameters. To assess the value of multiple biophysical parameters for classification of different cell types, we use q-DC to measure physical phenotypes of human pancreatic ductal adenocarcinoma (PDAC) cell lines that are derived from primary tumors (PANC-1 and MIA PaCa-2), and secondary sites (AsPC-1 and Hs766T), as well as a nontransformed human ductal pancreatic epithelial (HPDE) control cell line. These cell lines exhibit distinct differences in invasion[12], and therefore provide a model system for testing q-DC classification of cells.

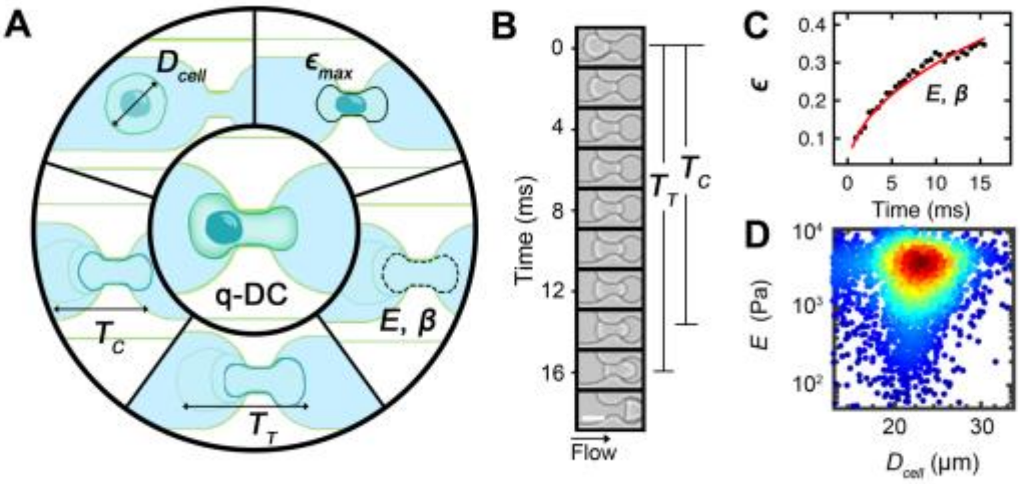

Fig 4-1. Overview of cell physical phenotyping by quantitative deformability cytometry (q-DC). (*A*) Overview of physical phenotypes measured by q-DC: elastic modulus *E*, cell fluidity *β*, transit time T_T, creep time T_C, cell size D_{cell}, and maximum strain ϵ_{max}. (*B*) A representative cell deforming through a microfluidic channel of the q-DC device. Creep time T_C is the time required for a cell to reach maximum strain ϵ_{max}; transit time T_T is the time required for the cell to transit through the constriction. Scale bar, 20 µm. (*C*) Black dots represent the strain of the single cell shown in panel *B* as a function of time. Red solid line represents power law fit to single-cell strain trajectory over the creep timescale, T_C. Using power law rheology, we extract elastic modulus, *E*, and fluidity exponent, *β*. (*D*) Representative scatter plot of *E* and D_{cell} for human pancreatic ductal epithelial (HPDE) cells. Each dot represents a single cell and color denotes number density. Shown here are a total of N = 3231 cells.

To identify which physical phenotypes provide unique information and which ones are statistically redundant for classifying populations of single cells, we first evaluate the correlation strength between pairs of the six q-DC outputs, E, β, T_T, T_C, D_{cell}, and ϵ_{max} (Fig. 4-2A, S. Table. 4-1). Spearman's rank correlation coefficients of -1 and +1 reflect pairs of parameters that are highly correlated and statistically dependent on each other. By contrast, correlation coefficients with a low absolute value indicate pairs of parameters that are weakly correlated with each other;

each parameter from a weakly correlated pair will more likely provide unique information, as they are more statistically independent from each other.

Analysis of the Spearman's correlation coefficients reveals that T_T and T_c are highly correlated ($r = 0.94$; $p \ll 0.001$) (Fig. 4-2A, S. Table. 1); this is expected as the first stage of cell transit through a pore requires cell creep. We also find that β and E are strongly correlated ($r = -0.88$; $p \ll 0.001$); this scaling of E and β is consistent with the behavior of soft glassy materials[17,39]. All other pairwise comparisons between parameters, such as D_{cell} to ϵ_{max}, T_T, E, are weakly correlated with $-0.14 < r < 0.41$ (S. Table 4-1), suggesting that combinations of these parameters could provide unique information for characterizing cell lines.

Multiparameter analysis for classification of pancreatic cells. To assess the value of q-DC data sets in classifying PDAC cell lines, we use the simple yet powerful k-nearest neighbors (k-NN) algorithm to classify cell lines based on physical phenotypes. In the k-NN method, training data establishes a multidimensional feature space, where q-DC parameters define each dimension; cells are then classified based on the identity of their k nearest neighbors in the pre-established feature space. To evaluate how the number of predictors and combinations thereof affect classification accuracy, we first assess single physical phenotypes. We find that single parameters alone offer low classification accuracy of cell lines: T_T yields 65% accuracy in predicting the correct cell line from our panel of PDAC cell lines, E yields 59% accuracy, and D_{cell} gives 52% (Fig. 4-2B).

The inclusion of additional physical phenotypes can significantly enhance classification accuracy: $\{E, T_T\}$ provide a model accuracy of 87% and with $\{T_T, D_{cell}\}$, the model accuracy increases to 91% (Fig. 4-2B, S. Fig. 1). Other combinations of two parameters yield accuracies ranging from 69% to 89% (S. Fig. 4-1). Including an additional third parameter further improves accuracy, but with smaller gains: both $\{E, T_T, D_{cell}\}$ and $\{E, \epsilon_{max}, D_{cell}\}$ result in 94% accuracy. The highest accuracy of 96% can be obtained using four parameters $\{E, T_T, D_{cell}, \epsilon_{max}\}$ (Fig. 4-2B). Surprisingly, we find that using additional q-DC parameters does not improve classification accuracy, which ranges from 92% to 96% when using five and six physical phenotypes; this highlights how highly correlated parameters, such as T_T and T_C, do not add unique value to cell classification accuracy. Therefore, $\{E, T_T, D_{cell}, \epsilon_{max}\}$ constitute the 'reduced set' of parameters as they provide the highest classification accuracy with the least amount of parameters.

Since transit time T_T is a common metric for mechanotype that is obtained by transit-based deformability cytometry[20], we next evaluate the benefit of q-DC parameters by comparing the performance of the k-NN algorithm using the reduced set of parameters to T_T alone (Fig. 4-2C,D). For the k-NN algorithm using T_T as a single predictor, we find the algorithm performs poorly: the true positive rate for each cell line ranges from 0.33 to 0.86 (Fig. 4-2C). For example, the true positive rate for PANC-1 cells is 0.33, indicating that only 33% of PANC-1 samples are correctly identified as PANC-1 cells, 41% are incorrectly identified as HPDE cells, and 26% as AsPC-1 cells (Fig. 4-2C). When $\{T_T\}$ is used, the true positive rate averaged across all cell lines is 0.65 and the false positive rate is 0.35. By contrast, the reduced set of q-DC parameters $\{E, T_T, D_{cell}, \epsilon_{max}\}$ significantly improves the average true positive rate to 0.96. For example, the true positive rate for PANC-1 cells is 1.0, where 100% of PANC-1 samples are correctly identified. Additionally, the true positive rate for Hs766T is 0.94, where 94% of Hs766T samples are correctly identified, while 6% are identified as MIA PaCa-2 (Fig. 4-2D). We also observe the reduced set $\{E, T_T, D_{cell}, \epsilon_{max}\}$ decreases the false positive rate, which ranges from 0 to 0.06

(average = 0.04) (Fig. 4-2D). Taken together, these findings indicate that q-DC predictors increase the accuracy for classifying PDAC cell lines compared to T_T alone.

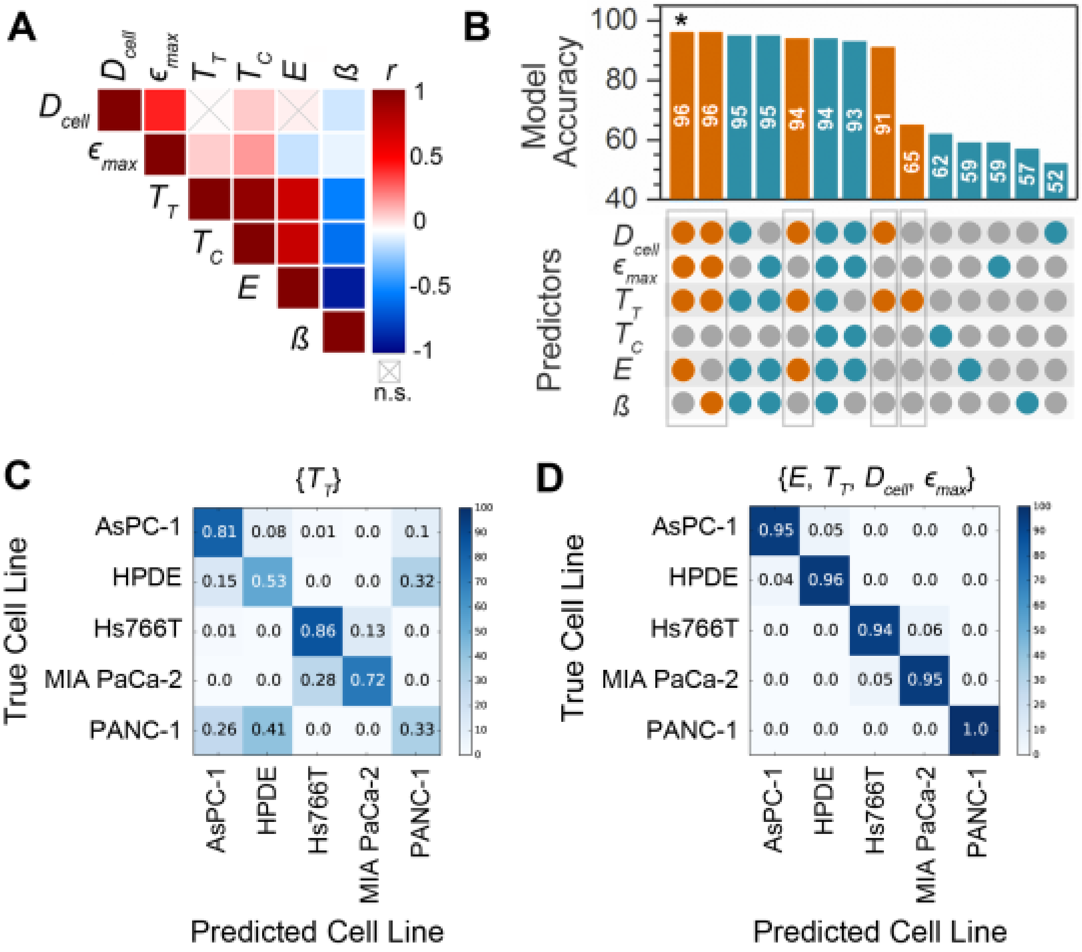

Fig. 4-2. Predictive power of q-DC outputs for cell classification. (*A*) Spearman's rank correlation coefficients for pairs of q-DC outputs: elastic modulus E, cell fluidity β, transit time T_T, creep time T_C, cell size D_{cell}, and maximum strain ϵ_{max}. Color represents the magnitude of the correlation coefficient, r, as detailed in S. Table. 1. Gray 'X' denotes not statistically significant (n.s.). (*B*) Accuracy of k-nearest neighbor machine learning algorithm for classifying human pancreatic cell lines. Each bar represents the accuracy of models built with varying combinations of q-DC predictors as indicated by the colored dots; grey dots represent excluded predictors. Orange bars and dots represent the highest accuracy that can be achieved with a set of one, two, three, and four physical phenotypes. Turquoise bars and dots show

accuracy obtained by all other combinations of physical phenotypes. Asterisk shows the reduced set of predictors that provides the greatest accuracy with the least number of parameters. White numbers show the accuracy, which is calculated as the percentage of data subsets that are correctly identified as one of the five pancreatic cell lines. S. Fig. 1 illustrates the accuracy of models using additional combinations of q-DC predictors. (C-D) Confusion matrices show the performance of the k-NN algorithm for (C) transit time T_T, and (D) reduced set of q-DC predictors: elastic modulus E, transit time T_T, cell size D_{cell}, and maximum strain ϵ_{max}. Rows represent the true cell line; columns represent the predicted cell line. Color scale denotes the proportion of cells predicted as each cell type.

Relationship of physical phenotypes to cancer cell invasion. Defining how cancer cell physical phenotypes relate to functional behaviors, such as invasion, could provide valuable biomarkers that have physiologically relevant predictive power. Invasion is fundamentally a physical process, whereby cells deform and move through narrow gaps of the extracellular matrix. The invasion of cancer cells is associated with physical phenotypes such as cell stiffness or elastic modulus: while in some contexts more invasive cells are more compliant[5–11], there are other cases where more invasive cells are stiffer[12–16]. Other physical phenotypes, such as cell size and deformation timescale can also determine the ability of cells to deform through narrow gaps[21]. While correlations between individual physical phenotypes and invasion have been investigated[12,32,40], it is not known how these phenotypes could collectively provide an improved biomarker for invasion.

To determine the relationship between the reduced set of physical phenotypes $\{E, T_T, D_{cell}, \epsilon_{max}\}$ and cancer cell invasion (Fig. 4-3A), we first evaluate the correlation between invasion and single physical phenotypes. Across the panel of PDAC cell lines, we find that individual parameters from the reduced set have poor to moderate correlations with invasion as measured using a 3D scratch wound invasion assay[12,32]: Pearson's correlation yields R^2 that range from $R_{D\text{-}}$

$_{\text{Inv}}^2 = 0.05 \pm 0.001$ to $R_{\text{E-Inv}}^2 = 0.45 \pm 0.006$ (Fig. 4-3B). We find the strongest correlation of a single parameter with invasion for E ($R_{\text{E-Inv}}^2 = 0.45 \pm 0.006$), whereby cells that are more invasive tend to have lower E (Fig. 4-3B). This trend of more invasive cells being more compliant is consistent with previous reports in breast and ovarian cancer cells[5–11]. However, the inverse relationship between invasion and E does not hold across all PDAC cell lines as MIA PaCa-2 cells exhibit the lowest elastic modulus yet reduced invasion compared to Hs766T and PANC-1 cells (Fig. 4-3B).

We also physical phenotype seven ovarian cancer cell samples that overexpress distinct tumor-suppressor microRNAs; higher levels of expression of these microRNAs are associated with improved patient survival, as identified through Cancer Genome Atlas (TCGA) data[31]. We previously found that these tumor suppressor microRNAs decrease cell invasion[31,32] and tend to increase cell transit time[32]. Physical phenotyping by q-DC reveals that individual phenotypes of microRNA-overexpressing cells also exhibit only moderate correlations to invasion (Fig. 4-3B). While we find that higher E and T_T are associated with decreased invasion across both established pancreatic cancer cell lines and ovarian cancer cells with manipulated microRNA levels, we find opposite trends for D_{cell} and ϵ_{max} (Fig. 4-3B); these discrepancies further substantiate the low predictive power of individual physical phenotypes. As single physical phenotypes are not sufficient to predict invasion, we next investigate if multiparameter analysis using the reduced set of four physical phenotypes can collectively predict cancer invasion.

To develop a model that can predict cell invasion on the basis of physical phenotypes, we train a multiple linear regression model using $\{E, T_T, D_{cell}, \epsilon_{max}\}$ and invasion data. While we use data from numerous cell samples, linear regression can be susceptible to overfitting when the number of fitting parameters approaches the number of data points. Therefore, we account for the number of predictors in the strength of correlation between the measured and predicted invasion using the adjusted-R^2 (R^2_{adj}),

$$R_{adj}^2 = 1 - [\frac{(1-R^2)(n-1)}{n-m-1}], \qquad \text{Eq. 3}$$

where n is the number of observations and m is the number of predictors. For the PDAC cell lines, an R^2_{adj} value does not exist, as there are four fitting parameters in the reduced set and only five cell lines. Reducing the number of predictors only yields R^2_{adj} that are similar to correlations between single parameters and invasion (S. Fig. 4-2). However, building the linear regression model using invasion and physical phenotype data $\{E, T_T, D_{cell}, \epsilon_{max}\}$ from seven ovarian cancer cell samples that overexpress distinct microRNAs results in invasion values that are highly correlated with experimental observations, as indicated by the high $R^2_{adj} = 1.00 \pm 0.002$ (Fig. 4-3D); we call this multiple linear regression model built with the reduced set the 'physical phenotype model for invasion', as it demonstrates robustness to predict invasion. We also train models with smaller sets of predictors; however, we find that reduced set of physical phenotypes ($E, T_T, D_{cell}, \epsilon_{max}$) yields the highest R_{adj}^2 value, and thus generates the strongest predictive model with the smallest number of parameters (Fig. 4-3D).

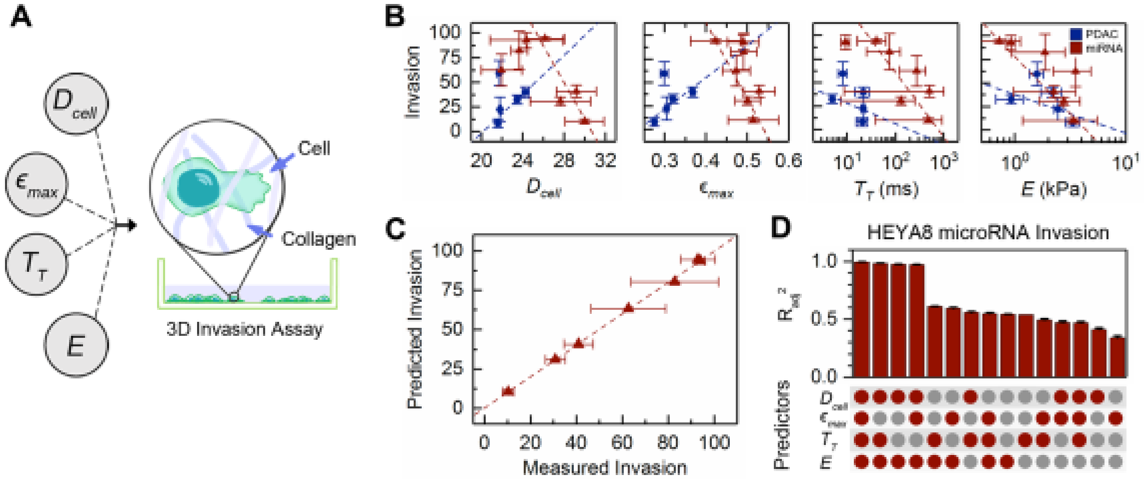

Fig. 4-3. **Relationship of q-DC parameters and invasion across cancer cell types**. (A) Schematic illustration the reduced set of physical phenotypes, which we use to predict cell invasion, elastic modulus E, transit time T_T, cell size D_{cell}, and maximum strain ϵ_{max}, as measured using 3D invasion assay. (B) Plots showing invasion versus single physical phenotypes for pancreatic adenocarcinoma (PDAC) cell lines (blue circles) and ovarian cancer (HEYA8) cells that overexpress a panel of tumor suppressor microRNAs (red triangles). Each data point represents the median value for a cell sample. Error bars represent standard deviation. Dashed lines show best linear fits. (C) Correlation between measured and predicted invasion using the physical phenotype model for invasion. Dashed lines show best linear fit for the microRNA-overexpressing cells. Data points represent the average value for a cell sample. Error bars represent standard deviation. (D) The strength of correlations between measured and predicted invasion from linear regression models built with combinations of physical phenotypes for microRNA-overexpressing ovarian cancer cells. Colored circles illustrate the set of predictors used in the model. Bars represent adjusted-R^2 (R_{adj}^2) values, which reflect the average strength of the correlation, while accounting for the number of fitting parameters to data points. Error bars represent standard deviation.

Predicting invasion using label-free physical phenotypes. To validate the physical phenotyping model for invasion, we measure physical phenotypes of seven additional cancer cell samples, and determine how accurately we can predict their invasion. We first use q-DC to physical phenotype three breast cancer cell lines, MDA-MB-231, MDA-MB-468, and MCF-7 (Fig 4-4A). These cell lines are well characterized to have varying invasive potentials, from highest to lowest: MDA-MB-231 > MDA-MB-468 > MCF-7[41–45]. Other key characteristics of progression are also described for these cell lines, including the propensity to form cell colonies (MDA-MB-231 > MDA-MB-468 > MCF-7)[45]. By physical phenotyping using q-DC, we find that MDA-MB-231 cells have decreased E compared to both MDA-MB-468 and MCF-7 cells ($E_{\text{MDA-MB-231}} = 1.2 \pm 0.3$ kPa < $E_{\text{MCF-7}} = 2.0 \pm 0.2$ kPa < $E_{\text{MDA-MB-468}} = 2.7 \pm 0.3$ kPa). Compared to the ranking of invasion of these cells types, we find a weak correlation between E and invasion, which is further quantified by Spearman's correlation coefficient (r = 0.5); these findings support that E alone is not sufficient to predict invasion. We find that transit times follow the same ranking as E, whereby $T_{T\text{ - MDA-MB-231}} = 15 \pm 3$ ms < $T_{T\text{ - MCF-7}} = 25 \pm 5$ ms < $T_{T\text{ – MDA-MB-468}} = 57 \pm 27$ ms (Fig. 4-4A). Thus, neither E nor T_T is sufficient to predict invasion. However, we discover that the physical phenotyping model for invasion correctly ranks the invasion of these breast cancer cell lines, MDA-MB-231 > MDA-MB-468 > MCF-7 (Fig. 4-4D). These results further substantiate the power of multiparameter analysis to predict invasion based on label-free physical phenotyping of single cancer cells.

To further validate the physical phenotyping model for invasion, we predict the invasion of ovarian cancer (OVCA433) cells that have been genetically manipulated to generate a pair of epithelial- and mesenchymal-like cell lines. Cancer cells with overexpression of Snail[33] (OVCA433-Snail), a key transcription factor in epithelial-to-mesenchymal transition (EMT)[46], are mesenchymal-like and exhibit increased invasion[46]. By contrast, the control cells (OVCA433-GFP) are epithelial-type. Using q-DC to physical phenotype this pair of cell lines, we find that OVCA433-Snail cells have a reduced E compared to the OVCA433-GFP control cells ($E_{\text{OVCA-GFP}} = 1.8 \pm 0.1$ kPa; $E_{\text{OVCA-Snail}} = 1.0 \pm 0.7$ kPa; $p << 0.001$) (Fig 4-4B). We also observe that OVCA433-Snail cells exhibit shorter transit times than OVCA433-GFP ($T_{T\text{ - OVCA-GFP}} = 22 \pm 2.8$ ms; $T_{T\text{ – OVCA-Snail}} = 16 \pm 1.2$ ms, $p << 0.001$), consistent with the decreased stiffness of the mesenchymal-type OVCA433-Snail cells (Fig. 4-4B). Using q-DC outputs, we demonstrate that the physical phenotype model for invasion has the power to predict the increased invasion of the OVCA433-Snail cells compared to the control OVCA433-GFP cells (Fig. 4-4B); these results also demonstrate that physical phenotypes measured by q-DC are consistent with other hallmark characteristics of EMT, such as the increased vimentin to E-cadherin ratio[47] and ability to form cell colonies[48], which are commonly used to define mesenchymal-type cells.

We next assess how increased cell invasion that is caused by pharmacologic manipulation can be predicted by the physical phenotype model of invasion. We previously showed that cancer cells treated with the β-adrenergic agonist, isoproterenol, have increased invasion *in vitro*[13]. Activation of β-adrenergic signaling also promotes metastasis in clinically-relevant orthotopic mouse models of breast cancer[34,49]. Following treatment of highly metastatic human breast cancer (MDA-MB-231-HM) cells with isoproterenol, we find that E increases from $E_{\mathrm{Control}} = 0.9 \pm 0.4$ kPa to $E_{\mathrm{ISO}} = 4.0 \pm 0.6$ kPa ($p = 0.001$) (Fig. 4-4C). Similarly, T_T increases from $T_{T\text{ - Control}} = 18 \pm 4.2$ ms to $T_{T\text{ - ISO}} = 81 \pm 31$ ms ($p << 0.001$)[13] (Fig. 4-4C). While we measure statistically significant differences in cell physical phenotypes with this pharmacologic perturbation, the physical phenotyping model for invasion does not accurately predict the effects of isoproterenol on cancer cell invasion (Fig 4-4F). The inability of the physical phenotyping model to predict the increased invasion caused by this pharmacologic manipulation suggests that there is a fundamentally different relationship between the physical phenotypes of cells with activation of β-adrenergic signaling and invasion compared to the other sets of cancer cells that we investigate here.

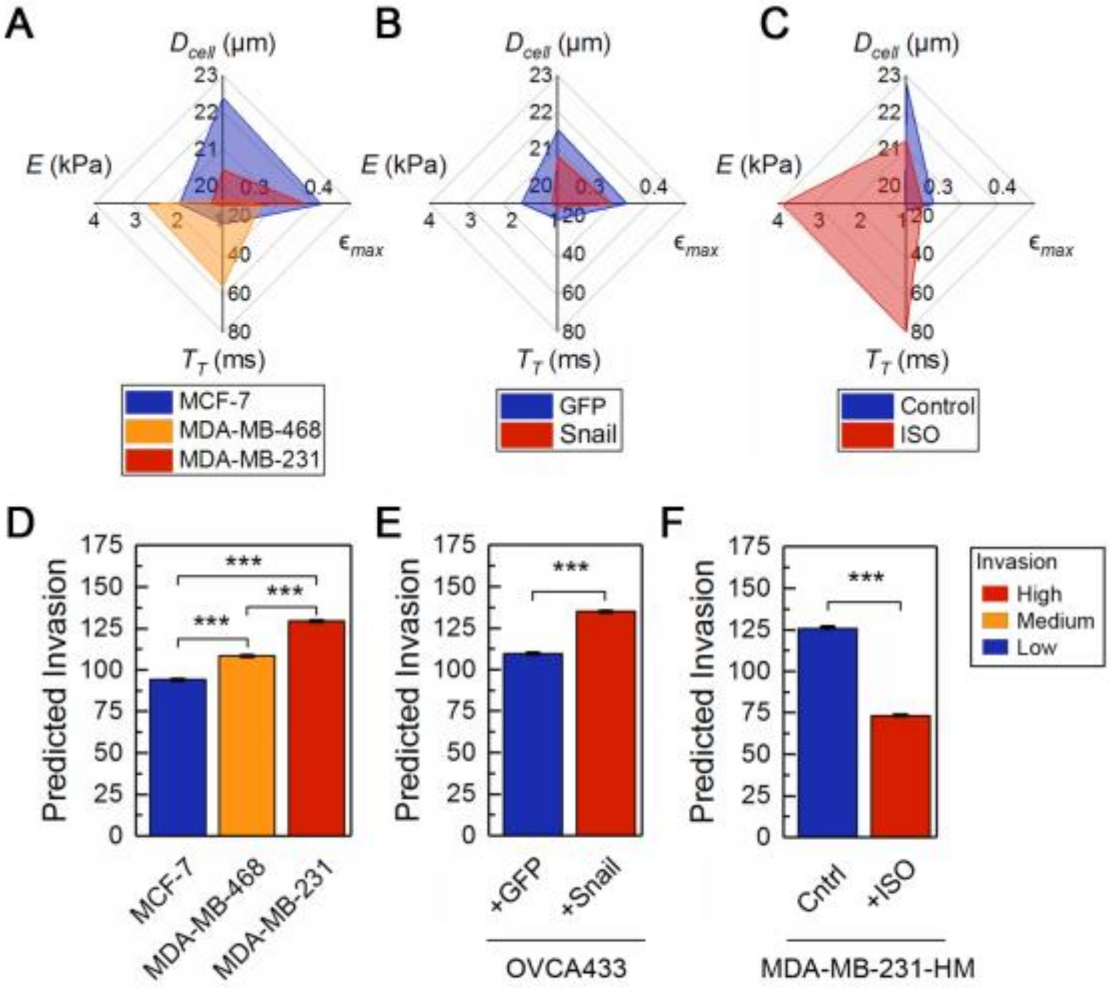

Fig. 4-4. **Predicting invasion by multiparameter physical phenotyping**. (A-C) The four key physical phenotypes that comprise the reduced set for: (A) breast cancer cells, MCF-7, MDA-MB-468, and MDA-MB-231; (B) ovarian cancer cells, OVCA433-GFP control, and OVCA433 that overexpresses Snail (OVCA433-Snail), a key transcription factor in epithelial-to-mesenchymal transition (EMT); (C) Highly metastatic human breast cancer (MDA-MB-231-HM) cells with activation of β-adrenergic signaling by treatment with 100 nM isoproterenol (+ISO) or vehicle (Control) for 24 h. N > 400. (D-F) Average predicted invasion as determined by the physical phenotyping model for invasion. Error bars represent the standard deviation. Colors represent previously determined invasive potentials, as described in literature[13,42–45].

DISCUSSION

Our results across 18 distinct samples of ovarian, breast, and pancreatic cancer cells show that cell stiffness alone, as indicated by E or T_T, is not sufficient to predict invasion. Using label-free, multiparameter physical phenotyping of single cells, we develop the physical phenotyping model that can predict invasion using four parameters—elastic modulus E, transit time T_T, maximum strain ϵ_{max}, and cell size D_{cell}—which can be rapidly measured using q-DC. We demonstrate the model's predictive power across cell lines, which have inherent differences in invasive potential, as well as for cells that have increased invasive potential caused by genetic manipulations.

Physical phenotypes as indicators of invasion. While cell classification is the basis for malignant diagnosis, the ability to rapidly physical phenotype populations of single cells, and predict their invasive ability, would greatly reduce the time required to measure cell invasion, which is typically hours to days. Using q-DC and machine learning, we find that the strongest indicators of invasion for microRNA-overexpressing ovarian cancer cells are E, T_T, ϵ_{max}, and D_{cell}.

Elastic modulus. E is an essential indicator of invasion in the physical phenotype model. Our investigation of physical phenotypes across 18 cell samples, including established cell lines and a range of genetic and pharmacologic perturbations, provide the opportunity to examine how broadly the relationship between cell stiffness and invasion can be generalized. Interestingly, while we find that E tends to decrease for cells that are more invasive, we also identify contexts where more invasive cells are stiffer. For example, across pancreatic cancer cell lines, we find that more invasive cells are more compliant. Yet, we also find that PANC-1 and Hs766T cells, which are more invasive, are stiffer compared to MIA PaCa-2 cells. We also observe that while many of the microRNAs cause ovarian cancer (HEYA8) cells to become stiffer and less invasive, overexpression of microRNA 509-5p causes cells to be stiffer and *more* invasive. There are additional examples of more invasive cells being stiffer in the breast cancer panel, where MDA-MB-468 are stiffer, yet more invasive than MCF-7 cells. Treatment of MDA-MB-231 cells with isoproterenol also causes cells to be stiffer and more invasive. These and other cases of more invasive cells that are stiffer[12–16], highlight how the concept that elastic modulus is inversely correlated with invasion is oversimplified.

Transit time. While transit time T_T is commonly used to distinguish cancer cell types[20], this parameter alone is not a strong indicator of invasion. We find moderate to poor correlations between T_T and invasion across well-characterized cell lines and microRNA-overexpressing cells. The emergence of T_T as an indicator of invasion in the physical phenotyping model suggests that the ability of cells to continuously deform may be important in invasion. While E reflects the ability of a cell to resist initial deformation, and thus dominates viscoelastic response on short ~ms timescales[21], transit time captures the ability of a cell to deform through the entire constriction. We showed previously that T_T depends on both elastic and viscous properties[21]; indeed, invasion occurs over hours to days[38], where viscous contributions may be more relevant.

Size. We also find that cell size D_{cell} strengthens the accuracy of the physical phenotype model to predict invasion. We and others previously determined that cell size is inversely correlated with invasion potential[9,32], which may reflect how smaller cells can more readily invade through a matrix. Cell size also determines the probability of cells to occlude narrow capillaries or pores[50,51], and thus may be implicated in lodging of cells in metastatic target sites, such as the narrow capillaries of the pulmonary beds of the lung[52]. The effects of cell size may also reflect contributions of the cell nucleus to q-DC measurements: nuclear size scales with cell size[12], and the nucleus tends to be stiffer than the surrounding cytoplasm[11]. Moreover, increased nuclear-to-cytoplasmic volume is a hallmark of malignant cells with diagnostic value[2,53,54]. Morphological parameters, such as eccentricity and circularity, are also identified as strong predictors of cancer cell types[25].

Effects of measurement techniques on multiparameter physical phenotyping. Since different methods for physical phenotyping probe cells over different time and length scales, it is not clear how broadly the predictors of invasion that we have identified using q-DC may be extended to other methods. Despite differences in the deformation depth and timescale between q-DC and a conventional mechanotyping method, such as AFM, we observe a similar range of elastic modulus values obtained using q-DC and AFM of cells that are cultured under the same conditions[12]. However, we find the ranking of elastic moduli determined by q-DC and AFM is not consistent: by q-DC from stiffest to most compliant, AsPC-1 > HPDE > PANC-1 > Hs766T > MIA PaCa-2, and by AFM, Hs766T ~ HPDE > PANC-1 > MIA PaCa-2. One notable difference is the Hs766T cells: they are the stiffest PDAC cell line measured by AFM and second most compliant cell line by q-DC, despite having an elastic modulus of a similar order of magnitude (3.0 ± 2.0 kPa by AFM and 1.6 ± 0.2 kPa by q-DC). This difference between cell mechanotype measured by these two methods may be attributed to the difference in cell measurement state: microfluidic methods such as q-DC probe cells in a suspended state, whereas AFM measures adhered cells. When cells lift off from the substrate into a suspended state, they undergo dramatic cytoskeletal rearrangements and exhibit altered distributions of F-actin[55]. By contrast, cells that are attached to a substrate also generate intracellular tension, or ‘prestress’[56], which can contribute to cell stiffness measurements[57,58]. Therefore, the stiffness of the Hs766T cells measured by AFM may reflect their increased contractility and/or stress fiber formation compared to when they are in suspension. Since the stiffness of adhered cells depends on myosin II activity[59–62] and traction stresses scale with cell metastatic potential[63], mechanotyping of adhered cells may thus provide an additional, complementary physical indicator of cell invasion. This example of cell mechanotype differences in adhered and suspended states highlights why measuring the mechanical properties of cells using complementary methods could provide valuable information about the passive and active contributions to cell deformability. Measurements of adhered and suspended cells may also provide deeper insight into the possible functional significance of cell mechanotype. While cell deformations are required for adhered cells during invasion, extravasation, and intravasation [52,64], cells in a suspended state deform during circulation through the blood and lymphatic vasculature [52,64].

Benefits of multiparameter analysis for predicting cell invasion. Cell physical phenotypes are emerging as valuable, complementary biomarkers for cell classification and clinical benefit(8,22,23,24). While enhanced predictive power can be achieved with additional parameters obtained by q-DC, extra computation is required to extract parameters such as elastic modulus E, cell fluidity β, creep time T_C, and maximum strain ϵ_{max}[22]. The tradeoff between classification accuracy and computational expense will ultimately depend on the specific application. For example, certain cancer cell populations can be distinguished using measurements of T_T and D_{cell}, which rely on simple image analysis[10,19–21,36,38]. With greater computational investment, including tracking the time-dependent changes in cell shape during deformation and fitting single-cell creep trajectories to power law rheology models, additional parameters such as ϵ_{max} and E can be determined[22]. However, such enhanced resolution may not be essential for specific applications. For example, the invasion of the epithelial-type OVCA433-GFP cells versus the mesenchymal-type OVCA433-Snail cells is accurately ranked by E alone

(Fig 4-4E). In future applications, more advanced machine learning algorithms could bypass the additional image analysis required for q-DC; for example, neural network algorithms can be trained using images with minimal processing, and thus do not require the additional computational steps to extract physical phenotypes.

Additional biophysical markers may also broaden the application of the physical phenotype model to contexts where the model does not accurately predict invasion, such as in the case of pharmacologic perturbations. Specifically, activation of β-adrenergic signaling alters single-cell physical phenotypes and invasion, but in a way that is not consistent with the other cell samples, including both cell lines and genetically-modified cells, that we investigate here. Further studies of how β-adrenergic signaling alters cell physical phenotypes should deepen our understanding of the relationship between invasion and physical phenotypes and facilitate the discovery of additional biomarkers, such as contractility, for invasion. Invasion is a complex and highly dynamic process requiring deformation through micron-scale pores[52,65], actin protrusion formation[66], generation of traction forces[63], and secretion of proteases[67–69]. For example, the increased stiffness of cells with activation of β-adrenergic signaling requires myosin II activity[13]; myosin II is also required for actomyosin contractility, which increases cell stiffness in adhered states[59–62] and generates forces required for cells to invade through 3D matrices[70,71].

Navigating the physical fitness landscape of invasion. While the physical phenotype model for invasion relies on the reduced set of parameters—elastic modulus E, transit time T_T, maximum strain ϵ_{max}, and cell size D_{cell}—it is intriguing to speculate if these physical phenotypes reflect a particular strategy for optimizing cell invasion. We observe that more invasive cells tend to have lower elastic modulus and smaller cell size (Fig 4-3B). However, the predictive power of the physical phenotype model for is based on the multiparameter physical signature of invasive cells.

Future studies to better elucidate the interplay between physical phenotypes in the invasion fitness landscape will deepen our understanding of selective advantages that may be acquired by cancer cells to enhance their invasion.

Our findings that the physical phenotype model for invasion cannot predict the increased invasion of cancer cells with β-adrenergic activation may imply that different physical signatures reflect different strategies for cancer cell invasion. Deeper investigation of contexts where invasion cannot be predicted by the physical phenotype model for invasion may reveal another regime that is described by a different set of phenotypes that can predict invasion. Identifying additional complementary biomarkers could generate a more inclusive—even universal—model to predict invasion across varied contexts.

While we focus here on using physical phenotypes as indicators of invasion, the rapid, calibrated measurements of q-DC have exciting potential to also provide mechanistic insights into the invasive behavior of cancer cells. Since proteins of the mechanome and contractome, which regulate cancer cell physical phenotypes, are also essential in invasion[32], determining the molecular origins of cell physical phenotypes should reveal novel mediators and pathways that can be targeted to stop cancer cell invasion.

CONCLUSION

The q-DC method for single-cell physical phenotyping coupled with machine learning algorithms provides a crucial step towards enhanced classification of cancer cell types. Our findings also link cancer cell physical phenotypes with functional behaviors such as invasion, establishing a framework for predicting invasion based on label-free biomarkers that can be rapidly measured. The ability of q-DC to enable calibrated, multiparameter cell physical phenotyping to classify cell types and predict cellular behaviors is valuable for biomedical applications, and should offer unprecedented insight into heterogeneous populations of cells that include subpopulations of drug-resistant cancer cells to undifferentiated stem cells.

ACKNOWLEDGEMENTS

We are grateful to the National Science Foundation (CAREER DBI-1254185 to ACR), Broad Stem Cell Research Center, UCLA Life Sciences Innovation Fund Award, and the Farber Family Foundation for financial support. We thank Dr. Timothy Donahue (University of California, Los Angeles, USA) for the pancreatic ductal adenocarcinoma cell lines; Dr. Ming-Sound Tsao (University Health Network-Princess Margaret Hospital and University of Toronto, Canada) for the non-transformed human pancreatic ductal epithelial (HPDE) cell line; Dr. Preethi Gunaratne (University of Houston, USA) for the tumor-supressor microRNAs; and Dr. Ruprecht Wiedemeyer and Dr. Barbie Taylor-Harding (Cedars-Sinai Medical Center, USA) for the OVCA433-GFP and Snail-expressing cell lines. We are also grateful to Massoud Karimzadeh contributed to insightful discussions and to the staff at the Integrated Systems Nanofabrication Cleanroom at the California NanoSystems Institute for supporting the fabrication of the microfluidic devices.

SUPPLEMENTAL INFORMATION

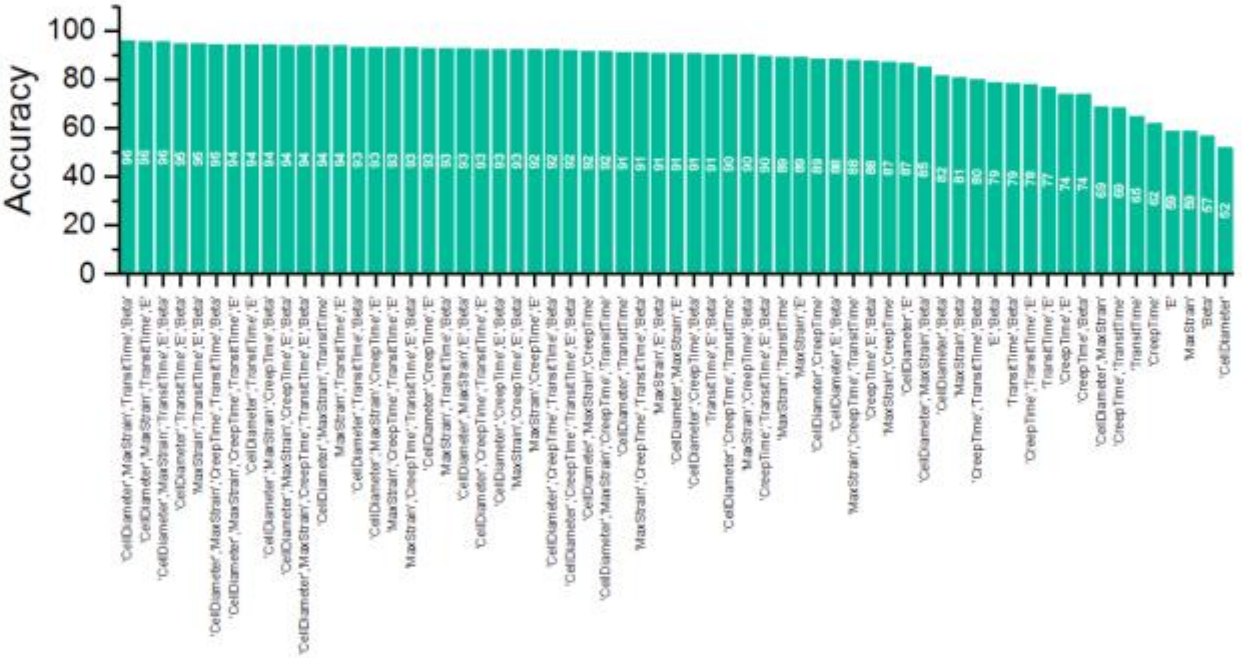

S. Fig. 4-1 Sets of q-DC predictors alter the accuracy of cell classification algorithms. Bars show the accuracy of classification algorithms that are built using varying sets of q-DC predictors; white text denotes the numeric values of accuracy.

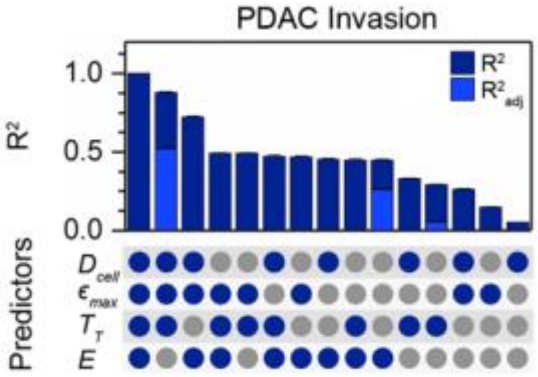

S. Fig. 4-2 Correlation between experimental and predicted invasion of PDAC cells using physical phenotyping. R^2 and adjusted R^2 (R_{adj}^2) values of physical phenotyping models of invasion, which use varying sets of parameters. Blue bars represent R^2 values; navy blue bars represent R_{adj}^2 values, which reflect goodness of fit, while accounting for the number of parameters to data points. Colored circles illustrate the set of predictors.

S. Table 4-1. Pair-wise Spearman's rank correlation coefficients. Matrix of correlation coefficients for pairs of q-DC variables: cell diameter D_{cell}, maximum strain ϵ_{max}, transit time T_T, creep time T_C, apparent elastic modulus E, and fluidity β. Correlation analysis is performed on the q-DC data for human breast and pancreatic cancer cell lines.

	D_{cell}	ϵ_{max}	T_T	T_C	E_a	ß
D_{cell}	1.00	0.41	-0.02	0.07	-0.02	-0.14
ϵ_{max}	0.41	1.00	0.06	0.17	-0.15	-0.10
T_T	-0.02	0.06	1.00	0.94	0.69	-0.52
T_C	0.07	0.17	0.94	1.00	0.72	-0.57
E_a	-0.02	-0.15	0.69	0.72	1.00	-0.88
ß	-0.14	-0.10	-0.52	-0.57	-0.88	1.00

REFERENCES

1 Brown M, Wittwer C. Flow cytometry: principles and clinical applications in hematology. *Clin Chem* 2000; **46**: 1221–1229.

2 Elston CW, Ellis IO. Pathological prognostic factors in breast cancer. I. The value of histological grade in breast cancer: experience from a large study with long-term follow-up. *Histopathology* 1991; **19**: 403–410.

3 Webster M, Witkin KL, Cohen-Fix O. Sizing up the nucleus: nuclear shape, size and nuclear-envelope assembly. *J Cell Sci* 2009; **122**: 1477–86.

4 Guilak F, Tedrow JR, Burgkart R. Viscoelastic properties of the cell nucleus. *Biochem Biophys Res Commun* 2000; **269**: 781–786.

5 Guck J, Schinkinger S, Lincoln B, Wottawah F, Ebert S, Romeyke M *et al.* Optical deformability as an inherent cell marker for testing malignant transformation and metastatic competence. *Biophys J* 2005; **88**: 3689–98.

6 Cross SE, Jin Y-S, Rao J, Gimzewski JK. Nanomechanical analysis of cells from cancer patients. *Nat Nanotechnol* 2007; **2**: 780–3.

7 Hur SC, Henderson-MacLennan NK, McCabe ERB, Di Carlo D. Deformability-based cell classification and enrichment using inertial microfluidics. *Lab Chip* 2011; **11**: 912–920.

8 Xu W, Mezencev R, Kim B, Wang L, McDonald J, Sulchek T. Cell stiffness is a biomarker of the metastatic potential of ovarian cancer cells. *PLoS One* 2012; **7**: e46609.

9 Swaminathan V, Mythreye K, O'Brien ET, Berchuck A, Blobe GC, Superfine R. Mechanical stiffness grades metastatic potential in patient tumor cells and in cancer cell lines. *Cancer Res* 2011; **71**: 5075–5080.

10 Hou HW, Li QS, Lee GYH, Kumar a. P, Ong CN, Lim CT. Deformability study of breast

cancer cells using microfluidics. *Biomed Microdevices* 2009; **11**: 557–564.

11 Agus DB, Alexander JF, Arap W, Ashili S, Aslan JE, Austin RH *et al.* A physical sciences network characterization of non-tumorigenic and metastatic cells. *Sci Rep* 2013; **3**: 1449.

12 Nguyen A V, Nyberg KD, Scott MB, Welsh AM, Nguyen AH, Wu N *et al.* Stiffness of pancreatic cancer cells is associated with increased invasive potential. *Integr Biol* 2016. doi:10.1039/c6ib00135a.

13 Kim T-H, Gill NK, Nyberg KD, Nguyen A V, Hohlbauch S V, Geisse NA *et al.* Cancer cells become less deformable and more invasive with activation of beta-adrenergic signaling. *J Cell Sci* 2016; **129**: 4563–4575.

14 Liu C-Y, Lin H-H, Tang M-J, Wang Y-K. Vimentin contributes to epithelial-mesenchymal transition cancer cell mechanics by mediating cytoskeletal organization and focal adhesion maturation. *Oncotarget* 2015; **6**: 15966–15983.

15 Rathje L-SZ, Nordgren N, Pettersson T, Ronnlund D, Widengren J, Aspenstrom P *et al.* Oncogenes induce a vimentin filament collapse mediated by HDAC6 that is linked to cell stiffness. *Proc Natl Acad Sci U S A* 2014; **111**: 1515–1520.

16 Weder G, Hendriks-Balk MC, Smajda R, Rimoldi D, Liley M, Heinzelmann H *et al.* Increased plasticity of the stiffness of melanoma cells correlates with their acquisition of metastatic properties. *Nanomedicine* 2014; **10**: 141–148.

17 Lange JR, Steinwachs J, Kolb T, Lautscham LA, Harder I, Whyte G *et al.* Microconstriction Arrays for High-Throughput Quantitative Measurements of Cell Mechanical Properties. *Biophys J* 2015; **109**: 26–34.

18 Hoelzle DJ, Varghese BA, Chan CK, Rowat AC. A Microfluidic Technique to Probe Cell Deformability. *JoVE* 2014; **91**: e51474–e51474.

19 Byun S, Son S, Amodei D, Cermak N, Shaw J, Kang JH *et al.* Characterizing deformability and surface friction of cancer cells. *Proc Natl Acad Sci* 2013; **110**: 7580–7585.

20 Rosenbluth MJ, Lam WA, Fletcher DA. Analyzing cell mechanics in hematologic diseases with microfluidic biophysical flow cytometry. *Lab Chip* 2008; **8**: 1062–1070.

21 Nyberg KD, Scott MB, Bruce SL, Gopinath AB, Bikos D, Mason TG *et al.* The physical origins of transit time measurements for rapid, single cell mechanotyping. *Lab Chip* 2016; **16**: 3330–3339.

22 Nyberg KD, Hu KH, Kleinman SH, Khismatullin DB, Butte MJ, Rowat AC. Quantitative Deformability Cytometry (q-DC): rapid, calibrated measurements of single cell viscoelastic properties. *Biophys J* 2017; **in press**.

23 Bongiorno T, Chojnowski JL, Lauderdale JD, Sulchek T. Cellular Stiffness as a Novel Stemness Marker in the Corneal Limbus. *Biophys J* 2016; **111**: 1761–1772.

24 Bongiorno T, Kazlow J, Mezencev R, Griffiths S, Olivares-Navarrete R, McDonald JF *et al.* Mechanical stiffness as an improved single-cell indicator of osteoblastic human mesenchymal stem cell differentiation. *J Biomech* 2014; **47**: 2197–2204.

25 Lin J, Kim D, Henry TT, Tseng P, Peng L, Dhar M *et al.* High-throughput physical phenotyping of cell differentiation. *Microsystems Nanoeng* 2017; **3**: 17013.

26 Darling EM, Topel M, Zauscher S, Vail TP, Guilak F. Viscoelastic properties of human mesenchymally-derived stem cells and primary osteoblasts, chondrocytes, and adipocytes. *J Biomech* 2008; **41**: 454–464.

27 Darling EM, Guilak F. A neural network model for cell classification based on single-cell biomechanical properties. *Tissue Eng Part A* 2008; **14**: 1507–1515.

28 Tse HTK, Gossett DR, Moon YS, Masaeli M, Sohsman M, Ying Y *et al.* Quantitative diagnosis of malignant pleural effusions by single-cell mechanophenotyping. *Sci Transl Med* 2013; **5**: 212ra163.

29 Jiang Y, Lei C, Yasumoto A, Kobayashi H, Aisaka Y, Ito T *et al.* Label-free detection of aggregated platelets in blood by machine-learning-aided optofluidic time-stretch microscopy. *Lab Chip* 2017; **17**: 2426–2434.

30 Lee WC, Shi H, Poon Z, Nyan LM, Kaushik T, Shivashankar G V *et al.* Multivariate biophysical markers predictive of mesenchymal stromal cell multipotency. *Proc Natl Acad Sci* 2014; **111**: E4409-18.

31 Pan Y, Robertson G, Pedersen L, Lim E, Hernandez-Herrera A, Rowat AC *et al.* miR-509-3p is clinically significant and strongly attenuates cellular migration and multi-cellular spheroids in ovarian cancer. *Oncotarget* 2016; **7**: 25930–25948.

32 Chan CK, Pan Y, Nyberg K, Marra MA, Lim EL, Jones SJM *et al.* Tumour-suppressor microRNAs regulate ovarian cancer cell physical properties and invasive behaviour. *Open Biol* 2016; **6**. doi:10.1098/rsob.160275.

33 Qi D, Gill NK, Santiskulvong C, Sifuentes J, Dorigo O, Rao J *et al.* Screening cell mechanotype by parallel microfiltration. *Sci Rep* 2015; **5**.

34 Le CP, Nowell CJ, Kim-Fuchs C, Botteri E, Hiller JG, Ismail H *et al.* Chronic stress in mice remodels lymph vasculature to promote tumour cell dissemination. *Nat Commun* 2016; **7**: 10634.

35 Duffy DC, McDonald JC, Schueller OJA, Whitesides GM. Rapid prototyping of microfluidic systems in poly(dimethylsiloxane). *Anal Chem* 1998; **70**: 4974–4984.

36 Rowat AC, Jaalouk DE, Zwerger M, Ung WL, Eydelnant IA, Olins DE *et al.* Nuclear

Envelope Composition Determines the Ability of Neutrophil-type Cells to Passage through Micron-scale Constrictions. *J Biol Chem* 2013; **288**: 8610–8618.

37 Lange JR, Metzner C, Richter S, Schneider W, Spermann M, Kolb T *et al.* Unbiased High-Precision Cell Mechanical Measurements with Microconstrictions. *Biophys J* 2017; **112**: 1472–1480.

38 Ekpenyong AE, Whyte G, Chalut K, Pagliara S, Lautenschläger F, Fiddler C *et al.* Viscoelastic Properties of Differentiating Blood Cells Are Fate- and Function-Dependent. *PLoS One* 2012; **7**. doi:10.1371/journal.pone.0045237.

39 Fabry B, Maksym GN, Butler JP, Glogauer M, Navajas D, Fredberg JJ. Scaling the microrheology of living cells. *Phys Rev Lett* 2001; **87**: 148102.

40 Lautscham LA, Kammerer C, Lange JR, Kolb T, Mark C, Schilling A *et al.* Migration in Confined 3D Environments Is Determined by a Combination of Adhesiveness, Nuclear Volume, Contractility, and Cell Stiffness. *Biophys J* 2015; **109**: 900–913.

41 Adams M, Jones JL, Walker RA, Pringle JH, Bell SC. Changes in tenascin-C isoform expression in invasive and preinvasive breast disease. *Cancer Res* 2002; **62**: 3289–3297.

42 Gordon LA, Mulligan KT, Maxwell-Jones H, Adams M, Walker RA, Jones JL. Breast cell invasive potential relates to the myoepithelial phenotype. *Int J cancer* 2003; **106**: 8–16.

43 Albini A, Iwamoto Y, Kleinman HK, Martin GR, Aaronson SA, Kozlowski JM *et al.* A rapid in vitro assay for quantitating the invasive potential of tumor cells. *Cancer Res* 1987; **47**: 3239–3245.

44 Sheridan C, Kishimoto H, Fuchs RK, Mehrotra S, Bhat-Nakshatri P, Turner CH *et al.* CD44+/CD24- breast cancer cells exhibit enhanced invasive properties: an early step necessary for metastasis. *Breast Cancer Res* 2006; **8**: R59.

45 Chekhun S, Bezdenezhnykh N, Shvets J, Lukianova N. Expression of biomarkers related to cell adhesion, metastasis and invasion of breast cancer cell lines of different molecular subtype. *Exp Oncol* 2013; **35**: 174–179.

46 De Craene B, Gilbert B, Stove C, Bruyneel E, van Roy F, Berx G. The transcription factor snail induces tumor cell invasion through modulation of the epithelial cell differentiation program. *Cancer Res* 2005; **65**: 6237–6244.

47 Behrens J, Mareel MM, Van Roy FM, Birchmeier W. Dissecting tumor cell invasion: epithelial cells acquire invasive properties after the loss of uvomorulin-mediated cell-cell adhesion. *J Cell Biol* 1989; **108**: 2435–2447.

48 Guadamillas MC, Cerezo A, Del Pozo MA. Overcoming anoikis--pathways to anchorage-independent growth in cancer. *J Cell Sci* 2011; **124**: 3189–3197.

49 Creed SJ, Le CP, Hassan M, Pon CK, Albold S, Chan KT *et al.* beta2-adrenoceptor signaling regulates invadopodia formation to enhance tumor cell invasion. *Breast Cancer Res* 2015; **17**: 145.

50 Doerschuk CM, Beyers N, Coxson HO, Wiggs B, Hogg JC. Comparison of neutrophil and capillary diameters and their relation to neutrophil sequestration in the lung. *J Appl Physiol* 1993; **74**: 3040–3045.

51 Bathe M, Shirai A, Doerschuk CM, Kamm RD. Neutrophil transit times through pulmonary capillaries: the effects of capillary geometry and fMLP-stimulation. *Biophys J* 2002; **83**: 1917–33.

52 Wirtz D, Konstantopoulos K, Searson PC. The physics of cancer: the role of physical interactions and mechanical forces in metastasis. *Nat Rev Cancer* 2011; **11**: 512–522.

53 Johnston DG. Cytoplasmic:nuclear ratios in the cytological diagnosis of cancer. *Cancer*

1952; **5**: 945–949.

54 Foraker AG, Reagan JW. Nuclear size and nuclear: cytoplasmic ratio in the delineation of atypical hyperplasia of the uterine cervix. *Cancer* 1956; **9**: 470–479.

55 Pietuch A, Janshoff A. Mechanics of spreading cells probed by atomic force microscopy. *Open Biol* 2013; **3**: 130084.

56 Gardel ML, Nakamura F, Hartwig JH, Crocker JC, Stossel TP, Weitz DA. Prestressed F-actin networks cross-linked by hinged filamins replicate mechanical properties of cells. *Proc Natl Acad Sci* 2006; **103**: 1762–1767.

57 Park CY, Tambe D, Alencar AM, Trepat X, Zhou EH, Millet E *et al.* Mapping the cytoskeletal prestress. *Am J Physiol Cell Physiol* 2010; **298**: C1245-52.

58 Jalilian I, Heu C, Cheng H, Freittag H, Desouza M, Stehn JR *et al.* Cell elasticity is regulated by the tropomyosin isoform composition of the actin cytoskeleton. *PLoS One* 2015; **10**: e0126214.

59 Martens JC, Radmacher M. Softening of the actin cytoskeleton by inhibition of myosin II. *Pflugers Arch Eur J Physiol* 2008; **456**: 95–100.

60 Murrell M, Oakes PW, Lenz M, Gardel ML. Forcing cells into shape: the mechanics of actomyosin contractility. *Nat Rev Mol Cell Biol* 2015; **16**: 486–498.

61 Wang N, Naruse K, Stamenovic D, Fredberg JJ, Mijailovich SM, Tolic-Norrelykke IM *et al.* Mechanical behavior in living cells consistent with the tensegrity model. *Proc Natl Acad Sci U S A* 2001; **98**: 7765–7770.

62 Wang N, Tolic-Norrelykke IM, Chen J, Mijailovich SM, Butler JP, Fredberg JJ *et al.* Cell prestress. I. Stiffness and prestress are closely associated in adherent contractile cells. *Am J Physiol Cell Physiol* 2002; **282**: C606-16.

63 Kraning-Rush CM, Califano JP, Reinhart-King CA. Cellular traction stresses increase with increasing metastatic potential. *PLoS One* 2012; **7**: e32572.

64 Chambers AF, Groom AC, MacDonald IC. Dissemination and growth of cancer cells in metastatic sites. *Nat Rev Cancer* 2002; **2**: 563–572.

65 Denais CM, Gilbert RM, Isermann P, McGregor AL, te Lindert M, Weigelin B *et al.* Nuclear envelope rupture and repair during cancer cell migration. *Science* 2016; **352**: 353–358.

66 Olson MF, Sahai E. The actin cytoskeleton in cancer cell motility. *Clin Exp Metastasis* 2009; **26**: 273–287.

67 Ma C, Wu B, Huang X, Yuan Z, Nong K, Dong B *et al.* SUMO-specific protease 1 regulates pancreatic cancer cell proliferation and invasion by targeting MMP-9. *Tumour Biol* 2014; **35**: 12729–12735.

68 Zhao X, Gao S, Ren H, Sun W, Zhang H, Sun J *et al.* Hypoxia-inducible factor-1 promotes pancreatic ductal adenocarcinoma invasion and metastasis by activating transcription of the actin-bundling protein fascin. *Cancer Res* 2014; **74**: 2455–2464.

69 Nabeshima K, Inoue T, Shimao Y, Sameshima T. Matrix metalloproteinases in tumor invasion: role for cell migration. *Pathol Int* 2002; **52**: 255–264.

70 Poincloux R, Collin O, Lizarraga F, Romao M, Debray M, Piel M *et al.* Contractility of the cell rear drives invasion of breast tumor cells in 3D Matrigel. *Proc Natl Acad Sci U S A* 2011; **108**: 1943–1948.

71 Petrie RJ, Koo H, Yamada KM. Generation of compartmentalized pressure by a nuclear piston governs cell motility in a 3D matrix. *Science* 2014; **345**: 1062–1065.

Chapter V: Conclusions and Future Directions

Conclusions

Advances in our knowledge of PDAC have resulted in the development of a number of new therapies (1,2) yet the average 5-year survival rate of pancreatic cancer patients is still under 10% (3). Therefore, it is imperative to explore additional characteristics of PDAC that may increase our understanding of why current therapies are ineffective and enable the discovery of new druggable therapeutic targets. Here I establish physical phenotypes of PDAC cells, including cell size and deformability, and determine how these are associate with cell invasion. I also measure the ability of PDAC cells to actively generate forces, and establish how actomyosin contractility and protrusive forces contribute to both cell stiffness and invasion.

In chapter I, I find that three PDAC cell lines – Hs766T, MIA PaCa-2, and PANC-1 – are more deformable than the nontransformed pancreatic ductal epithelial cell line – HPDE – but that more invasive PDAC cells are stiffer than their less invasive counterparts. The finding that stiffer cells are more invasive was surprising as a large number of studies on the cell deformability of breast, ovarian, and prostate cancer show that more deformable cells are more invasive. My results, along with studies in lung cancer and breast cancer cells treated with a beta-adrenergic agonist, highlight that cancer cell stiffness is cell-type dependent.

In chapter II, I determine that active force generation, namely the myosin II-dependent production of contractile forces and actin polymerization driven by Arp2/3 and formins, are determinants of both PDAC cell stiffness and invasion potential; these data support why stiffer cells are more invasive, as described in chapter I.

In chapter III, I describe a label-free physical phenotype model that can predict invasion using single-cell physical phenotypes. These physical parameters are all obtained by microfluidic quantitative deformability cytometry, a novel method developed by Kendra Nyberg and Dr. Amy Rowat.

Overall, my studies establish the physical properties of PDAC cells, and the relationship between these physical phenotypes and invasion. Since the proteins and processes that regulate cell deformability and active force generation are required for invasion and mechanotransduction, these biophysical studies should deepen our knowledge of cancer cell behaviors, such as motility, growth, and resistance to chemotherapy.

Future Directions

My work sets the foundation for future studies that integrate our knowledge of the physical properties PDAC cells with our understanding of the mechanical properties of the PDAC microenvironment. Alterations in the physical microenvironment of pancreatic cancer are strongly implicated in disease progression. A number of studies have established that the extensive stromal deposition in and around PDAC tumors accelerates disease progression (4,5). For example, the increased density of extracellular matrix (ECM) in the PDAC microenvironment activates a positive feedback loop that increases the deposition of collagen and other ECM proteins, and further increases disease progression (5). Additional studies establish that cells sense their physical surroundings through a process called mechanosensing, which is the ability of a cell to sense and transmit mechanical stimuli from the microenvironment into the cell. Mechanotransduction is imperative to cancer processes, including proliferation, invasion, and metastasis (6). I hypothesize that the sensing of mechanical stimuli may be influenced by the stiffness of a cell since the ability of a cell to sense and respond to external physical cues occurs through integrins and focal adhesions, which are physically connected to the cell cytoskeleton, a major determinant in cell stiffness (7). In addition, cells also generate mechanical forces. For example, contractile and protrusive forces, which I have implicated in PDAC cell stiffness and invasion, are transmitted to the surrounding environment via adhesion proteins to trigger forward cell locomotion (8,9). Thus, it is essential to study the physical properties of PDAC cells and their microenvironment as two entities that influence each other, and not as independent characteristics that influence cancer cell behaviors.

Specifically, future studies can explore the how cancer processes are altered when PDAC cells of different stiffnesses are introduced to a stiff matrix, which is representative of the fibrotic cancer microenvironment, or a more deformable matrix, which is representative of a non-disease state. What molecular changes occur when stiffer or more deformable PDAC cells sense a stiffer surrounding? Does mechanosensing differ in stiff or deformable cells, and do these differences contribute to an increased invasive potential or other hallmark cancer behaviors?

A deeper understanding of the relationship between the physical properties of PDAC cells and the surrounding microenvironment could lead to knowledge that could enhance the development of therapeutics. In 2009, Olive *et al*. presented data suggesting that the inhibition of Sonic hedgehog (Shh) disrupted and lessened the desmoplasia present in the PDAC microenvironment. Using a pancreatic cancer mouse model, they showed that Shh inhibition and the resultant decrease in stromal tissue increased mouse survival compared to controls (10). They hypothesized that the stroma conferred chemoresistance by decreasing drug penetrance to the tumor cells. These exciting results formed the basis for clinical trials that used IPI-926, a drug that inhibits the Shh pathway and decreases desmoplasia around tumors, in combination with gemcitabine, a common chemotherapeutic for pancreatic cancer. Unfortunately, the trials were stopped due to poor clinical results. From this example, it is clear that the physical properties of

PDAC, either cell or microenvironment, should not be individually targeted for treatment without knowledge of how one affects the other, as they are each part of a complex system. It is possible that the stiffness and density of the PDAC extracellular matrix is not only upregulating pathways that promote cancer progression (5), but also may be confining tumor cells in a small space to prevent rapid dissemination (11). Thus, it is imperative to understand the relationship between the physical properties of cells and their environment as we develop new therapies to treat, and hopefully cure, pancreatic cancer.

References

1. Di marco M, Grassi E, Durante S, et al. State of the art biological therapies in pancreatic cancer. World J Gastrointest Oncol. 2016;8(1):55-66.
2. Kleger A, Perkhofer L, Seufferlein T. Smarter drugs emerging in pancreatic cancer therapy. Ann Oncol. 2014;25(7):1260-70.
3. Surveillance, Epidemiology, and End Results (SEER) 18 registries, National Cancer Institute, 2016.
4. Hezel AF, Kimmelman AC, Stanger BZ, Bardeesy N, Depinho RA. Genetics and biology of pancreatic ductal adenocarcinoma. Genes Dev. 2006;20(10):1218-49.
5. Laklai, H. et al. Genotype tunes pancreatic ductal adenocarcinoma tissue tension to induce matricellular fibrosis and tumor progression. Nat. Med. 22, 497–505 (2016).
6. Wirtz D, Konstantopoulos K, Searson PC. The physics of cancer: the role of physical interactions and mechanical forces in metastasis. Nat Rev Cancer. 2011;11(7):512-22.
7. Jaalouk DE, Lammerding J. Mechanotransduction gone awry. Nat Rev Mol Cell Biol. 2009;10(1):63-73.
8. Danuser, G., Allard, J. & Mogilner, A. Mathematical modeling of eukaryotic cell migration: insights beyond experiments. Annu. Rev. Cell Dev. Biol. 29, 501–528 (2013).
9. Bangasser, B. L., Rosenfeld, S. S. & Odde, D. J. Determinants of maximal force transmission in a motor-clutch model of cell traction in a compliant microenvironment. Biophys. J. 105, 581–592 (2013).
10. Olive KP, Jacobetz MA, Davidson CJ, Gopinathan A, McIntyre D, Honess D, Madhu B, Goldgraben MA, Caldwell ME, Allard D, et al. Inhibition of Hedgehog signaling enhances

delivery of chemotherapy in a mouse model of pancreatic cancer. Science. 2009;324:1457–1461.

11. Rhim AD, Oberstein PE, Thomas DH, et al. Stromal elements act to restrain, rather than support, pancreatic ductal adenocarcinoma. Cancer Cell. 2014;25(6):735-47.
12. Yamaguchi H, Condeelis J. Regulation of the actin cytoskeleton in cancer cell migration and invasion. Biochim Biophys Acta. 2007;1773(5):642-52.